U.PORTO
FACULDADE DE CIÊNCIAS
UNIVERSIDADE DO PORTO

INSTITUTO DE CIÊNCIAS BIOMÉDICAS ABEL SALAZAR
UNIVERSIDADE DO PORTO

· U C ·

FCTUC FACULDADE DE CIÊNCIAS
E TECNOLOGIA
UNIVERSIDADE DE COIMBRA

A biophysical approach to mitochondrial gene therapy: gemini surfactant-based colloidal vectors

Ricardo de Sá Bessa
Mestrado em Bioquimica
Departamento de Química e Bioquímica
2016

Orientador
Prof. Doutor Eduardo Jorge Figueira Marques, DQB, FCUP

Coorientadora
Profª. Doutora Maria Amália da Silva Jurado, Dep. Ciências da Vida, FCTUC e CNC- Centro de Neurociências e Biologia Celular, Universidade de Coimbra

U.PORTO

FACULDADE DE CIÊNCIAS
UNIVERSIDADE DO PORTO

Todas as correções determinadas pelo júri, e só essas, foram efetuadas.
O Presidente do Júri,

Porto, _____/_____/_____

Para a minha mãe

ACKNOWLEDGEMENTS

To my supervisor, Prof. Eduardo Marques for the opportunity to participate in the research group for this project, all the support given throughout the entire project and especially for the help in professional development.

To my co-supervisor, Prof. Amália Jurado, for the patience, knowledge and help on the biological part of the project.

To Prof. Luisa do Vale for the use of the synthesis laboratory and all the support and teachings.

To Dr. Ana Cardoso for always being there, and the help and teachings in laboratory work.

To all the physical chemistry research group for the friendship and companionship, through the year.

To Bárbara Claro for all the moral support and incentive.

To Isabel Oliveira and Bárbara Abreu for all their help and suggestions.

To my mother, for all the support, food and taxi services.

To my family, which accompanied me through this journey.

To José Ferreira, my co-conspirator in writing.

To all my friends, despite their constant nagging.

Abstract

Efficient mitochondrial gene delivery is a technique with great biomedical potential, due to the possibility of using it for the treatment of many pathologies, currently without cure. Among many other types of vectors, surfactant and lipid-based systems stand out as an efficient, safe and biocompatible strategy to integrate new DNA in the existing mitochondrial genome.

The aim of this work was to determine the physicochemical properties, transfection efficiency and cytotoxicity of novel serine-based gemini surfactants. Gemini are a class of surfactants containing two polar head groups and two hydrocarbon chains (*n*) linked by a spacer (*s*) at the headgroup level.

In this work, a series of four different serine-based gemini surfactants, all with a 12 carbon long alkyl spacer (*n*-12-*n*), and hydrocarbon chains containing *n* = 12, 14, 16 and 18 carbons, were successfully synthesized. The critical micelle concentration and other interfacial parameters of these compounds were determined by tensiometry, and several unusual and interesting trends were obtained.

These novel gemini surfactants were further used to prepare binary gemini/DNA and ternary gemini/DNA/helper lipid complexes with mtDNA, with several formulations, differing on the gemini:DNA (+/-) charge ratio. The transfection efficiency and cytotoxicity of the formulations were tested *in vitro*, in HeLa cell cultures. Both types of complexes were further characterized in terms of morphology, size and zeta potential. The various formulations of complexes containing gemni surfactants were shown to have distinctive transfection efficiencies and cytotoxicity, varying significantly with the presence of helper lipids.

This work is a contribution to the more global study of the relationships between the lengths of both spacer and hydrocarbon chain of gemini surfactants, on one side, and their effects on physicochemical properties and biological activity, on the other side, providing another piece of the puzzle in the rational design of novel gene delivery systems.

Keywords: surfactant, gemini, serine, mitochondria, DNA, transfection, cytotoxicity, helper lipids, alkyl spacer, *cmc*

Resumo

A terapia génica mitocondrial eficiente é uma técnica de elevado potencial biomédico, devido à possibilidade da sua utilização no tratamento de inúmeras patologias atualmente sem cura. Entre muitos outros tipos de vetores, os nanosistemas auto-agregados baseados em surfactantes e lípidos destacam-se como uma estratégia eficaz, segura e biocompatível para integrar novo DNA no genoma mitocondrial já existente.

O objetivo deste trabalho consistiu na determinação de propriedades físico-químicas, citotoxicidade e eficiência de transfecção de novos surfatantes gemini derivados de serina. Os surfactantes gemini são uma classe de agentes tensioativos que contêm dois grupos polares ligados entre si por um espaçador covalente (*s*), e duas cadeias hidrocarbonadas principais (*n*).

Neste trabalho, efetuou-se com sucesso a síntese de uma série de quatro surfactantes gemini diferentes, derivados de serina, todos com um espaçador de 12 carbonos (*n*-12-*n*) e cadeias hidrocarbonadas diferentes, com *n* = 12, 14, 16 e 18 carbonos. A concentração micelar crítica dos compostos e outros parâmetros interfaciais correlacionados foram determinados por tensiometria através do método da placa de Wilhelmy. Estes compostos demonstraram apresentar tendências pouco comuns e interessantes nas suas propriedades físico-químicas, em particular na dependência da *cmc* com o comprimento das cadeias hidrocarbonadas.

Os novos surfactantes gemini foram posteriomente usados para preparar complexos binários gemini/DNA e ternários gemini/DNA/lípido auxiliare com mtDNA, de acordo com várias formulações, diferindo entre si na razão de carga (+/-) gemini:DNA. A citotoxicidade e eficiência de transfecção destas formulações foram testadas *in vitro*, usando culturas de células HeLa. Ambos os tipos de complexos foram ainda estruturalmente caracterizados pelo seu tamanho, morfologia e potencial zeta. As diferentes formulações de complexos demonstraram possuir eficiências de citotoxicidade e transfecção distintas, variando de forma significativa na presença de lípidos auxiliares.

Este trabalho constitui um contributo para o estudo das relações entre o comprimento da cadeia hidrocarbonada e espaçador dos surfactantes gemini derivados de serina e os seus efeitos sobre as propriedade físico-químicas e atividade biológica, configurando-se assim como uma nova peça de puzzle no desenvolvimento racional de novos sistemas de terapia génica.

Palavras-chave: surfatante, gemini, serina, mitocôndria, DNA, transfecção, citotoxicidade, lípidos auxiliares, espaçador, cmc

TABLE OF CONTENTS

Figure Index

Table Index

Supplementary information index

Acronyms and Symbols

cac – Critical aggregation concentration

Chol - Cholesterol

cmc - Critical micelle concentration

COSY – 2D NMR homonuclear correlation spectroscopy

CPEO - Chronic progressive external ophthalmopelia

DCE – Dichloroethane

DIC – Differential interference contrast

DLS – Dynamic Light Scattering

DSC – Differential Scanning Calorimetry

DMEM - Dulbecco's Modified Eagle's Medium

FBS – Fetal bovine serum

FRET – Fluorescence Resonance Energy Transfer

GFP – Green Fluorescent Protein

HBS – HEPES Buffered Saline

HeLa – Human epithelial carcinoma cell

HSQC – NMR Heteronuclear single-quantum correlation spectroscopy

KSS - Kearns-Sayre Syndrome

LHON - Leber's hereditary optic neuropathy

MERRF - Myoclonic epilepsy with ragged-red fibers

MGT – Mitochondrial Gene Therapy

mtDNA – Mitochondrial DNA

NMR – Nuclear Magnetic Resonance

ROS – Reactive oxygen species

TFA – Trifluoroacetic acid

TPAP - Tetrapropylammonium perruthenate

Chapter 1: Introduction

1.1 Mitochondrial gene therapy

The mitochondrion is the cell organelle that produces most of the required energy under normal conditions. Therefore, its health is of paramount importance for the cell metabolism and the overall health and functional capacity of the organism.

The mitochondrion is also unique as the sole organelle in human cells that contains its own DNA, separated from the nucleus, and as such possesses its own unique problems and pathologies.

1.1.1 Mitochondrial diseases

Even though mitochondria have lost, in the process of evolution, most of their genes (coding proteins that mediate their function) to the cell's nucleus, they still maintain a separate, albeit small, genome[3], as seen in Figure 1.

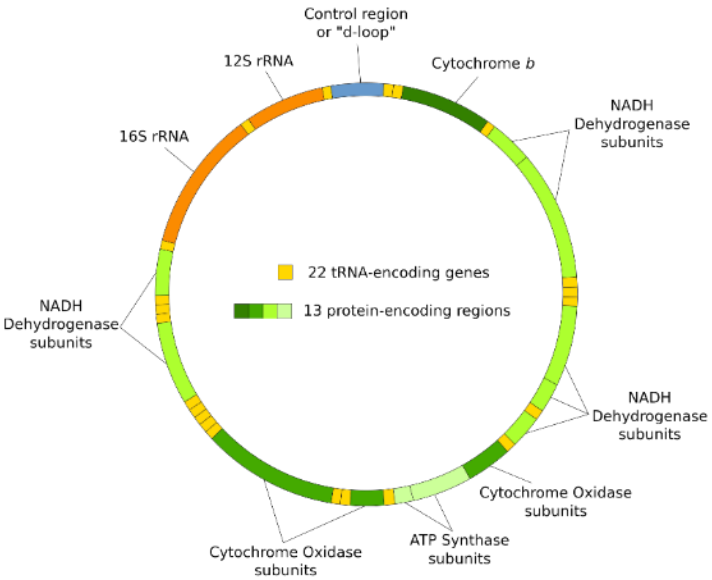

Figure 1 - Representation of the mitochondrial genome and the zones corresponding to certain proteins. The orange zones correspond to the part of the mtDNA that encodes for the mitochondria specific ribosome subunits From ref[4].

Mitochondrial diseases are caused by dysfunctions in the mitochondria's normal metabolic processes, generating a measurable effect on the organism as a whole. These dysfunctions have varying degrees of severity and can lead to a vast array of pathologies, since mitochondria are important for many critical vital processes, such as

energy generation, apoptosis mediation, generation of signalling molecules, to cite a few.[5-6]

Depending on the metabolic pathway affected these pathologies can range from immediately lethal to lifelong debilitating symptoms and reduced lifespan.[7-8]

One of the first mitochondrial pathologies to be discovered is Leber's hereditary optic neuropathy (LHON), a blindness with a sudden onset caused by a mtDNA missense mutation[9]. Other examples of classic mitochondrion based diseases are chronic progressive external ophthalmopelia (CPEO)[9], Kearns-Sayre Syndrome (KSS)[10-11] and myoclonic epilepsy with ragged-red fibers (MERRF)[12]. In Figure 2, one can see the location of some of the cited mutations in the mitochondrial genome.

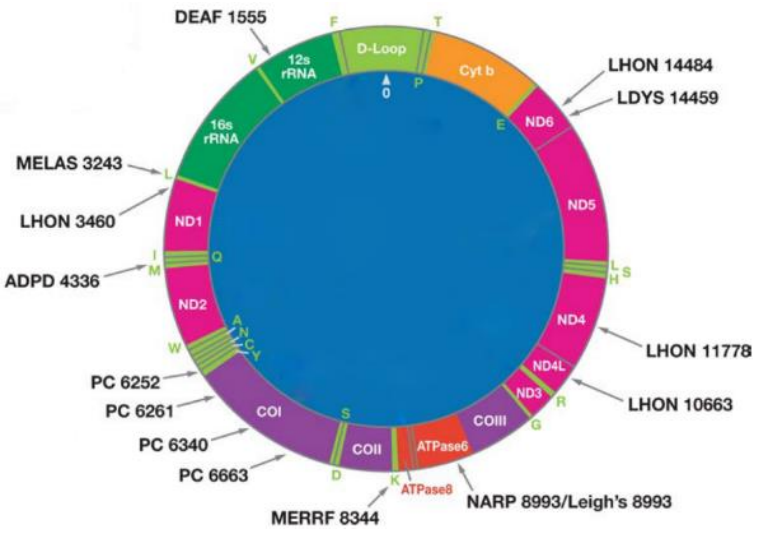

Figure 2 - Position in the mitochondrial genome of some well-known mutations. Adapted from ref[3].

Recently, mitochondria have been linked to other diseases that until now were thought to unrelated to this organelle, such as Parkinson's disease[13-14], diabetes melitus[15] and Alzheimer's disease[16-17].

Mitochondria are a center of high energy production; however, they use a process that generates copious amounts of reactive oxygen species (ROS), which are highly damaging to organic tissue and molecules, including DNA. These ROS are generated in very close proximity to the mitochondrial genetic material, which can induce mutations over time if the processes for ROS removal are not efficient.[8, 18]

1.1.2 Treating mitochondrial dysfunction

Treating a mitochondrial dysfunction is not an easy task and over the years several strategies have been developed to prevent or treat the diseases caused. Three distinct methodologies arise, described as follows.

Starting on the prevention front, there is a very recent technique that allows for a mother with a known mitochondrial dysfunction to have healthy children, free of the mother's dysfunction or propensity to it. This technique consists of the donation of an oocyte with healthy mitochondria by another woman, which is then enucleated. The nucleus from the mother's fertilized zygote is then transferred to the empty oocyte that in turn, is also potentially capable of forming a fully functioning embryo[19]. A representation of this process can be seen on Figure 3.

The ethical problems related to this process are, however, still subject to intense discussion.[20]

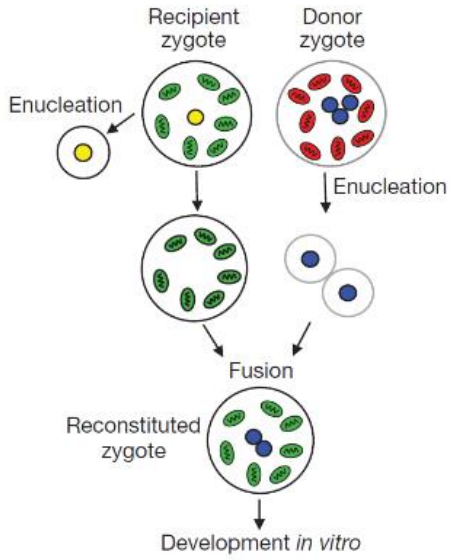

Figure 3 - Representation of the mitochondrial donation process. In red are the mutated undesired mitochondria, and the healthy in green. The blue circles represent the mother's genetic material. From ref[19].

Another pathway to treat these dysfunctions is the pharmacological path, which can be used to rectify the signalling from the mitochondrial pathways, either by blocking or activating proteins, in order to eliminate, modulate or reduce the symptoms caused by the dysfunctions.[21]

The pharmacological path can be applied with more ease than any other, for well documented dysfunctions, but can also cause many undesired side effects. With recent developments, it is possible to reduce the intensity and incidence of the side effects with

drug delivery systems, by making the drug available only to the specific place of treatment.[22]

Lastly, it is possible to treat mitochondrial dysfunctions by acting at the root of the problem: the mitochondrial DNA. While possible, it is no easy task to change the already existing DNA of a living multicellular being. On this respect, mtDNA is different from the regular cell's DNA and this fact entails both advantages and disadvantages.

The mitochondrial DNA exists inside the mitochondria itself in circular forms (like bacterial plasmids) and multiple copies exist at the same time in each mitochondrion[5]. It is not condensed around histones like the nucleus' DNA, making it more prone to changes. Its location inside the mitochondrion is both an advantage, since it makes it easier to have selectivity and no interference with regular DNA, and a disadvantage, as the mitochondrion membranes are more difficult to overcome than the nucleus' porous membrane. The modification of the mitochondria mtDNA can be achieved through mitochondrial gene therapy, which will be discussed below.

1.1.3 Workings of Mitochondrial Gene Therapy (MGT)

Adhya et al define mitochondrial gene therapy as "a protocol for the treatment of mitochondrial dysfunctions using genetic material as the therapeutic agent, delivered to the appropriate sub-compartment of the mitochondria, improving its function and having a measurable clinical effect"[5]. The genetic material used can be of various natures: DNA, RNA and their derivatives.

Inside each mitochondrion there are between 1000 and 5000 copies of circular mtDNA that mutate independently. A certain threshold of mutated copies must be reached for a dysfunction to manifest itself[23]. This is called heteroplasmy and varies with the individual in terms of number of mutated copies required[24]. This threshold can be overcome in two distinct manners in a single organism over its lifetime, through the vegetative and relaxed replication of mtDNA[25]. Vegetative replication occurring during mitosis and subsequent division of mitochondria, has the potential to both eliminate the mutation over time or increase the number of mutated plasmids. At all points of the cell's cycle, mtDNA is constantly turned over, with random plasmids being replicated – relaxed replication – which can lead over time to the propagation of mutated plasmids and onset of mitochondrial disease. Both vegetative and relaxed replication occur at the same time[25].

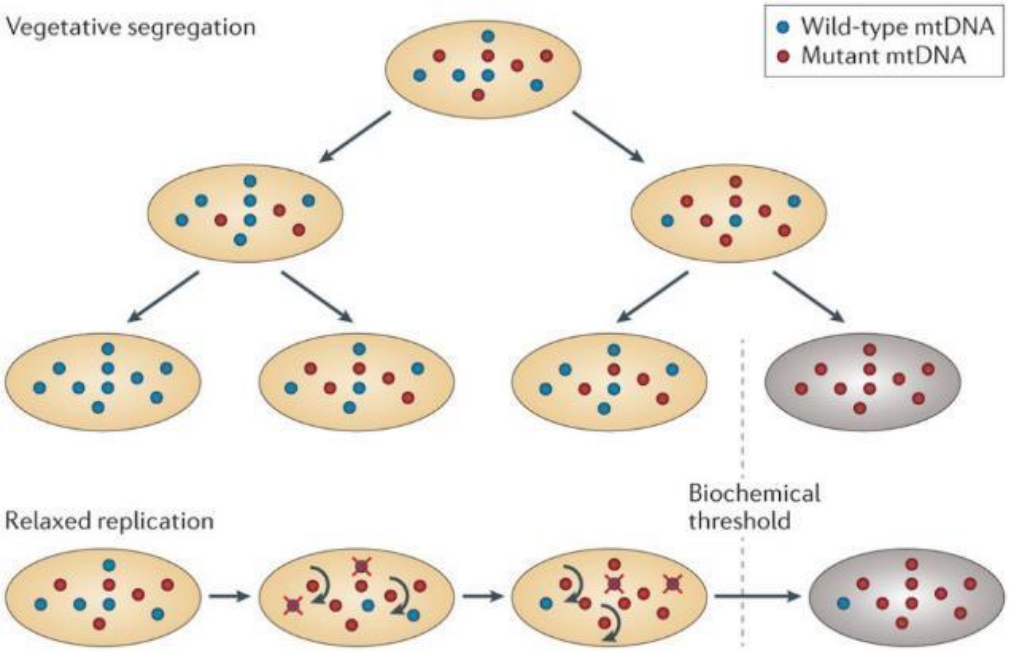

Figure 4 - Schematics for both vegetative and relaxed replications of mtDNA. From ref[25].

Therefore, MGT must be able to deliver enough synthetic plasmid DNA to offset the number of mutated copies, in order to revert the dysfunction. Once enough copies have been delivered to offset the ratio of mutated mtDNA, the mitochondria may clonally expand the new plasmid, causing new mitochondria replicated during mitosis to lack enough copies of the mutated mtDNA for the dysfunction to remain.[26]

For transfection to occur, several conditions must be met: the DNA delivery system must pass undetected through the immune system (*in vivo*); it must reach the targeted cells; it must be able to interact with the cell's membrane, in order to be internalized, either by endocytosis or through direct translocation; once the system is able to get inside the cell it should have the ability to avoid lysosomal degradation, by performing an endosomal escape; lastly the delivery system should release the encapsulated DNA near the target organelle (Figure 5)[27].

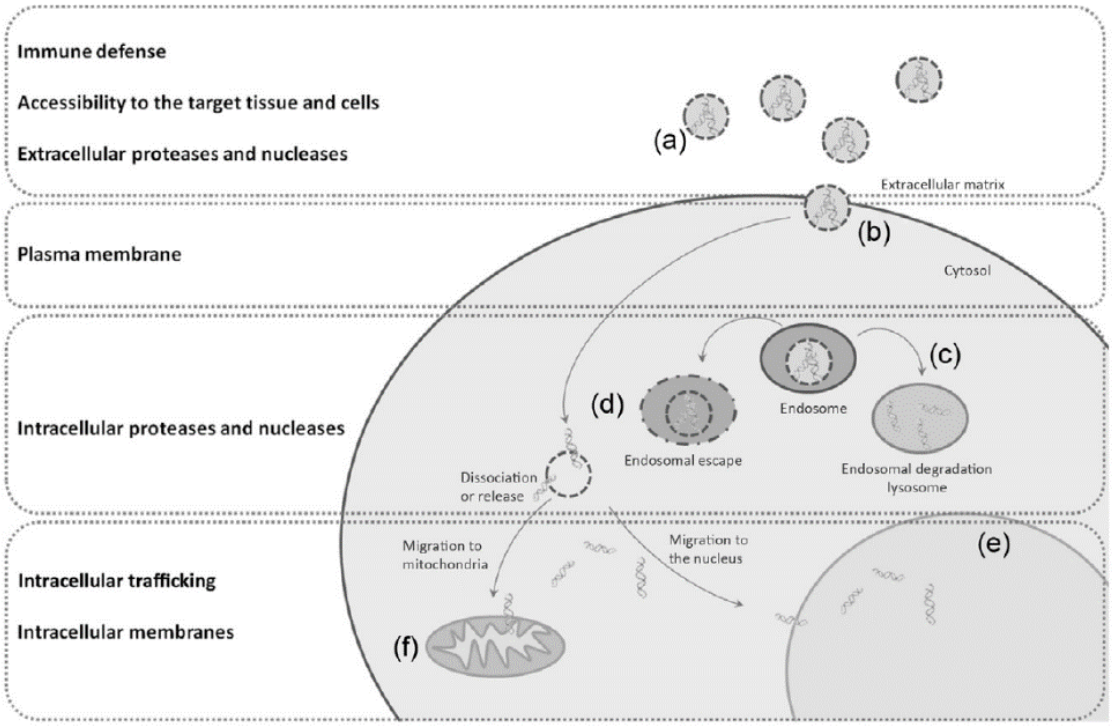

Figure 5 - Schematic of the path a gene delivery system must go through for transfection to successfully occur. From ref[27].

Direct translocation is an internalization process independent of both energy and proteins present in the cellular membrane, being mediated by the ability of the surfactant or surfactant/lipid mixture to interact and destabilize membranes with specific lipid composition[28]. Endocytic pathways, however, are highly dependent on the proteins present on the membrane, relying somewhat less on the chemical compatibility of the transfection system's chemical nature with biological membranes. The downside is that the system must be able to escape the endosome in order to free the DNA. Such is the case in clathrin and caveolae-mediated endocytosis[27].

In the endocytic pathways it should be noted that the size of the transfection system is an important factor to consider, since the ideal size for internalization varies with the pathway (macropinocytosis being the pathway able to accommodate larger structures). If the complexes are too small, they might not be able to interact with enough membrane proteins to start the process; if too large, it might be impossible for the cell to proceed on their uptake.

1.1.4 Conventional vectors for transfection

The simplest approach to gene delivery is direct DNA injection, but this method has the drawback of being to process only one cell at a time, making it unusable for most medical applications[29]. Many other strategies for gene delivery have been created in the last years, from folded DNA boxes[30] to metallic nanoparticles[31], each with their own advantages and disadvantages.

Figure 6 - Representation of DNA chains adsorbed to a nanoparticle's surface.

A common strategy when using nanoparticles is to adsorb the DNA at the particle's surface[32] (Figure 6), thus allowing them to be more easily internalized by the cell[33].

The vector that immediately stands out as an efficient way to transfect DNA into cells is the virus, since introducing genetic material into cells is the natural way for a virus to replicate – this causes naturally a high transfection efficiency. However, custom viruses have a high cost of production and require better safety standards due to their natural high mutability[34-35].

On the other hand, lipid-based transfection systems have great potential for DNA transfection due to their versatility.[29] There is a myriad of different lipids, surfactants and combined lipid/surfactant system that can be used, allowing for greater refinement of transfection, depending on the types of cells and targets. Some lipids commonly used for transfection, due to their high efficiency and low cytotoxicity, are lipofectamine©[36], monolein[37] and DOPE[38].

Lipid-based transfection systems work by encapsulating, adsorbing or otherwise securing DNA in self-assembled structures. These self-assemblies mimic the cell's own

chemical and physical structure, allowing them to be internalized along with DNA. However, lipids suitable for this application are expensive, so their synthetic alternatives, the surfactants, are a desired field of study. Like lipids, surfactants also have both and hydrophilic and hydrophobic region, but their chemical nature is very distinct, usually having smaller size and molar mass. The downside of surfactants is their typically low biocompatibility, increasing their cytotoxicity. To get the “best of both worlds”, surfactant-based transfection systems usually have included in their composition some lipids to counter this effect, called the helper lipids[39]. These mixed systems are usually referred to as lipoplexes.

Helper lipids not only increase the biocompatibility of a surfactant-based system, but also can give those systems extra or augmented properties. An example of this is DOPE, which can be used to increase the efficiency of endosomal escape in transfection systems that use this route[28].

1.2 Lipids and Surfactants

Surfactants are a class of molecules with a unique chemical structure, that confers them unusual properties. These molecules have a hydrophobic part (apolar; usually a long hydrocarbon chain) and a hydrophilic (polar) part, both important in defining the physicochemical behaviour of the whole molecule. Surfactants can be classified by several properties, usually:

- By the polar head group charge, as anionic, cationic, zwitterionic and non-ionic;
- By the polar head group chemical nature, as amines, carboxylates, amino acid derived, etc;
- By the number of both apolar chains (single-chained, double-chained, etc.) and polar head groups (monomeric, dimeric, etc.);

The combination of different polar head groups and hydrophobic chains in different levels of complexity allows an enormous variety of surfactants. [40-41]

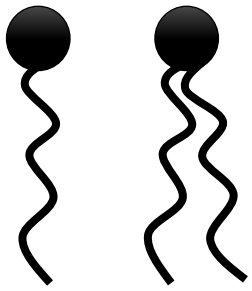

Figure 7 - Representation of a simple, one hydrophilic headgroup/one hydrophobic tail (left) and a more complex, one hydrophicilic headgroup/two hydrophobic tails (right) surfactants.

One may think that these molecules may be somewhat rare to find outside an applied chemical environment, but that is far from the truth. In reality surfactants are present not only in research and industrial processes, but in living systems aswell. Lipids are the building blocks of all cell membranes and play other different roles in nearly all of the organisms, from intracellular signalling[42] to preventing lungs from collapsing on themselves[43-44].

1.2.1 Surfactant properties

Since surfactants have a dual nature in terms of polarity (they are both hydrophilic and hydrophobic) in separate zones of the molecule, some peculiar properties appear.

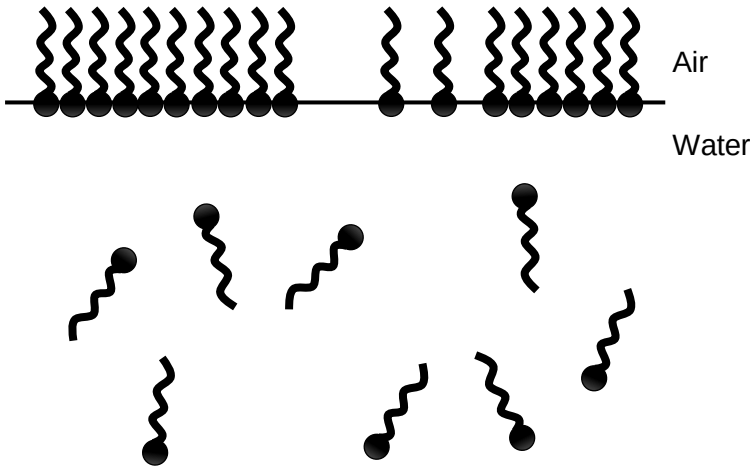

Figure 8 - Visual representation of the air/water interface and surfactant adsorption on it.

While in solution, surfactants tend to concentrate more at the surface or interfaces of the solution than in the bulk due to the presence of the hydrophobic tail, as its contact with water molecules is not as favourable as the contact with air. Furthermore, the creation of an interface between two media of different polarities, such as water/air is also unfavourable, giving rise to an interfacial tension (i.e. excess Gibbs energy per unit area of surface) and an increase of the overall Gibbs energy of the system[27]. This makes it thermodynamically favourable for the surfactant molecules to move to the interface in order to make the contact between the two more favourable and reducing the Gibbs energy.

In the case of a water/air interface, the surfactant molecules gather on the surface and reduce the Gibbs free energy of the area of contact between the two media (Figure 8). This reduces the energy per area unit that is necessary to keep the two phases separate, as the surfactant acts a stable link between them. Furthermore, the surfactant molecules intercalate with the water molecules at the surface (which are more structurally organized than in the bulk), making them lose cohesiveness among them[45], thus lowering the surface tension.

1.2.1.1 Surface tension

Surface tension manifests itself as the differences between the Gibbs energies of molecules located at the surface and the bulk of a liquid. Due to this difference, the surface of the liquid has a tendency to reduce its area of contact with air.

In the case of a liquid-air interface (a surface), different forces act on the surface's molecules and bulk molecules (Figure 9). In the bulk, solvent molecules are completely surrounded by equal molecules and have forces pulling them in all directions simultaneously, with a resulting null net force. At the surface, however, molecules are not surrounded by the same number of molecules and the resulting net force pulls them inward into the solution (Figure 9). Additionally, the surface acquires an elastic-like behaviour due to this aspect.

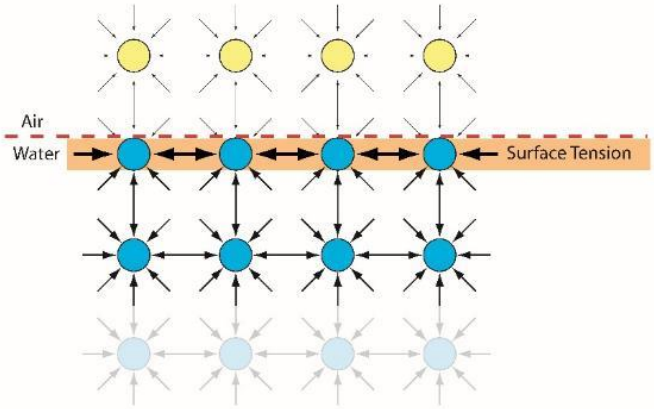

Figure 9 - Representation of forces acting on water molecules at the surface and in the bulk. From ref[46].

This greater cohesiveness, between liquid-liquid molecules than liquid-air molecules, makes creation additional surface area energetically unfavourable. Due to these molecular aspects, the surface tends to reduce its area in order to reduce the unfavourable interactions.

Surface tension can then be thermodynamically defined by the reversible work need to expand this surface area, as demonstrated in eq. [1], where γ is the surface tension, w the reversible work and ΔA the increase in total surface area.

$$w = \gamma \Delta A \qquad [\ 1\ ]$$

For a planar surface and constant pressure and temperature, surface tension can be defined in terms of Gibbs energy (eq. [2]).

$$\gamma = \left(\frac{\delta G}{\delta A} \right)_{p,T} \qquad [\ 2\ ]$$

1.2.2. Self-Assembly

As more and more surfactant is added into a solution, the surfactant adsorption at the surface starts to become thermodynamically unfavourable (this means the surface tension can't be infinitely lowered). Since surfactant molecules cannot adsorb to the interface anymore the surfactant molecules start organizing themselves, in a process called self-assembly, in organized structures (Figure 10), in order to minimize the contact between the tails and the solvent, thus minimizing the hydrophobic effect.

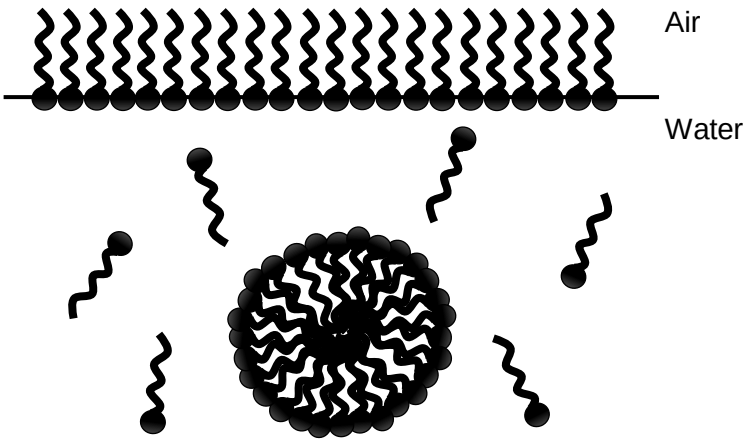

Figure 10 - Representation of a surfactant solution at the *cmc* and formation of micelles.

The concentration at which the surfactant molecules start self-assembling is called the critical aggregation concentration (*cac*). Once the critical micelle or aggregation concentration has been achieved in a solution, it will not change with the addition of more surfactant molecules. The extra molecules will form self-assembled structures, maintaining the solution's unimer concentration constant.

However, surfactants do not all organize in the same manner, with different molecules assembling in different types of structures, such as micelles and vesicles, among others. It should be noted that in many cases it is not only the nature of the molecule that defines the structure but also the concentration of said molecules.

The type of structure a surfactant self-assembles into can be predicted to some extent by two distinct models, discussed below.

1.2.2.1 Surfactant packing parameter

The surfactant packing parameter associates the volumetric geometry of a molecule to the structures it is likely to self-assemble into, in a solution. This parameter is defined by the ratio between the actual volume occupied by the molecule, defined by the volume of the hydrocarbon chain (V_{hc}; Figure 11), and the theoretical volume it would occupy considering a cylindrical shape with the optimal area (a_{hg}) of the polar headgroup and the length of the hydrocarbon chain (l_{hc}), as seen in eq.[3].

$$P_S = \frac{V_{hc}}{a_{hg} l_{hc}} \qquad [\,3\,]$$

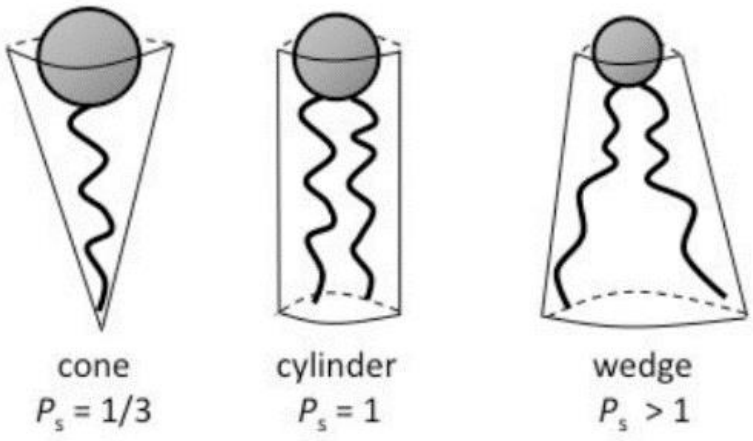

Figure 11 - Visual representation of the volumes used for the calculation of the packing parameter P_s. From ref[47].

It is considered that when P_S<1/3 (cone shaped molecule), surfactants will preferably assemble into spherical micelles, with cylindrical micelles arising at 1/3<P_S<1/2 (truncated cone shape). At 1/2<P_S<1 the preferred structures are vesicles and flexible bilayers (as P_S approaches 1), with planar extended bilayers at P_S=1. Above P_S=1 surfactants will tend to form reverse spherical or reverse cylindrical micelles (Figure 12).

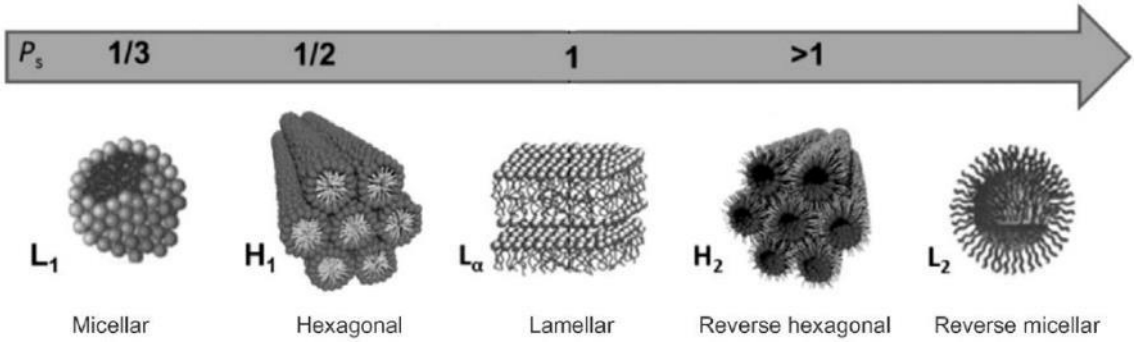

Figure 12 - Visual representation of the relation between the surfactant packing parameter and the structure formed. Adapted from ref[27].

It is difficult to calculate the value of a_{hg} due to many variables that interfere with it (such as the presence of salts in the solution), but the values of V_{hc} and l_{hc} can be estimated for simple surfactants by the formulae (eq. 2 and eq. 3) below, where n_c is the number of carbons in the hydrocarbon chain:

$$V_{hc} / nm^3 = 0.0274 + 0.0269 n_c \qquad [4]$$

$$l_{hc} / nm = 0.154 + 0.127\, n_c \qquad [5]$$

1.2.2.2 Spontaneous curvature

As an alternative to the surfactant packing parameter model, the spontaneous curvature model is especially useful for the description of different kinds of bilayer based structures, such as vesicles and planar bilayers.

In this model, all structures are considered to be formed by surfactant films, with the structure formed defined by the curvature of the film. This can be described by the following equation (eq. 4), in which H_0 is the spontaneous curvature, and R_1 and R_2 are the radii of curvature in perpendicular directions.

$$H_0 = \frac{1}{2}\left(\frac{1}{R_1} + \frac{1}{R_2}\right) \qquad [6]$$

Each radius, R, has an associated signal (positive or negative) related to the direction of a vector that defines it on the self-assembled structure. By convention the polar region is always taken as positive (Figure 13).

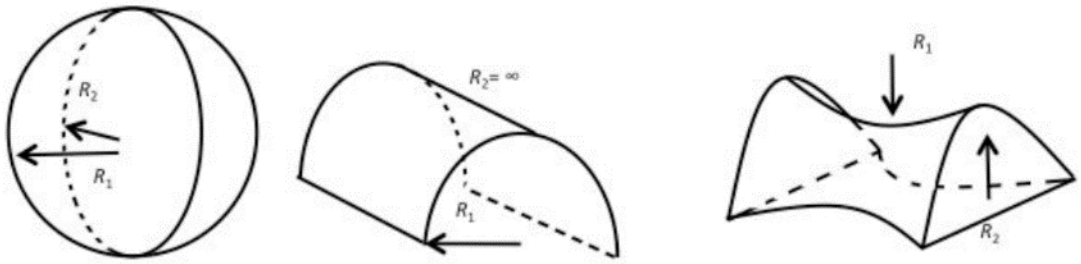

Figure 13 - Visual representation of the curvature in self-assembled structures and respective radii. From ref[47].

A regular spherical micelle has two defined radii with a positive signal, giving it a spontaneous curvature of 1/R, while a planar bilayer film has a H_0 of ≈ 0 (zero curvature) since both its radii are immeasurable (considered infinite). A reverse spherical micelle has H_0 = -1/R, since its polar region is in the innermost part of the sphere.

The spontaneous curvature adopted by a surfactant film is always the one that minimizes the Gibbs energy of the system. Unlike the packing parameter, which relates the shape of the final aggregate to the nature of the individual molecule, the spontaneous curvature refers more to the physical properties of the film as a whole.

1.2.3 Structures

While alone in a solution, each individual surfactant molecule is called an unimer, the basic unit of any self-assemblage. By order of complexity, the first and simplest self-assembled structure that can be formed is the micelle. Micelles can have several shapes, depending on the surfactant concentration and packing parameter, among them spherical, elongated, cylindrical and worm-like shapes. In all these structures, the hydrocarbon chains are directed to the centre, reducing their contact with the aqueous media.

In certain conditions, such as packing parameter > 1 or the presence of a high amount of a hydrophobic substance (such as an oil), reverse micelles can be formed, which have their hydrophobic tail turned outward.

Next on the order of complexity are the vesicles (Figure 14). These usually spherical structures are formed by a curved bilayer of the surfactant, having an aqueous pool. This structure is much larger than regular micelles and have typically slower dynamics, but unimers in it still exchange with those in solution over time in dynamic equilibrium. The large aqueous pool is a particularity of this structure that makes it

especially useful for drug delivery, since it can contain and protect water-soluble molecules.

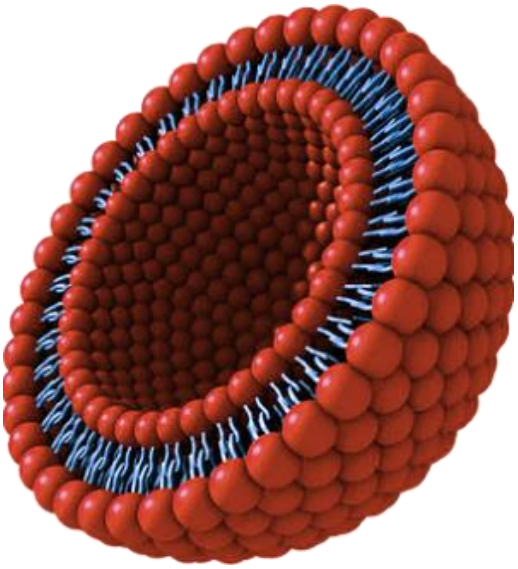

Figure 14 - Cross-section representation of a liposome. From ref[48].

Bilayers are composed of opposing layers of surfactants, with either the hydrocarbon tails or the headgroups in contact, depending on the polarity of the solvent. They can be categorized in 3 distinct morphologies, closed (vesicles), planar and bicontinuous.[49]

1.2.4 Gemini surfactants – Structure and properties

Gemini surfactants are composed of two hydrophilic and two hydrophobic moieties, covalently linked to each other usually at the headgroup level via a unit that is called the spacer[2].

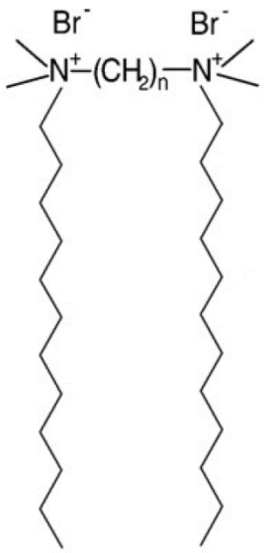

Figure 15 - Bis-quat gemini surfactant alkanediyl-α,ω-bis(dodecydimethylammonium bromide). Spacer with variable length. Adapted from ref[2].

Like conventional surfactants, gemini can have innumerable structural variations. They can be classified mainly by symmetry (symmetric if both monomers have identical headgroup and hydrocarbon tail, asymmetric if they do not), charge of the headgroups (neutral, cationic, anionic or catanionic), chemical nature of both the headgroups and spacer[50-51], length of the hydrocarbon chains, origin of the headgroups (amino-acid derived, sugar derived[52], among others).

Gemini surfactants, despite their high synthesis costs, have several advantageous properties over conventional single-chained surfactants, such as a lower *cmc*, higher surface activity and higher structural versatility[27, 53].

The higher surface activity and low *cmc* are especially sought after in several areas, industry among them, since it lowers the amount of compound needed in comparison to a conventional surfactant to achieve the same effect. This helps turn industrial processes more efficient[54] and less prone to contaminations, helping to prevent toxicity in medical and cosmetic applications[55]. Some gemini are even reported to have an antimicrobial effect[54, 56-58].

In recent years gemini of various chemical nature and structural configurations have been studied for their applications in gene and drug delivery due to their efficiency and low cytotoxicity[54, 59-60], especially those derived from amino-acids[23, 59]. In this work we approach serine-derived gemini surfactants.

1.2.4.1 Serine-based gemini surfactants

In recent studies, gemini derived from several amino acids have shown to be even better than conventional surfactants, for medical applications due to their even lower cytotoxicity[61-63].

These amino acid derivatives show higher biocompatibility, due their structural likeness to biological molecules. This allows them to readily interact with biological membranes, facilitating the delivery of drugs/DNA into the cell, either by fusion with the membranes or by a facilitated internalization.[60]

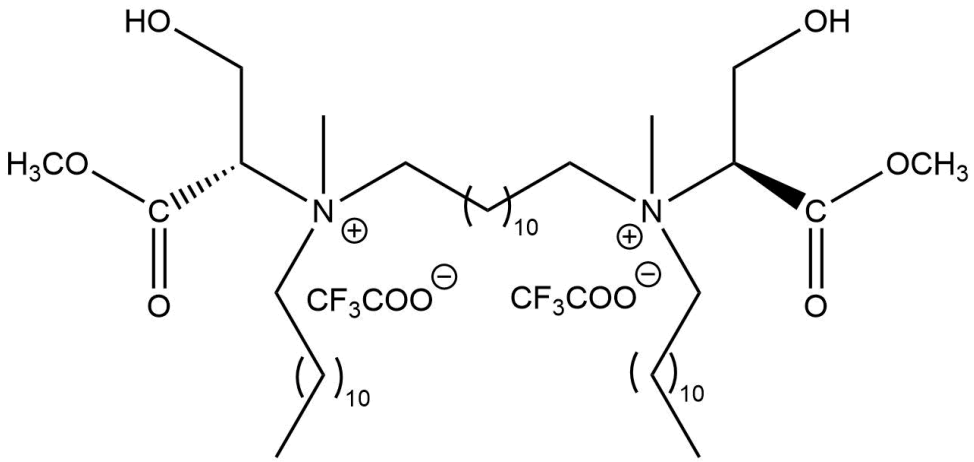

Figure 16 - Example of a gemini surfactant molecule. Serine derived gemini with a spacer of twelve carbons and both hydrocarbon chains with twelve carbons.

Serine-based gemini were synthesized for the first time in 2012[61], comprising of two N-alkylated serine residues linked by a simple hydrocarbon chain spacer.

1.2.5 Compaction and transfection of DNA by surfactants

The interaction of DNA with the surfactant of a gene delivery system is of paramount importance to determine its ability to form stable and usable forms of aggregates for use in transfection.

The DNA molecule possesses multiple negative charges along its double helix due to the phosphate groups present in its structure. These negative charges allow cationic surfactants, and their self-assembled structures to interact with the DNA chain. Most surfactants used for this purpose are cationic, given that the opposite charge grants a much stronger electrostatic interaction. However, uncharged surfactants can also be employed, although the nature of interaction is different, since they interact by van der Waals and hydrophobic forces alone, which are generally weaker[64-65].

The type of self-assembled structure present in solution before DNA complexation will greatly change the final conformation of supramolecular surfactant:DNA aggregates[66]. For example, it was reported[67] that when DNA is added to existing micellar systems it tends to form compacted globular complexes, with chains of DNA connecting several of these globules (Figure 17). Furthermore, with vesicle-forming gemini surfactants, it was seen that the addition of DNA caused a rearrangement of the system, forming inverted hexagonal structure, containing DNA[27, 67]. This aggregation of DNA with self-assembled structures is often called *DNA packing.* For cationic surfactants, the structures of the surfactant:DNA complexes depends greatly on the charge ratio between the two, leading to different levels of packing.

Mixtures of cationic and neutral surfactants are often used to balance the magnitude of the interaction with DNA, preventing either excessive DNA packing (which would difficult its later release inside the cell) or too loose or non-existent packing.

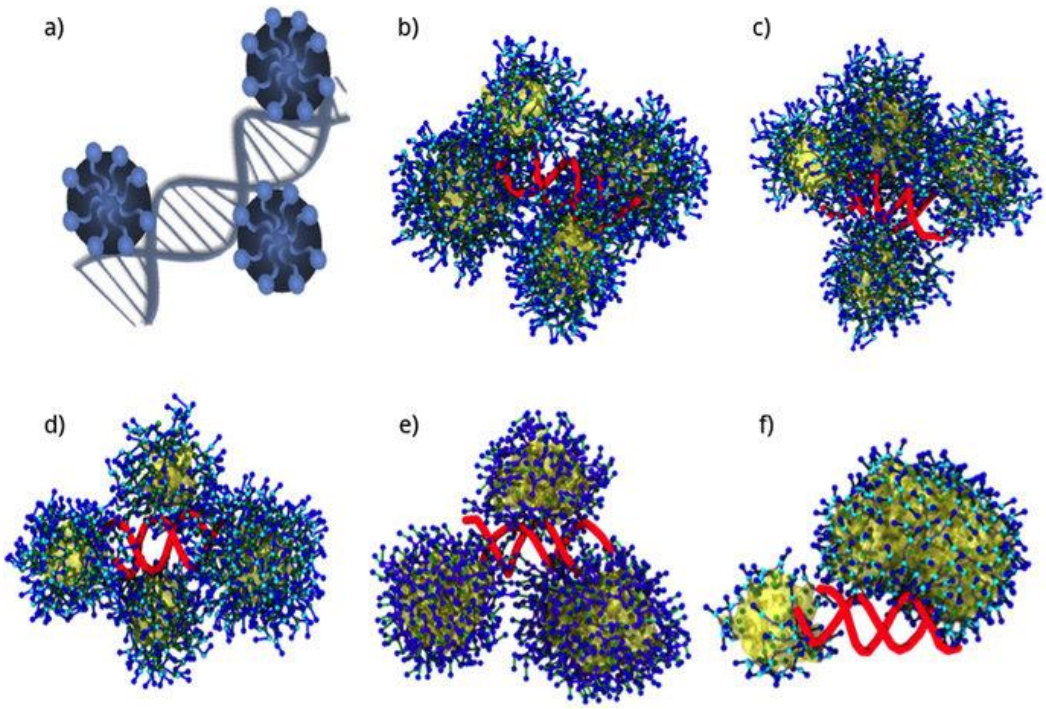

Figure 17 - Example of DNA packing in an environment with cationic spherical micelles, as reported using electron microscopy. From ref[68].

Concerning gemini surfactants, the compaction of DNA might involve a chain effect, derived from the combined effect of hydrophobic and electrostatic interactions, promoting the interaction of additional surfactant molecules over time, as more molecules are present, starting from a small cluster[27]. This process has an enthalpy gain, thus, being favoured by a low *cmc*[27, 69].

It was found that the most efficient compaction was mediated by those with short spacers (n=2, n=3)[27, 70], which form disperse micelle-like aggregates of the two components.

For transfection purposes it was found that generally, the transfection ability is higher, for lower spacer lengths, correlating to the area occupied by the surfactant head-group[27]. This might be explained by the fact that short spacer maintain the positive charge of the cationic head-groups, in a distance more favourable for interaction with the 4.9Å spaced, negatively charged phosphate groups in DNA[27]. Additionally, it is not possible to generalize further the influences of the chemical nature of the bond between headgroup and spacer[27].

1.3 Aim of this project

Mitochondrial gene therapy techniques and protocols are becoming ever more popular due to their potential ability to treat otherwise incurable diseases and syndromes, such as the ones referred in chapter 1.1.1. Like all gene therapies, the treatment efficiency depends on the delivery system chosen. This system must able to both survive the biological environment (degradation, inactivation, etc.) and be able to safely deliver the genetic cargo to the inside of cells. Many strategies and types of delivery systems can be adopted for this purpose. In this project, the strategy followed is the use of surfactant and lipid-based colloidal DNA carriers, with the specific objective of targeting the mitochondria, inside cells.

This project is part of a more global study of gemini surfactants, both conventional and amino-acid derived, and their transfection abilities, developed in the research groups of University of Porto and University of Coimbra[23, 59-61, 71-75]. The studies that have already been published, present not only the advantages of gemini surfactants to their monomeric counterparts in terms of DNA compaction, transfection efficiency and cytotoxicity, but also the advantages of amino-acid derived regular and gemini surfactants in terms of biocompatibility. In this project, we assess the influence of varying length of the hydrocarbon chains (from twelve to eighteen carbons long) in serine derived cationic gemini surfactants, all with the same hydrocarbon spacer (twelve carbons long).

The development of this project can be divided in three major parts: (1) organic synthesis of the serine-derived gemini surfactants; (2) Physicochemical, interfacial and morphological characterization of the neat surfactants and their complexes with DNA and helper lipids; (3) biological studies of the transfection efficiency and cytotoxicity of the complexes, *in vitro*; (4) comparisons with previous studies.

Chapter 2: Materials and methods

2.1 Serine based gemini surfactants organic synthesis

2.1.1 Reagents and preparative reactions

With the synthetic pathway used, both the spacer and side chain carbons must be added to the serine derivative in their aldehyde and dialdehyde (for the spacer) forms. Due to the overall instability of these long chain aldehydes, they must be synthesized right before their use in the main synthesis.

All the aldehydes variants were synthesized using the same reaction, the tetrapropylammonium perruthenate (TPAP) catalysed oxidation of their respective alcohol forms[76], which are available commercially. TPAP was used in a molar quantity equal to 5% of the reagent.

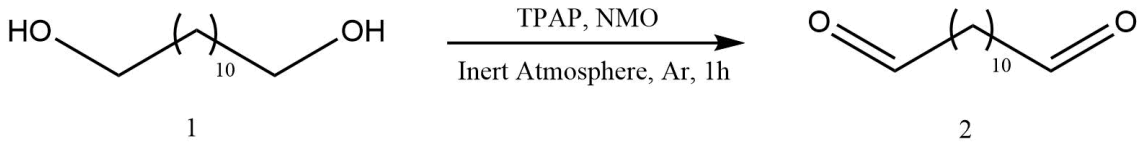

Figure 18 - Representation of the reaction of oxidation of 1,12-dodecanediol to 1,12-dodecanedial.

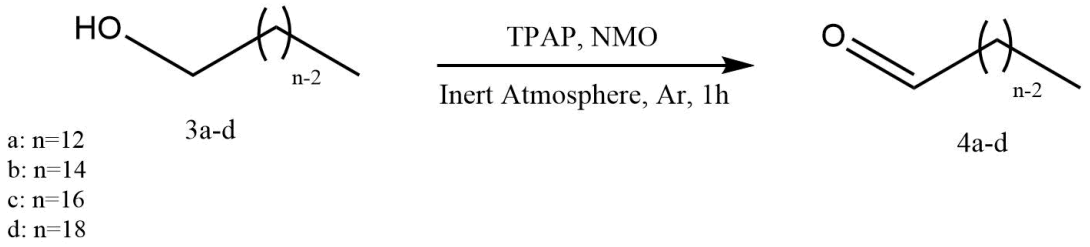

Figure 19 - Representation of the reactions of oxidation to aldehydes of the several long chained alcohols used.

2.1.2 Synthetic pathway

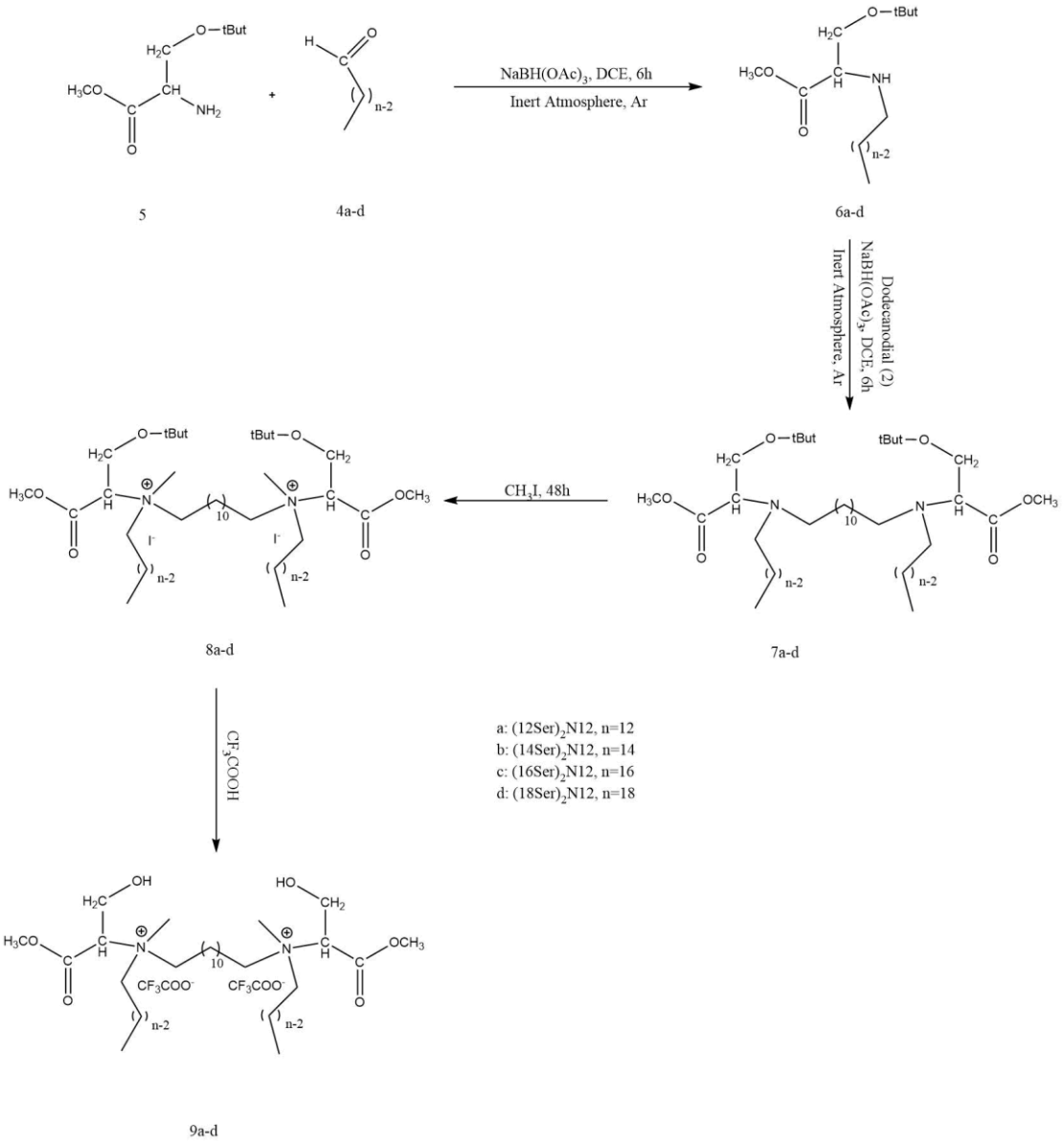

Figure 20 - General synthesis pathway for the several gemini surfactants produced.

The synthesis pathway for the $(nSer)_2N12$ gemini surfactants used in this work has two initial reductive amination reactions. Both aminations were processed under Argon inert atmosphere with sodium triacetoxyborohydride ($NaBH(OAc)_3$) as the reducing agent.

The first reaction is used to attach the variable length hydrocarbon chain onto a *o*-methylated (in the carboxyl group), *o-terc*-butyl protected (in the alcohol group) serine, creating (nSer) monomers. In the second reductive amination the monomers are chained together to each other and the twelve carbon long spacer, by carefully maintaining reaction stoichiometry to avoid excess formation of unwanted species. The resulting

product was then doubly methylated with methyl iodide (CH_3I) on both ternary amine groups, turning them into quaternary ammonium groups, with iodide counter ions. Lastly, the *terc*-butyl group was removed with trifluoroacetic acid (TFA), exchanging the iodide counter ions for trifluoroacetate counter ions in the process.

2.1.3 Purifications

2.1.3.1 Column chromatography

To ensure that a minimum of side products are present at the end of each reaction step, column chromatography was employed to purify the resultant mixture of each step and isolate the desired product.

These purification steps in the middle of the synthesis chain prevent the formation of compounds that could be inextricable from the desired product at the final step, when the final product is fully formed.

The columns used have an embedded ceramic filter at the bottom and were packed with a thin layer of sodium sulphate (Sigma Aldrich) followed by fine silica, the stationary phase in the system. The mobile phase, or eluent mixture, depends on the reaction step that was purified, due to the different polarity needs of each intermediate product.

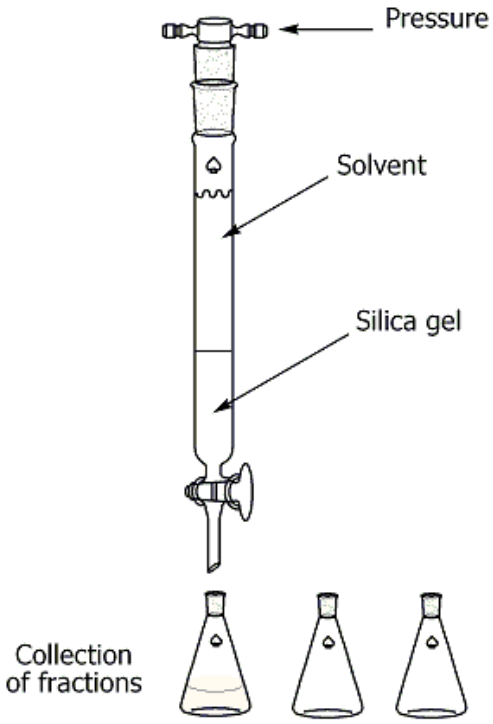

Figure 21 - Flash column chromatography schematic. From ref[1].

The method employed differs slightly from the regularly used process since it was done under artificial air pressure, with a small air pump at the top of the column, a flash column chromatography (Figure 21).

After the column separation, the relevant fractions (assayed by Thin Layer Chromatography (TLC)) were combined and the solvent was removed using a rotary evaporator, readying the product for the following step.

2.1.3.2 Nuclear magnetic resonance (NMR)

Nuclear magnetic resonance is a technique that employs the ability of atomic nuclei to absorb and re-emit electromagnetic radiation when a magnetic field is present.

Some atomic nuclei, such as ^{1}H, ^{13}C, ^{14}N, ^{15}N, ^{19}F, among others, are magnetic because of their charge and because they behave as if spinning. This magnetic property allows them to interact with magnetic fields, in a manner similar to bar magnets. However, unlike bar magnets, the atomic nuclei do not always align themselves to the magnetic field, due to quantum restrictions; they can also oppose it. These two configurations of the atomic nuclei are of different energy, lower energy being the aligned configuration while the opposed configuration has a higher energy level (Figure 22).

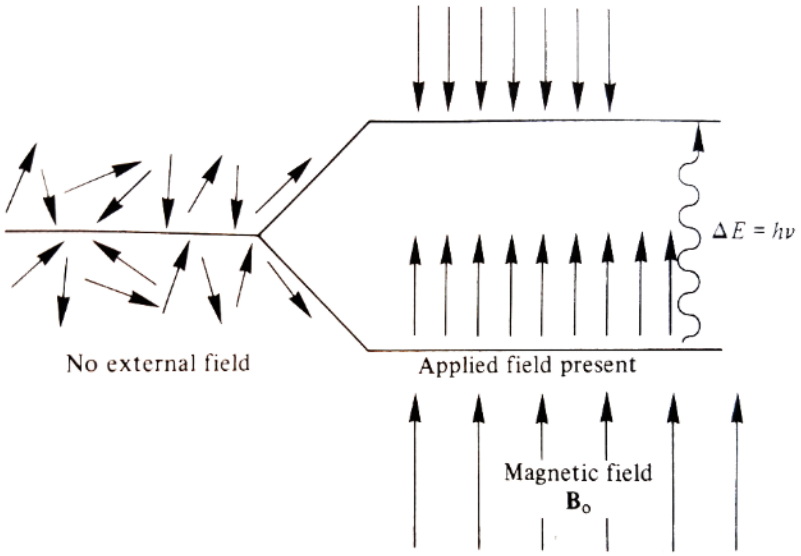

Figure 22 - Representation of the different configuration of atomic nuclei without and with the presence of a magnetic field Bo and the energy gap between the aligned and opposed configurations. Adapted from ref[77].

The energy difference between the two configurations is unique to the type of nucleus in a given magnetic field and can be translated to an electromagnetic frequency by the Bohr relationship (eq. [7])

$$\Delta E = h\nu \qquad [\ 7\ ]$$

As an example, the ^{1}H nucleus has an energy difference (ΔE) of approximately 6.6 x 10^{-26} J in a magnetic field of intensity 2.35 tesla (T); thus, the correspondent frequency is 100 MHz, on the radiofrequency band of the electromagnetic spectrum. If the field intensity changes, so does the energy difference, increasing proportionally to the magnetic field intensity – with a field strength of 7.0 T for example, the frequency of the energy difference would be 300 MHz (Figure 23).

While in the magnetic field, if the nuclei are irradiated with the radiofrequency that matches the frequency of the energy difference they will undergo transitions from the aligned state to opposed and vice-versa, absorbing part of the radiofrequency transmission energy. This process is called resonance.

The resonating frequency of these nuclei vary not only with the strength of the applied magnetic field (Figure 23), but also with the chemical environment they are in, such as the neighbouring nuclei in a molecule with different electron densities, which change their magnetic susceptibilities. The change in resonating frequency by the chemical environment is called a *chemical shift* and is usually expressed in ppm (parts per million), and represented by the greek letter δ.

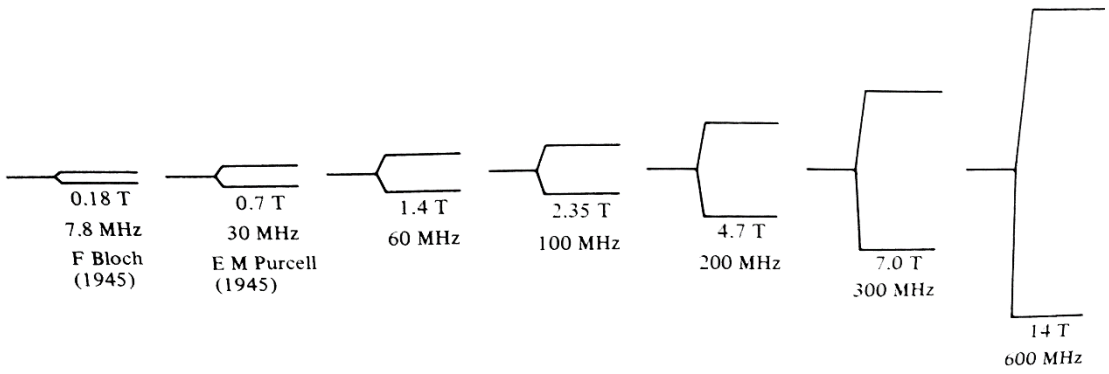

Figure 23 - Changes in the resonant frequency of ^{1}H nuclei with the change of the magnetic field's strength. Adapted from ref[77].

By measuring both the frequency at which the nucleus absorbs the radiofrequency signal and how much it absorbs, it is possible to build a spectrum that can be read to identify the nature of the nuclei (and their chemical neighbourhood via the

chemical shift) and the number of these nuclei in the molecule. It is possible then to reconstruct the structure of the entire molecules by these data alone. However, it may require more than one NMR analysis to do so in more complex molecules.(77)

NMR spectra peaks can also be split in several components due to spin-spin coupling, which arises from the nuclei interference with each other because of their innate small magnetic field.

In this work, ^{1}H NMR was used to determine the structure and purity of the products in the intermediate steps of the synthesis, while the final product of each synthesis was analysed by four distinct techniques: ^{1}H, ^{13}C, COSY and HSQC, to ensure that the products are in good purity for the rest of the work. With the exception of the final NMR spectra, for which the product was dissolved in deuterated acetone or dimethyl sulfoxide, for the intermediary NMR spectra, the products were dissolved in deuterated methanol.

2.1.3.1 NMR peak attributions

The synthesis of the various gemini surfactants were carried out by the procedure previously described.

The characterization of the intermediate and final products of the synthesis was carried out by ^{1}H and ^{13}C (final products only) NMR, presented in the supplementary information section.

The NMR data for $(12Ser)_2N12$ is not shown, since it coincides with data already reported in literature(71).

2.2 Surfactant characterization

2.2.1 Tensiometry - Wilhelmy Plate Method

There are several methods that can be employed to determine the surface tension of a liquid, using different physical properties and characteristics. These methods can be divided in three distinct categories:

- Based on force: such as Wilhelmy Plate method, Du Noüy Ring method and capillary elevation method;
- Based on pressure: such as maximum drop pressure method;
- Based on shape: such as sessile drop method and pendant drop method.

Figure 24 – DCAT11 tensiometer used for the surface tension measurements.

The shape-based methods need low amounts of liquid to determine the surface tension and are able to achieve good precision, but are technically difficult to execute. They may require some correction of the experimental values obtained (the sessile drop method requires chromatic aberration corrections when a camera is used to determine the contact angle).

Force-based methods are also in general very precise, but much simpler to execute, the downside being that they require expensive equipment (with the exception

of the capillary elevation method). The Wilhelmy Plate method was used for all surface tension measurements in this work.

In this method, the Wilhelmy plate is attached to a balance, and a vessel with the liquid to be measured is placed under it. The balance is zeroed and the vessel with the liquid is then elevated until the plate breaks the liquid's surface. At this point, a meniscus forms around the length of the plate due to the surface tension, which exerts a downward force, pulling the plate (Figure 25). This force is measured by the balance and is used to calculate the surface tension by the following formula (eq. [8]).

$$\gamma = \frac{m_{measured} \times G}{L_{plate} \times \cos\theta} \qquad [\,8\,]$$

Here, γ is the surface tension, $m_{measured}$ is the value measured by the balance, G is gravitational constant, L_{plate} is the plate's perimeter and θ is the contact angle of the liquid with the plate. Since the plate is made of a rough platinum or platinum-iridium alloy, the contact angle θ=0°, thus being completely wetted by the liquid. The equation can then be simplified (eq. [9]).

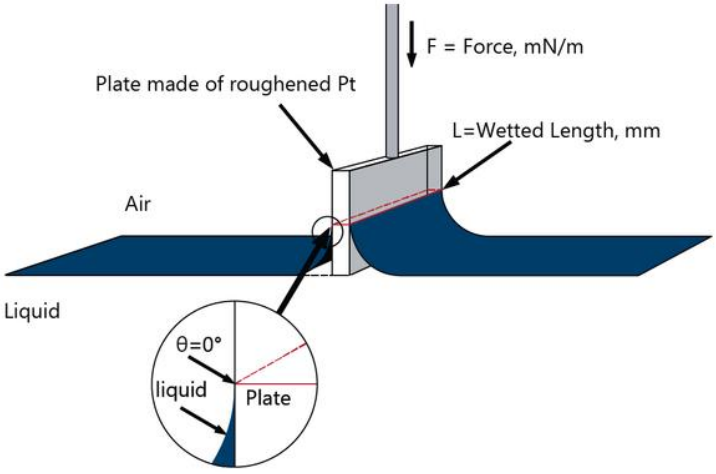

Figure 25 - Wilhelmy Plate method theoretical schematic.

$$\gamma = \frac{F}{L} \qquad [\,9\,]$$

Experimental procedure

For this work, a DCAT11 tensiometer from Dataphysics was used. This apparatus consists of a sealed chamber (to stop air drafts from affecting the measurement) with a motorized elevation platform of high precision (with an error of ±0.0001 mm) with a thermostatization module (fed from an external source, a thermostated bath from Julabo), and a high precision balance (±0.00001 g) on the top.

A glass vessel was used for the solution, previously washed with deionized water and ethanol, and dried in an oven at 100°C. The Wilhelmy plate was also washed with deionized water and ethanol, but dried in a butane flame.

For all experiments the vessel was loaded with 25.0g of ultra-pure water (Millipore™) and the surface tension measured, to further assess the purity of the water. Surfactant solutions were prepared within 24 hours of the measurement with ultra-pure water and maintained overnight in an oven at 25°C.

Aliquots of the surfactant solution under study were transferred to the vessel, using micropipettes (Gilson™). For each aliquot added the solution was magnetically agitated for 3 minutes, followed by 1 minute of rest. The plate was then immersed in the solution and left to stabilize for at least 5 minutes.

Each curve obtained by this method contains 20 to 29 surface tension data points, each for an added aliquot.

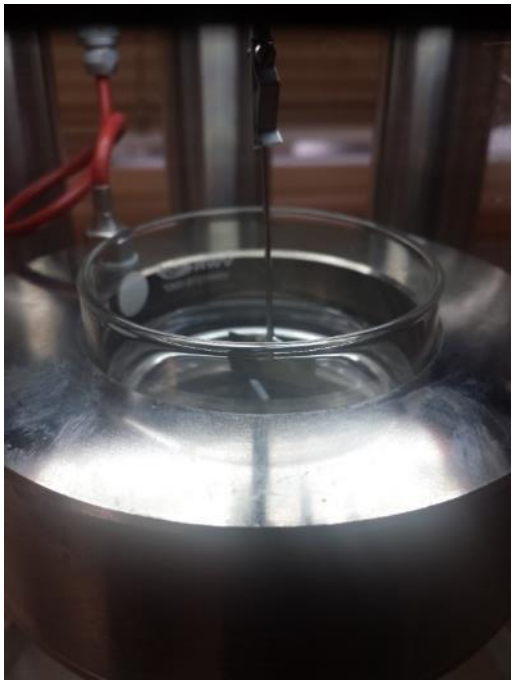

Figure 26 - Inner chamber of the DCAT11 tensiometer, with attached Wilhelmy plate, during a measurement.

From the surface tension curves, one can gather relevant parameters, such as the surface tension of the dispersion at the *cmc*, the maximum surface excess concentration, Γ_{max} (page 34) and the minimum surface area per molecule, a_{Smin} (page 34).

2.2.2.1 Calculating the cmc

The surface tension obtained was plotted versus the natural logarithm of surfactant molal concentration.

The critical micelle concentration (*cmc*) was determined by intersecting two linear regressions of two sets of data points, the first one being the set that contains the data points that form a regression with the highest slope and the second the set contains the data points at which the surface tension is stabilized (referred as the surface tension plateau), as graphically exemplified below (Figure 27). The concentration at this point of intersection yields the *cmc.*

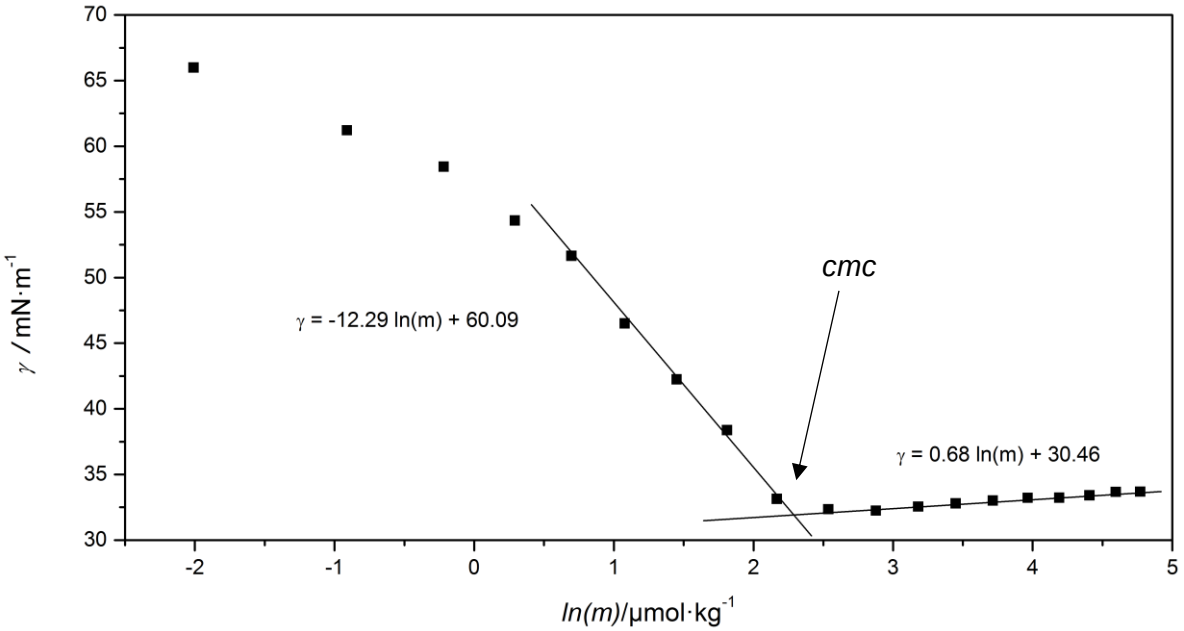

Figure 27 - Graphical example of the method used to calculate the *cmc*.

2.2.2.2 Maximum surface excess concentration

Surface excess concentration is the excess concentration of surfactant molecules adsorbed at the air-water interface, within the Gibbs ideal model and as defined by the Gibbs isotherm (eq. [10]).

$$\Gamma_i = \frac{n_i^{\sigma}}{A} \qquad [\ 10\ ]$$

This parameter was calculated by using the highest slope obtainable in the curve and applying it to eq. [11], where *n* is the number of chemical species considered; *n*=2 for a partial counter-ion dissociation of the cationic surfactant, while *n*=3 is used for a full dissociation and the three species coexist.

$$\Gamma = -\frac{1}{nRT} \cdot \frac{d\sigma}{d \ln c} \qquad [\ 11\ ]$$

2.2.2.3 Minimum superficial molecular area

This parameter is the minimum area a surfactant molecule occupies at the liquid's surface. It is useful to determine if the surfactant in question has the hydrocarbon chain turned upwards or is lying longitudinally on the surface, among other diverse configurations, situations which have distinctive molecular areas occupied. It is calculated using Γ_{max} and the Avogadro's number (N_A), as shown in following equation (eq. [12]).

$$a_{S_{\min}} = \frac{1}{N_A \Gamma_{\max}} \qquad [\ 12\ ]$$

2.2.2 Dynamic Light Scattering

The Dynamic Light Scattering (DLS) is a technique commonly used to determine the fluid dynamics and particle sizes of colloidal systems.

DLS works by making a laser beam, typically originated from Helium-Neon or Argon excitation, hit the desired colloidal sample. The light from this beam is then scattered by the particles in suspension and detected at an angle, θ, to the incident beam (Figure 28). This scattered light has an intensity dependent on size and Brownian motion of particles, fluctuating over time[78-79].

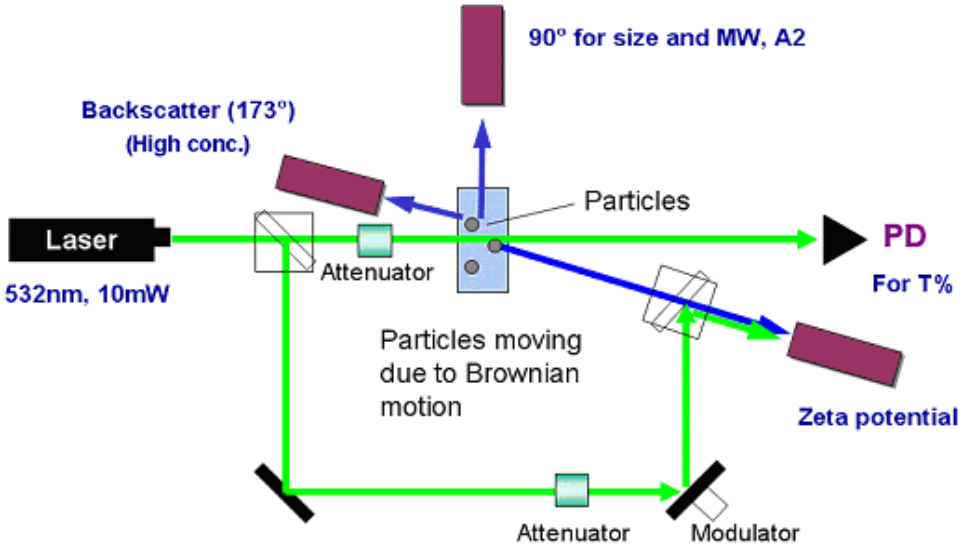

Figure 28 - Schematic of the dynamic light scattering measuring system. From ref[1].

This scattered light is then analysed by an autocorrelator that generates a function g(τ), the auto-correlation function, enabling the determination of the diffusion coefficient D (eq. [13]) for monodisperse populations of particles. [79]

$$g(\tau) = e^{-Dq^2\tau} \qquad [\ 13\ ]$$

In this equation *q* represents the scattering vector, which depends (eq. [14]) on the solvent's refractive index (*n*), the wavelength of incident light (λ_0) and the scattering angle (θ).[79]

$$q = \frac{4\pi n}{\lambda_0} \sin\frac{\theta}{2} \qquad [\ 14\ ]$$

The diffusion coefficient D can then be used to calculate the hydrodynamic radius (R_H) of the particles by the Einstein-stokes equation (eq. [15]), where K_B is the Boltzmann constant, T is the absolute temperature, and η the solvent's viscosity.[79]

$$D = \frac{K_B T}{6\pi\eta R_H} \qquad [\ 15\ ]$$

However, for polidisperse particle populations which are more common, this calculation method cannot be used as it is. In polidisperse populations the diffusion coefficient must take in account various particle sizes and diffusion modes[78, 80]. The most common way to obtain the diffusion coefficient in this case is to use the cumulants method, which uses a monoexponential correlogram fit to calculate the Z-average diameter and the polydispersity index (PDI), an estimate of the population polydispersity[81].

This technique has the limitation of assuming that every particle it measures is spherical, which may induce error in some situations, such as the measurement of elongated aggregates and any other non-spherical particle.

Experimental procedure

The DLS measurements in this work were carried out in a Zetasizer Nano ZS machine, from Malvern Instruments. Each sample was prepared immediately before the measurement, directly inside the cuvette to prevent contaminations and reduce the time between preparation and measurement. They were measured at a scattering angle of 173° known as backscatter analysis. Data was processed using Malvern's Dispersion Technology Software (DTS).

2.2.3 Zeta Potential

Dispersed particles have a net charge that depends on the composition of said particle and affects the positioning of ions from the dispersion medium around them, forming an electrical double layer. The first and inner layer is called the Stern layer, where ions are strongly bound to the particle. The next layer is more diffuse with the ions more weakly bound. The interface between this outer layer and the dispersion medium is called the slipping plane[82].

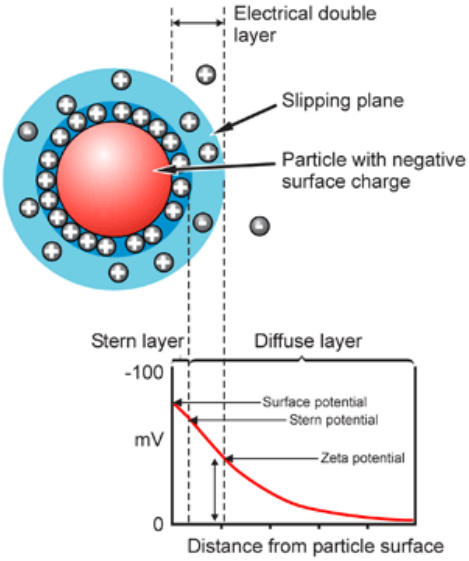

Figure 29 - Various layers of charges acquired by a particle and the corresponding interlayer interfaces. From ref[1].

The zeta potential is the electric potential between the slipping plane of a dispersed particle and the dispersion medium, that is created when the particle experiences motion. It can be either negative or positive, depending on the particle's charge[82-83].

This potential can be used as a measure of stability of a colloidal dispersion, since a higher modulus of the zeta potential signifies a higher repulsive force between identical particles with the same charge, preventing aggregation[84].

A modulus between 0 mV and 5 mV signifies that the particles will quickly aggregate, while moderate stability is only achieved from a modulus of 30 mV, with stability increasing as the modulus increases. This property can be measured by determining the electrophoretic mobility (velocity of a particle in an electrical field) of the particles, by the laser Doppler velocimetry. This is then calculated using the Henry's equation (eq. [16]), where U_E is the electrophoretic mobility, z is the zeta potential and f*(ka)* the Henry's function. By the Smoluchowski approximation the Henry's function has

a value of 1.5 for aqueous solutions, and by Hückel approximation a value of 1 for non aqueous solutions[82, 84].

$$U_E = \frac{2\varepsilon z f(ka)}{3\eta} \qquad [16]$$

Experimental procedure

Figure 30 - U-shaped cuvette with electrodes used for zeta potential determination.

Zeta potential determinations were also made in the Zetasizer Nano ZS by Malvern instruments. Each sample was prepared immediately before each measurement. One milliliter of each sample was transferred to a U-shaped cuvette with electrodes from Malvern Instruments (Figure 30) and left to reach thermal equilibrium inside the equipment for two minutes. Zeta potential was then measured at a scattering angle of 17°.

Data was processed using Malvern's Dispersion Technology Software (DTS).

2.2.4 Light Microscopy

Bright field microscopy was used for the morphological analysis of the aggregates in this work. This type of microscopy involves direct observation of an amplified image of the samples, backlighted by visible light, outputted through a series of lenses. This amplified image has a high resolution and high contrast between the objects and background, allowing the resolution of more details.

The image obtained by this type of microscopy cannot be amplified indefinitely, having a finite resolution defined by three major components: the quality of the lenses, the wavelength of the light source used and the aperture of the objective.

The quality of the lenses depends on the structural quality and purity of the glass and the precision of the geometry (such as curvature) of the finished lens.

The dependency of the resolution with the light's wavelength and numerical aperture is given by the following equation (eq. [17]).

$$R = \frac{\lambda}{2NA} \qquad [\ 17\ ]$$

Where R is the resolution (in *nm*) and NA is the numerical aperture.

Since the studied samples have very low contrast due to almost complete absence of colour, two techniques, derived from the use of polarized light were used to overcome this problem, as discussed further.

This was done in an Olympus BX51 microscope, linked to an Olympus C5060 digital camera. The samples were sealed between a slide and coverslip using a fast drying hydrophobic compound to prevent evaporation and contamination during the analysis.

Figure 31 - Olympus BX51 optical microscope used in this work.

2.2.4.1 Polarized light microscopy

Regular polarized light microscopy allows portions of the sample which have anisotropic optical qualities to be detected, because of their birefringence. Birefringence exists due to fact that the sample has a refractive index dependent on the polarization and direction of propagation of light. This property is present in many materials and crystals under stress, but also on self-assembled surfactant structures, such as bilayers and some liquid crystals.

This technique works by passing a beam of polarized light, obtained through a polarizing filter after the source, through the sample (Figure 32). This polarized light then passes through another filter before going into the microscope's lenses. The second filter only allows light that was interfered with by the sample (acquiring a different polarization plane due to the varying refractive indexes). Birefringent samples modify the polarized light by turning it into two separate waves with perpendicular planes.

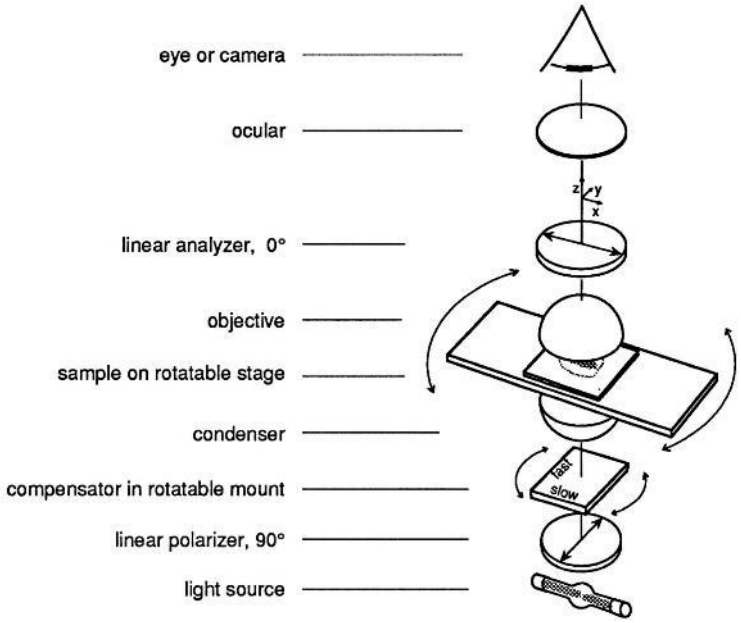

Figure 32 - Schematic of the working of a polarized light microscopy system. From ref[85].

2.2.4.2 Differential interference contrast microscopy

Differential interference contrast microscopy (DIC) uses a double beam of polarized light, created by the *Normarski* prism, to interact with the sample. These two beams are then recombined by the DIC prism immediately before the second filter. The two beams are separated by a small distance, allowing them to interact with the sample and to suffer interference in slightly different ways. Due to this, once the beams are recombined the image becomes slightly three-dimensional, increasing contrast with the background.

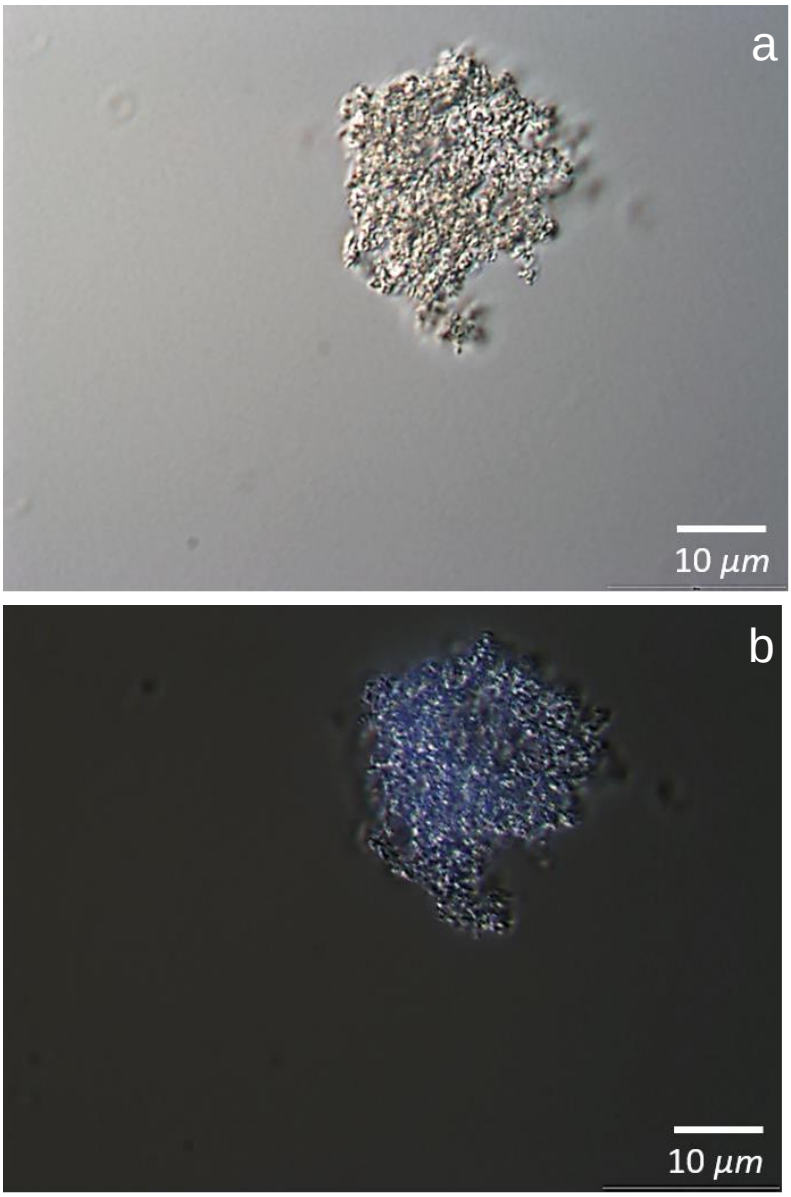

Figure 33 - Comparison between images obtained by the DIC (a) and regular polarized light (b) techniques. It should be noted in (b) the blue zones that sign the presence of birefringence. Images from $(18Ser)_2N12$ binary complexes.

2.3 Biological studies

2.3.1 Cell Line and Culture Conditions

The biological assays were performed in the immortal human epithelial cervical carcinoma (HeLa) cell line, derived from cervical cancer cells originally taken from a patient in 1951.

The cell culture (Figure 34) was maintained at 37°C, in 5% CO_2, in Dulbecco's Modified Eagle's medium-high glucose (DMEM-HG, Sigma Aldrich) supplemented with 10% (v/v) heat inactivated fetal bovine serum (FBS) and 100 units of penicillin and 100 µg of streptomycin per mL.

Cells grown adherent in monolayers at 50–70% confluence were detached by treatment with 0.25% trypsin solution (Sigma Aldrich) and split every two or three days, Cell suspensions were diluted 1:1 with trypan blue and cells were counted using a haemocytometer.

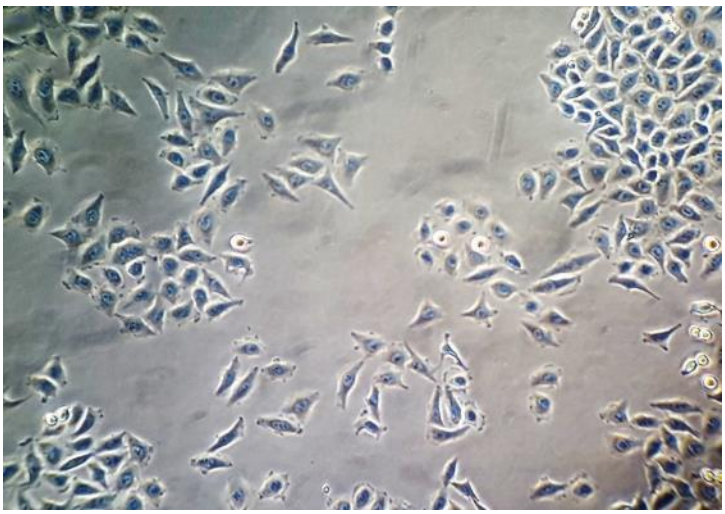

Figure 34 – Microscopy image from one of the HeLa cell cultures, used in this work.

For the following experiments, cells were seeded in 12-well plates ($8x10^4$ cells per well) 24 hours prior to transfection with the gemini-based complexes.

2.3.2 Preparation of gemini surfactant-based complexes

Surfactant-based complexes were prepared using a GFP-encoding plasmid DNA (mtDNA), specifically expressed in mitochondria.

The gemini surfactants comprised two amine series with different spacer lengths of 5 and 12 carbons, both with alkyl chain lengths of 12, 14, 16 and 18 carbons.
For each gemini surfactant, aqueous solutions at a concentration of 0.5 mM were prepared and then filtered through 0.2 µm pore diameter filters (Schleicher and Schuell).

Helper lipid dispersions were prepared using 1,2-dioleoyl-sn-glycero-3-phosphoethanolamine (DOPE) and cholesterol (Chol) (Avanti Polar Lipids) dissolved in chloroform, mixed at 2:1 molar ratio, and then dried under vacuum in a rotary evaporator. The dried lipid films were hydrated with HBS at pH 9.0, resulting in the formation of vesicles, at a final lipid concentration of 0.5 mM, which were then filtered through a 0.2 µm pore diameter filter.

Plain complexes, composed of gemini surfactant and plasmid DNA, were produced by mixing aliquots of mtDNA with the previously prepared gemini surfactant solutions, to achieve 3 distinct gemini surfactant/DNA (+/-) charge ratios: 8/1, 10/1 and 12/1, following incubation at room temperature for 15 min to allow complex formation.

Ternary complexes, composed of gemini surfactant, mtDNA and helper lipids (DOPE:Chol), were prepared by adding the HL dispersion to the plain complexes to achieve a 1:1 surfactant:HL molar ratio.

All complexes were allowed to incubate for further 30 minutes at room temperature to allow full stabilization.

2.3.3 Cell Transfection

Binary gemini surfactant/mpDNA, or ternary gemini surfactant/mpDNA/HL complexes were added to each well (0.5 µg mtDNA per well) in the previously seeded 12-well plates, in serum-free OptiMEM medium and left to incubate at 37°C and 5% CO_2 for 4 hours. After the transfection period, the medium containing the complexes was replaced by complete DMEM medium, and the cells were let to incubate for further 44 hours.

2.3.4 Evaluation of mtDNA expression

Transfection efficiency mediated by the gemini surfactant-based complexes was evaluated using flow cytometry to determine the percentage of cells expressing GFP. Flow cytometry allows for the simultaneous measurement and analysis of multiple physical characteristics of cells, including relative cell size, granularity and fluorescence intensity, as individual cells pass through a focused laser beam.

Forty-eight hours after transfection, cells from each well were washed once with PBS buffer and detached with 0.25% trypsin solution (Sigma Aldrich) at 37°C and 5% CO_2 for 10 minutes. Cells were further washed three times by centrifugation (200 g, 4°C, 5 minutes) in ice-cold PBS, and immediately analysed by flow cytometry.

Flow cytometry was performed in a FACScalibur flow cytometer (BD Biosciences) and data gathered by CellQuest software were processed using FlowJo software. Live cells were gated by forward/side scattering from a total of 10,000 events, which were further gated by GFP fluorescence, which determines transfection success.

Transfection efficiency was determined as a percentage of cells expressing GFP from the total of viable cells (eq.[18]).

$$Transfection\ efficiency(\%) = \frac{\text{Number of GFP expressing cells}}{\text{Number of viable cells}} \times 100 \qquad [\ 18\ ]$$

2.3.5 Evaluation of Cell Viability

Cell viability was assessed in parallel with transfection efficiency, to correlate the cytotoxicity promoted by the gemini surfactant-based complexes with the length of the spacer and alkyl chain of the gemini surfactants.

The test used to determine cell viability was a modified Alamar Blue assay[86]. In this assay, resazurin (dark blue) is reduced to resorufin (pink) (Figure 35), which is highly fluorescent, by metabolically active cells. The redox capacity of the cells is a measure of their viability, thus being possible to assay cytotoxicity of compounds incubated with the cells by how much resazurin they reduce.

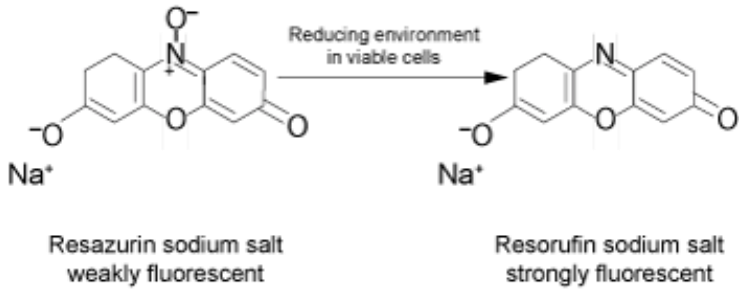

Figure 35 - Resazurin reduction reaction. From ref[1].

After 48 h of incubation with the gemini complexes, the medium was replaced with 0.4 mL of 10% resazurin dye in complete DMEM medium and cells were let to incubate at 37°C in 5% CO_2 for 45 minutes. After the allotted time, 180 µL of the supernatant were collected from each well and placed in a 96-well plate (Figure 36). The absorbance of the supernatant was measured at 570 nm and 600 nm in a SPECTRAmax PLUS 384 spectrophotometer (Molecular Devices). It should be noted that for the Alamar Blue assay one can also use the values of fluorescence, instead of absorbance.

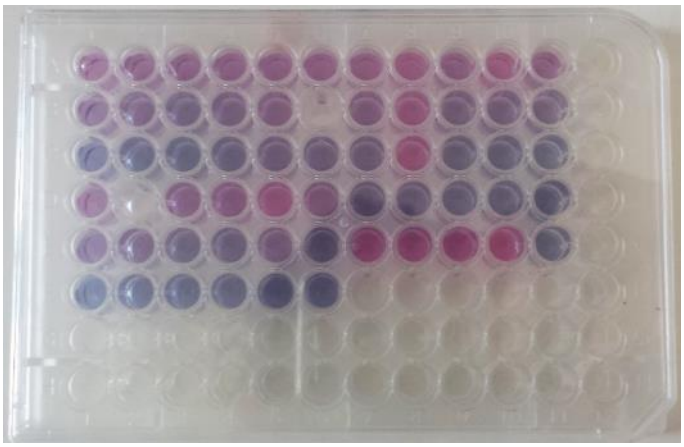

Figure 36 – Example of cell viability assay supernatants after 45 minutes of incubation, in a 96-well plate. The colour of the wells represents the cytotoxicity of the complexes; the more pink a supernatant in the well is, the less cytotoxic was the complex.

Cell viability was calculated as a percentage of the control cells (nontreated), using the following equation (eq. [19]), where A_{570} and A_{600} are the absorbances of the samples and A'_{570} and A'_{600} are the absorbances of the control, at the respective wavelengths.

$$cell\ viability\ (\%\ of\ control) = \frac{A_{570} - A_{600}}{A'_{570} - A'_{600}} \times 100 \qquad [\ 19\ ]$$

Chapter 3: Results and discussion

3.1 Synthesis yields

All gemini surfactants were successfully synthesized in this work according to the procedure described in section 2.1, with the exception of $(12Ser)_2N12$, which already existed in stock and was analysed for its purity.

Table 1 - Full reaction yields for each of the synthesized gemini surfactants and the corresponding structures.

Gemini	***Yield (%)***
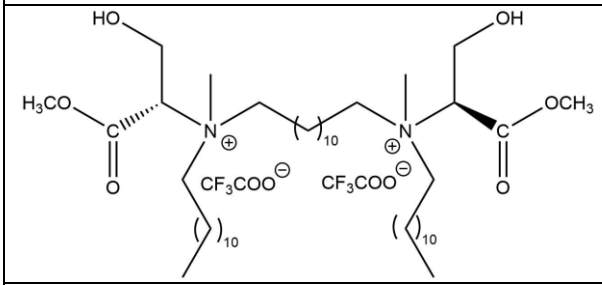 $(12Ser)_2N12$	--*
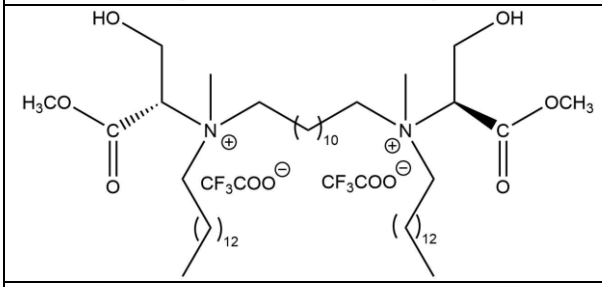 $(14Ser)_2N12$	5.5
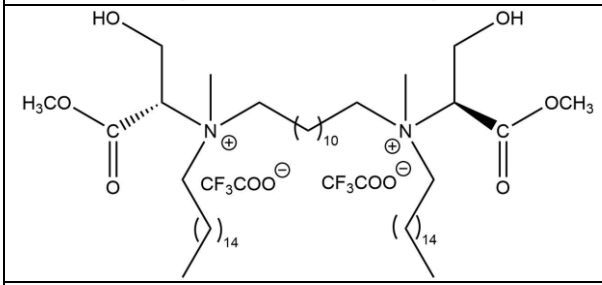 $(16Ser)_2N12$	16.8
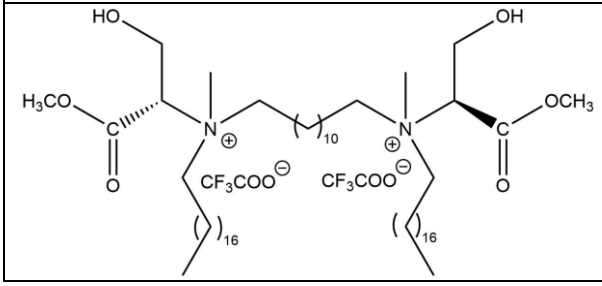 $(18Ser)_2N12$	8.6

*Synthesis not realized in this project. Analysed by NMR before use.

The synthesis yielded high purity products, even though column chromatography purification for the various products of this synthesis pathways was somewhat difficult to complete. The low yields obtained are expected and result of the high complexity of the synthesis process and the need for intermediate purification between each step

3.2 Interfacial and aggregation properties

3.2.1 Determination of *cmc*

Critical micelle concentration was determined by the Wilhelmy plate method, as described in section 2.2.1. Measurements were performed at both 25°C and 40°C to determine if temperature had a significant influence on the cmc calculated.

The method of calculating the *cmc* from chapter 2.2.2.1 was applied to the following data sets (Figure 37 to Figure 40).

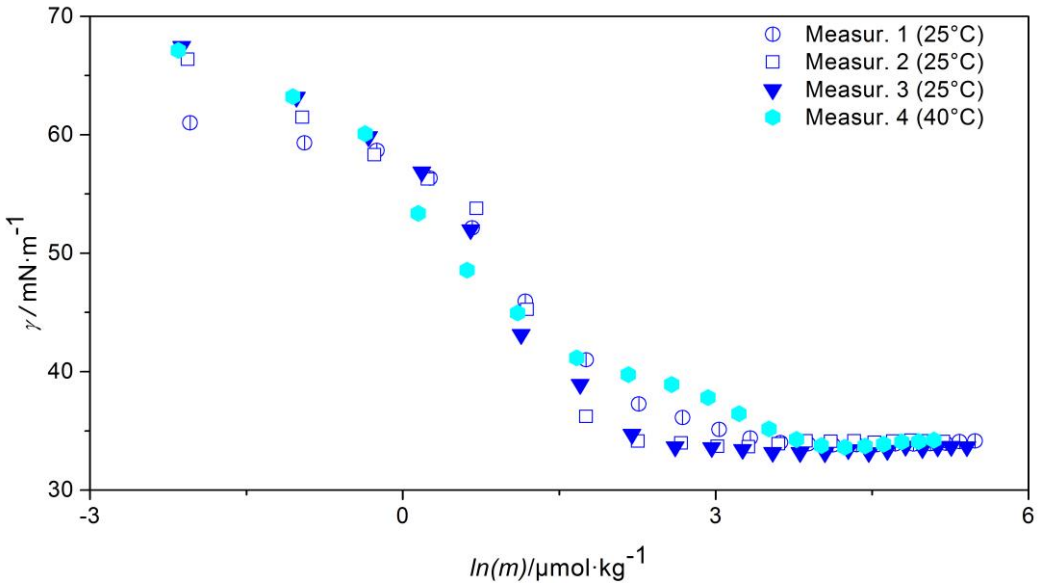

Figure 37 - Data plots for the Whilhelmy plate surface tension experiments for the gemini $(12Ser)_2N12$. Separated by temperature.

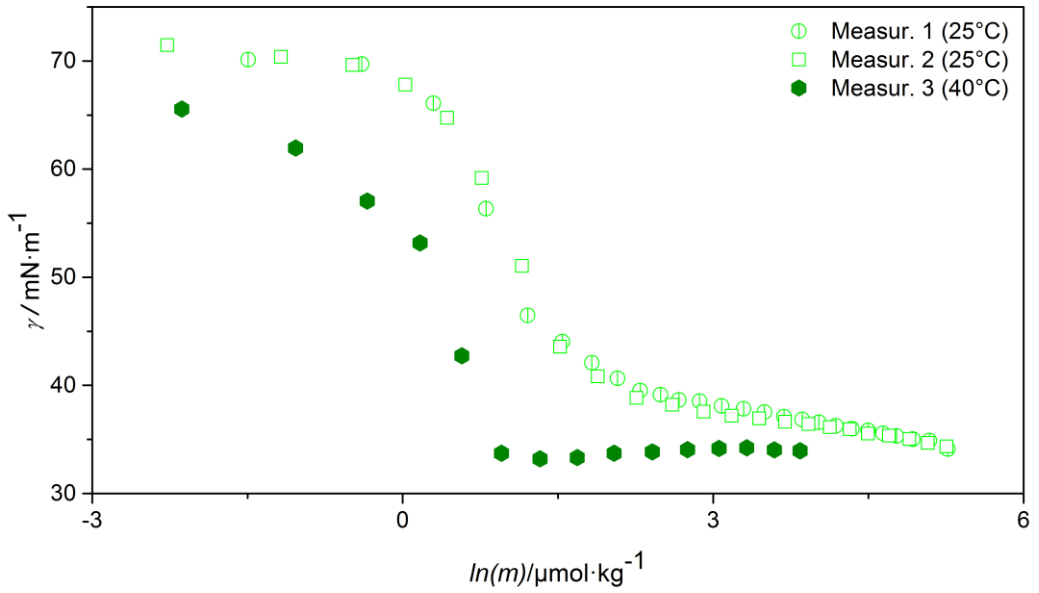

Figure 38 - Data plots for the Whilhelmy plate surface tension experiments for the gemini $(14Ser)_2N12$. Separated by temperature.

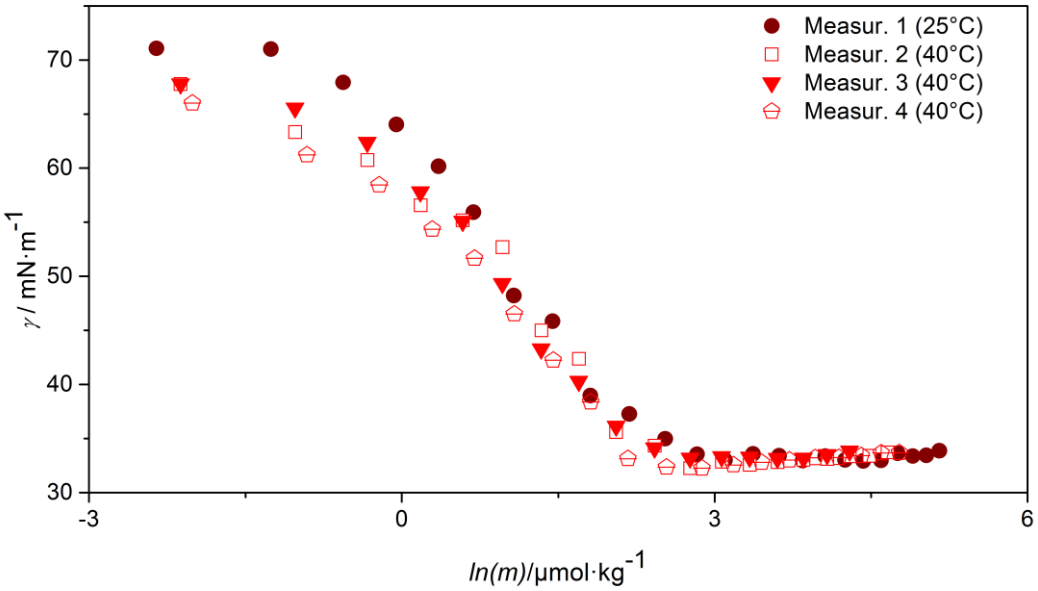

Figure 39 - Data plots for the Whilhelmy plate surface tension experiments for the gemini $(16Ser)_2N12$. Separated by temperature.

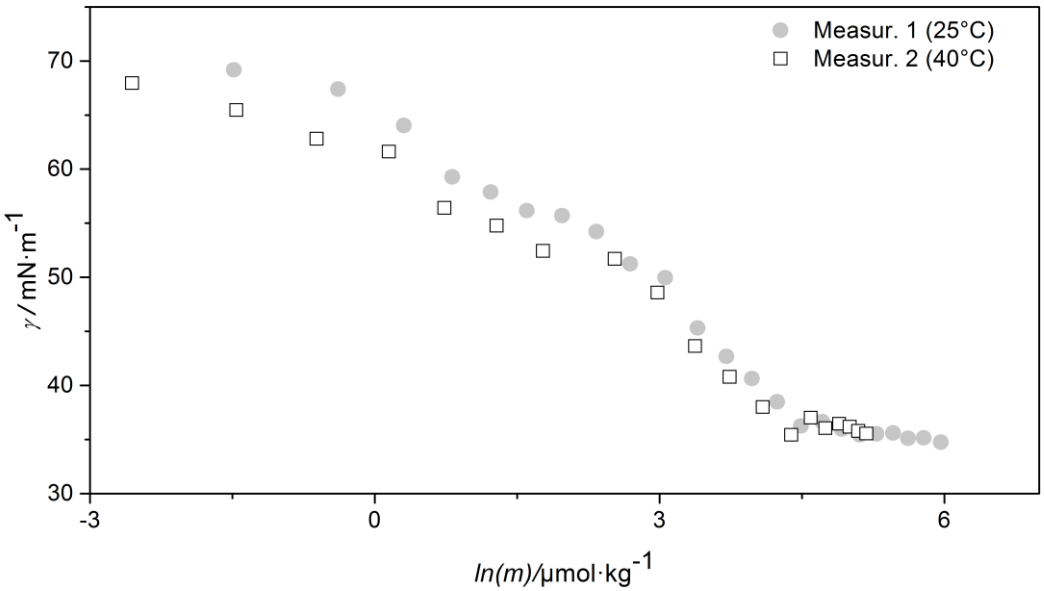

Figure 40 - Data plots for the Whilhelmy plate surface tension experiments for the gemini $(18Ser)_2N12$. Separated by temperature.

It is possible to observe that the various gemini have a different behaviour in solution, since the tensiometric curves have a distinct profile depending on the gemini and on the temperature. The temperature effect is more evident in Figure 37 and Figure 38.

Considering the graphs for the various gemini surfactants, one can observe that the curves for $(14Ser)_2N12$ were the less reproducible ones, at both temperatures.

Table 2 summarizes the results of all measurements for the four gemini surfactants.

Table 2 – Summary of data from surface tension studies of the entire $(nSer)_2N12$ gemini series. Includes temperature, critical micelle concentration, surface tension at *cmc*, maximum excess superficial concentration and minimum molecular area, in order.

Gemini	θ /°C	*cmc* /µmol.kg^{-1}	γ_{cmc} /mN.m^{-1}	Γ_{max} x 10^{-6} /mol.m^{-2}		a_{Smin} /nm^2	
				n=2	n=3	n=2	n=3
$(12Ser)_2N12$	25	10.1 ± 1.3	33.88 ± 0.23	2.10	1.40	0.791	1.187
				2.34	1.56	0.710	1.065
				2.27	1.51	0.732	1.097
	40	11.6*	33.86*	1.86	1.24	0.894	1.340
$(14Ser)_2N12$	25	4.82 ± 0.68	35.28 ± 0.75	4.32	2.88	0.385	0.577
				4.33	2.89	0.383	0.575
				3.95	2.63	0.421	0.631
	40	2.9*	33.84*	3.72	2.48	0.447	0.670
$(16Ser)_2N12$	25	10.5*	33.24*	2.63	1.75	0.632	0.948
	40	10.8 ± 0.9	33.16 ± 0.17	2.48	1.65	0.670	1.005
				2.56	1.71	0.649	0.973
				2.32	1.55	0.716	1.074
$(18Ser)_2N12$	25	84.4*	35.27*	1.92	1.28	0.867	1.300
	40	70.4*	37.01*	1.83	1.22	0.907	1.360

*Single measurement.

All cmc_s obtained are within the expected concentration range for this kind of compounds.

From the $(12Ser)_2N12$ to $(14Ser)_2N12$ the usual surfactant hydrocarbon chain length/*cmc* trend seems to manifest, albeit in a reduced manner, with only a *cmc* decrease at about 50%. From there however, it inverts, with the *cmc* increasing with the length of the carbon chains.

3.2.2 Trends in *cmc* and comparison with previous studies

Previous works on serine derived gemini surfactants have shown a decrease in the *cmc* as the hydrocarbon chain length increases[61](Figure 41), which is a typical behaviour for surfactant systems. It can also be observed a decrease in the *cmc* with the increase in the spacer length, for both the conventional bis-quat gemini surfactant series and the $(nSer)_2N5$ series (Figure 41).

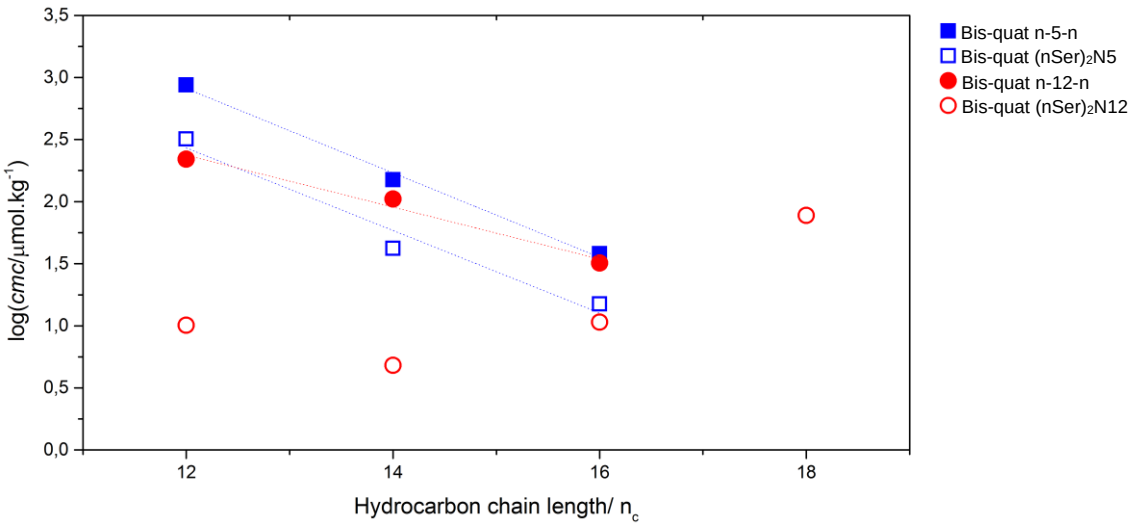

Figure 41 - Logarithm of cmc vs. hydrocarbon chain length for conventional gemini with a spacer of 5 carbons (Bis-quat n-5-n)[71, 87-88], serine derived gemini with a spacer of 5 carbons (Bis-quat $(nSer)_2N5$)[61], the conventional gemini with a 12 carbons spacer (Bis-quat 12-12-12)[71, 89] and the serine derived gemini series with a 12 carbons spacer studied in this work (Bis-quat $(nSer)_2N12$).

Differential Scanning Calorimetry (DSC) measurements were performed for the gemini surfactants synthesized, and no phase change was found between 10°C and 90°C, at 3 mM concentration, thus Krafft temperature for the compounds is below the temperatures used for preparation of samples and posterior measurements.

The critical micelle concentration is known for decreasing as the hydrocarbon chain of a surfactant increases in length. This trend is caused by the increased hydrophobic effect of the longer hydrocarbon chains[90]. This relationship is kept in gemini surfactants, even amino-acid derived, with higher decreases in *cmc*, but surprisingly the trend is not observed in the whole $(nSer)_2N12$series studied here.

The trend seems to manifest at the beginning of the series, with the *cmc* decreasing from $(12Ser)_2N12$ and $(14Ser)_2N12$ (by a factor of about 2), but increases at $(16Ser)_2N12$ (by a factor of about 2) and again at $(18Ser)_2N12$ by a much larger factor of about 8. This break in the trend does not occur in similar series of serine derived gemini, like $(nSer)_2N5$[61] (Figure 41), but the effect cannot be fully attributed to the

different spacer without further testing. This irregular variation could have its origin in the difficulty of measuring the surface tension by tensiometric methods due to these surfactant's complex surface dynamics. These complex surface dynamics could possibly be caused by the long spacer containing in these gemini and its interference in the interaction between the positively charged headgroups. Thus, tensiometric studies were realized at higher temperature (40°C), which did not significantly change the *cmc* value, asserting the fiability of the results.

Curiously, a similar variation of the trends was observed in a previous study[91], suggesting that the inversion in the decreasing *cmc* trend can be attributed to hydrophobic interactions between very long hydrocarbon chains present in the gemini, which would cause them to coil around each other. This "self-coiling", as the author refers, would cause an increase in the energy needed to separate the coiled carbon chains so that the gemini could be part of an organized self-assembled structure, such as a micelle or liposome. The energy increase would hinder the adaptation of the system, thus increasing the number of surfactant molecules needed for the formation of structures, meaning an increase in the *cmc*. However, this hypothesis could not be verified without a more extensive study.

3.3 Biological studies

3.3.1 Cell viability

Gemini surfactants of both $(nSer)_2N12$ and $(nSer)_2N5$ series were tested for their cytotoxicity.

In these assays both binary (without HL) and ternary (with HL) complexes were used, in order to determine if the helper lipid formulation would increase biocompatibility.

As observed, addition of the DOPE:Chol helper lipids (identified by “HL” in the Figures) to binary complexes promoted a decrease of the cytotoxicity (Figure 42 and Figure 43).

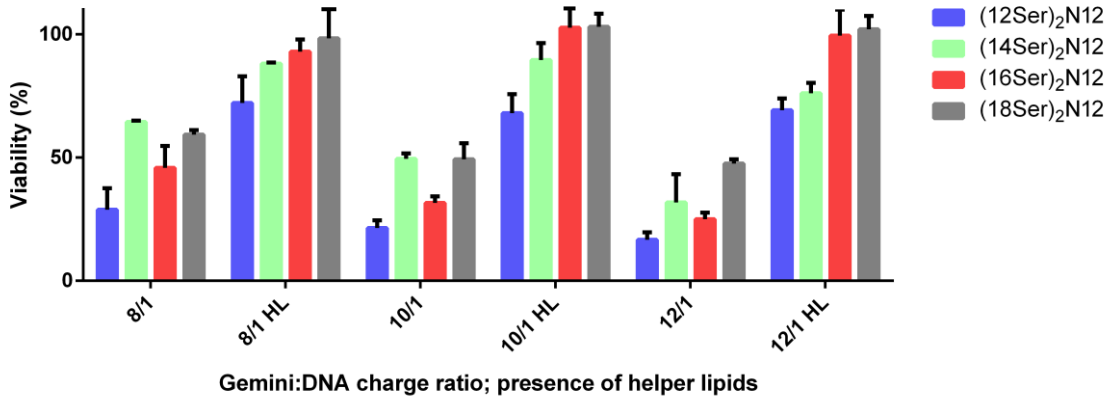

Figure 42 – HeLa cell viability 48 h after transfection with mtDNA complexes based on surfactants of the $(nSer)_2N12$ gemini series, prepared in the presence or absence of the helper lipids DOPE:Chol (HL), as assessed by the Alamar blue assay.

Considering the different charge ratios of gemini/DNA, the data show, that for binary complexes, the higher the ratio, the lower the cell viability, while the presence of the helper lipid did not result in significant effect in this trend. As it can also be observed, for each (+/-) charge ratio, both with and without HL, the cell viability increases with increasing hydrocarbon chain length of the gemini surfactant, except for binary complexes prepared from $(14Ser)_2N12$ gemini surfactants (Figure 42), which seem to be less toxic than those with longer hydrocarbon chain length, at all charge ratios.

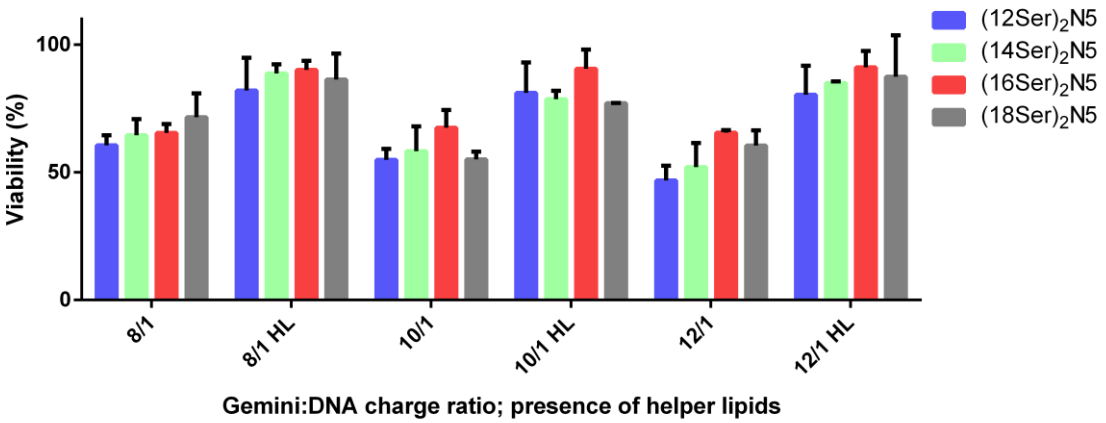

Figure 43 - HeLa cell viability 48 h after transfection with mtDNA complexes based on surfactants of the $(nSer)_2N5$ gemini series, prepared in the presence or absence of the helper lipids DOPE:Chol (HL), as assessed by the Alamar blue assay.

$(nSer)_2N5$ series promoted a larger decrease in cell viability than the $(nSer)_2N12$ series in the presence of HL, as opposed to the smaller decrease observed in the absence of HL.

For ternary complexes, no clear trend can be observed, both in terms of charge ratio and hydrocarbon chain length, whereas binary complexes show a slightly decrease cell viability with the increase in charge ratio (Figure 43).

It is also worth mentioning that the $(16Ser)_2N5$-based complexes seem to promote less loss of cell viability over the charge ratio range evaluated, being more noticeable for cells transfected with the binary complexes.

3.3.2 Transfection efficiency

Similar to the viability assay, for the transfection efficiency determination, the $(nSer)_2N5$ series (Figure 45) was also tested for control purposes.

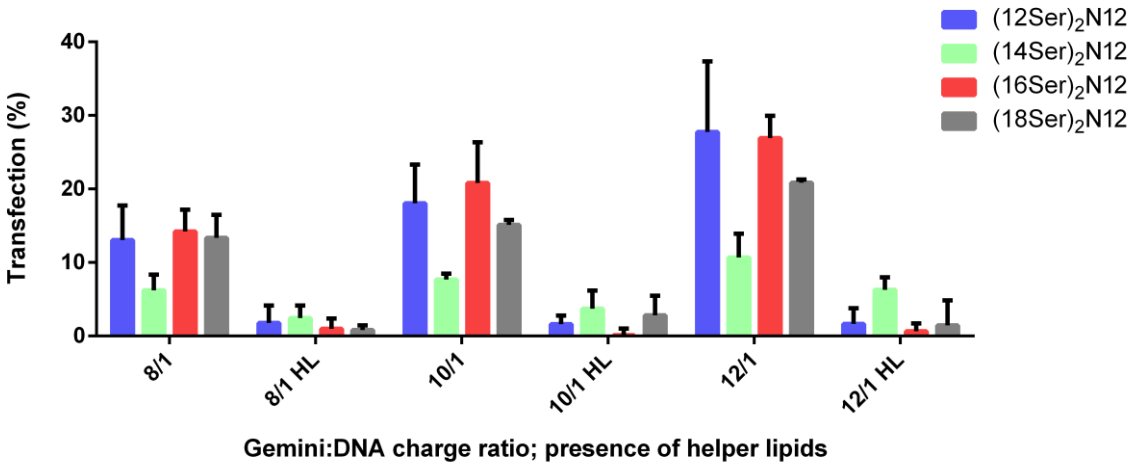

Figure 44 -Transfection efficiency, determined in terms of percentage of HeLa cells transfected with mtDNA complexes based on gemini surfactants of the $(nSer)_2N12$ gemini series, prepared in the presence or absence of the helper lipids DOPE:Chol (HL), as assessed by flow cytometry.

The most striking feature in this data set is the very low transfection efficiency obtained with the complexes containing HL. The $(14Ser)_2N12$ complexes are outside this trend, especially at the highest charge ratio, having a much larger transfection efficiency than the complexes formed by other gemini surfactants. However, its transfection efficiency is still low.

This low efficiency may be related with the potential “protective” effect conferred by the helper lipids, which is reflected in the high viability of cells transfected with the ternary complexes (Figure 41). In fact, if the helper lipids contribute to decrease the interaction between the complexes and the surface of the cell membranes, the predictable outcome is a lower cytotoxicity, but also a lower internalization and efficiency of the complexes. Further studies are necessary to disclose this possibility.

For binary complexes, the transfection efficiency increases with the increase of the (+/-) charge ratio, although this trend is less noticeable for the $(14Ser)_2N12$–based complexes. $(12Ser)_2N12$ and $(16Ser)_2N12$ seem to be the most efficient transfection compounds, which is more notorious for complexes prepared at higher charge ratios.

Since the evaluation of transfection excludes non-viable cells, efficiently transfected cells correspond to a small percentage of the whole cell population. Additionally, for a safe administration in an in vivo application, more than 20-30%

reduction in cell viability, caused by unspecific toxic effects of the transfection process, is undesirable and pose a risk to the patient.

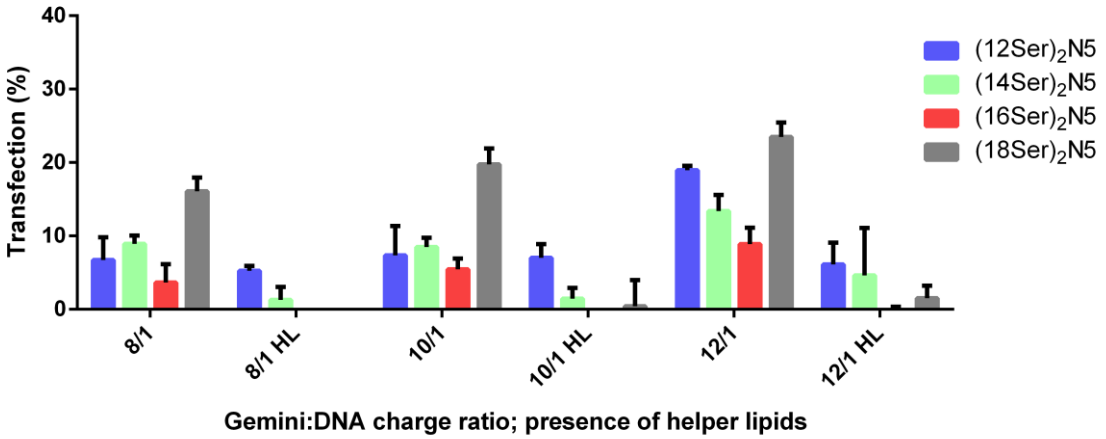

Figure 45 - Transfection efficiency, determined in terms of percentage of HeLa cells transfected with mtDNA complexes based on gemini surfactants of the $(nSer)_2N5$ gemini series, prepared in the presence or absence of the helper lipids DOPE:Chol (HL), as assessed by flow cytometry.

Complexes prepared with the $(nSer)_2N5$ gemini surfactants present an overall lower transfection efficiency than those prepared with the (nSer)2N12 gemini surfactant series. The nearly null transfection efficiency observed with the 12 carbon spacer is maintained in this series, for complexes with HL, with the exception of the $(12Ser)_2N5$ gemini surfactant, which, for the highest (+/-) charge ratio tested, mediates transfection in 20% of the cells.

In the absence of HL, a decrease of the transfection efficiency was observed with the increase of the hydrocarbon chain length (particularly at the (+/-) charge ratio of 12/1). However, the transfection efficiency increased markedly when the hydrocarbon chain length reached 18 carbons, being more than double the efficiency, when compared to a chain length of 16 carbons.

Overall, the transfection efficiency for both series is relatively low. The gemini surfactants able to mediate the highest levels of transfection with reasonable efficiencies being those prepared from $(18Ser)_2N5$ (Figure 45), $(12Ser)_2N12$ and $(16Ser)_2N12$ (Figure 44). However, these gemini surfactant-based formulations were also those that promoted extensive loss of cell viability (Figure 42 and Figure 43).

3.3.3 Transfection efficiency *vs.* cellular viability

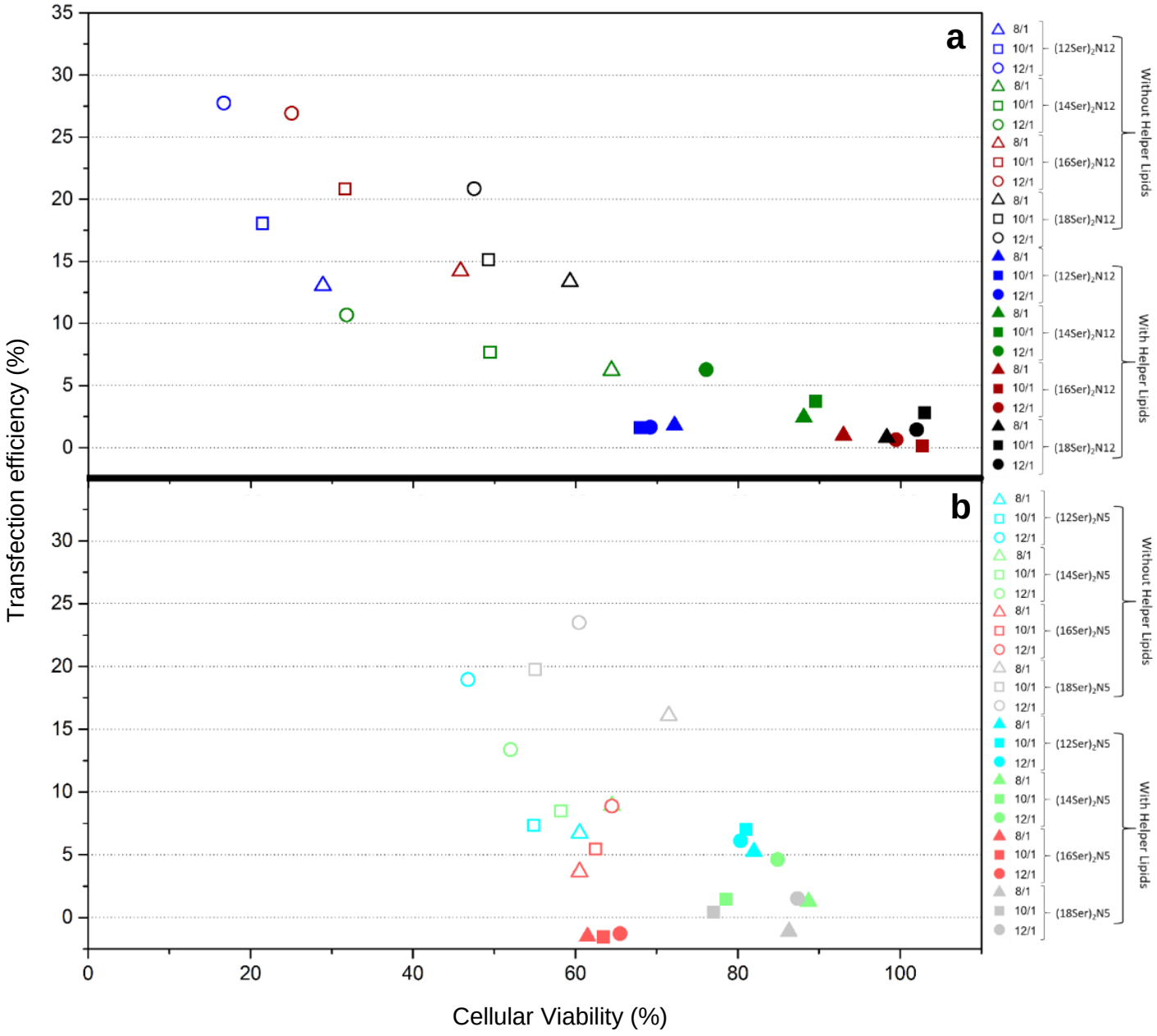

Figure 46 - Transfection efficiency VS Cellular viability for both series of gemini surfactants, $(nSer)_2N12$ (a) and $(nSer)_2N5$ (b), for all three gemini:DNA charge ratios considered, with and without HL.

In the graphs in Figure 46 one can observe that the $(nSer)_2N5$ gemini series has a lower dispersion of cellular viability values across the entire sample spectrum (Figure 46 **b**) than the $(nSer)_2N12$ series. This series with the 5 carbon spacer also has the 2 data points with the highest transfection/viability ratio of both series (8/1 and 12/1 $(18Ser)_2N5$).

Data points from the $(nSer)_2N12$ series are much less clustered (Figure 46 **a**), suggesting more different behaviours between each surfactant of the series. However, it is in this series that the highest transfection efficiency (12/1 $(12Ser)_2N12$) and highest cellular viability (12/1 $(18ser)_2N12$ HL) are achieved.

In both series the data points of the samples containing helper lipids are more clustered together than those without, suggesting that the presence of HL somewhat masks the intrinsic properties of each surfactant.

3.3.4 Comparison with previous studies

Previous studies have been performed for the $(nSer)_2N5$ gemini series, up to a gemini:DNA charge ratio of 8/1, showing several trends.

In first place there is a decrease in cellular viability with the growth of the hydrocarbon chains length and the increase in charge ratio[59], while there is an increase in the transfection efficiency with the growth of the hydrocarbon chains length and the increase in charge ratio[59].

It is also reported an increased transfection efficiency in complexes, for most of the charge ratios, containing HL[59-60] than the charge ratios studied in this work;

This suggests a high dependence between gemini:DNA charge ratio and transfection, with lower charge/ratios being more beneficial for this series.

3.4 Lipoplex characterization

3.4.1 Size stability studies

Due to the detection of visible aggregation in preliminary samples, the size stability over time (1.5 hours) was evaluated, using gemini samples with a Gemini/DNA charge ratio of 12/1 without helper lipids, both at 25°C (Figure 47) and 40°C (Figure 48), and with helper lipids at 25°C (Figure 49).

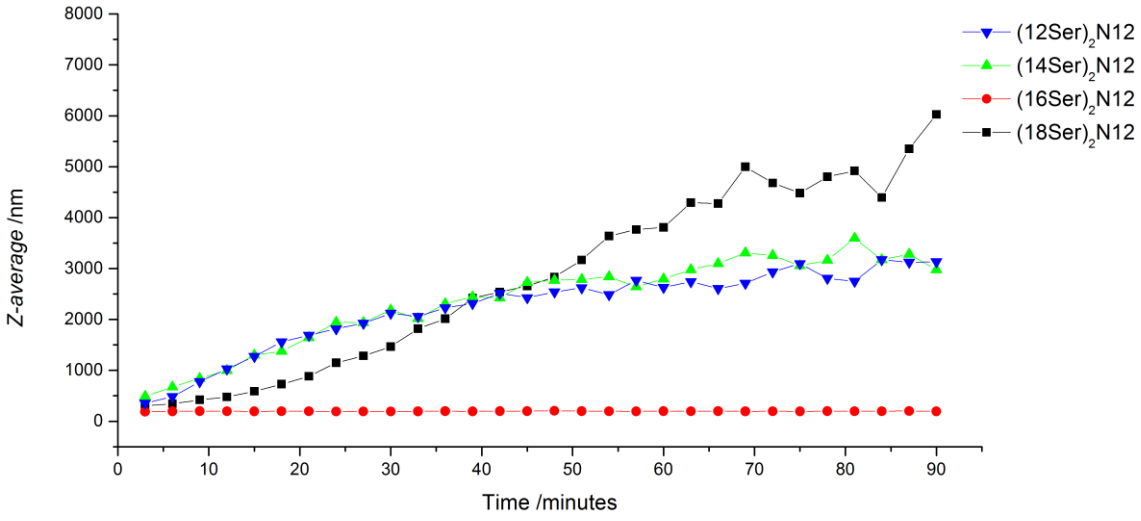

Figure 47 - Plot of the aggregate's size (Z-average) over time at 25°C, for the entire $(nSer)_2N12$ gemini series at the Gemini/DNA charge ratio of 12/1.

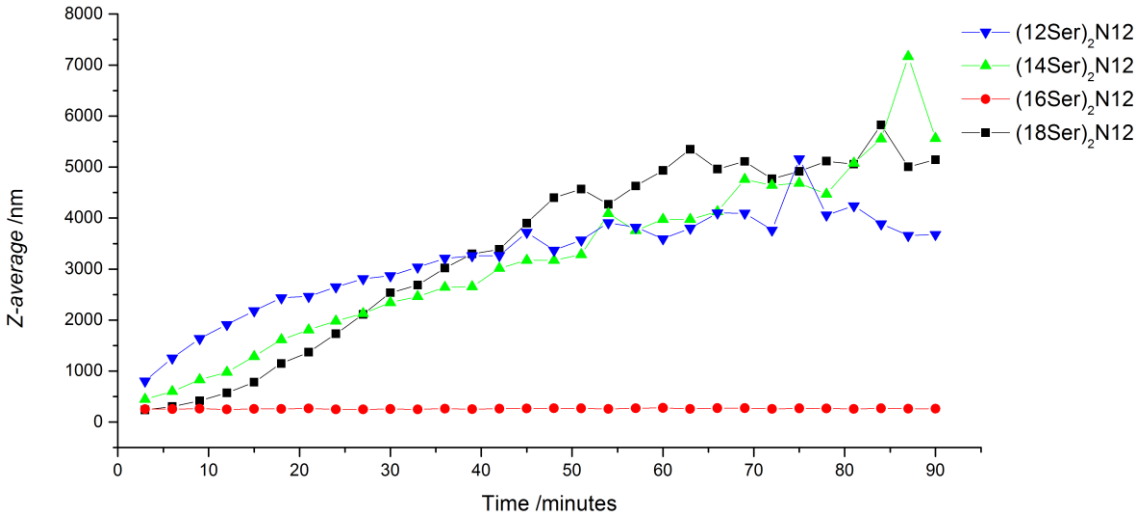

Figure 48 - Plot of the aggregate's size (Z-average) over time at 40°C, for the entire $(nSer)_2N12$ gemini series at the Gemini/DNA charge ratio of 12/1.

In the absence of helper lipids, $(16Ser)_2N12$ showed to be stable during the entire experiment, averaging a size of 194nm at 25°C and 261nm at 40°C. At 25°C, $(12Ser)_2N12$ and $(14Ser)_2N12$ increased in size over time but reached a plateau at about 50 minutes, after which the size did not vary significantly. For $(18Ser)_2N12$ the behaviour was different, since size did not stop increasing until the end of the experiment. At 40°C, no plateau was reached for any of the samples, with the exception of the stable $(16Ser)_2N12$.

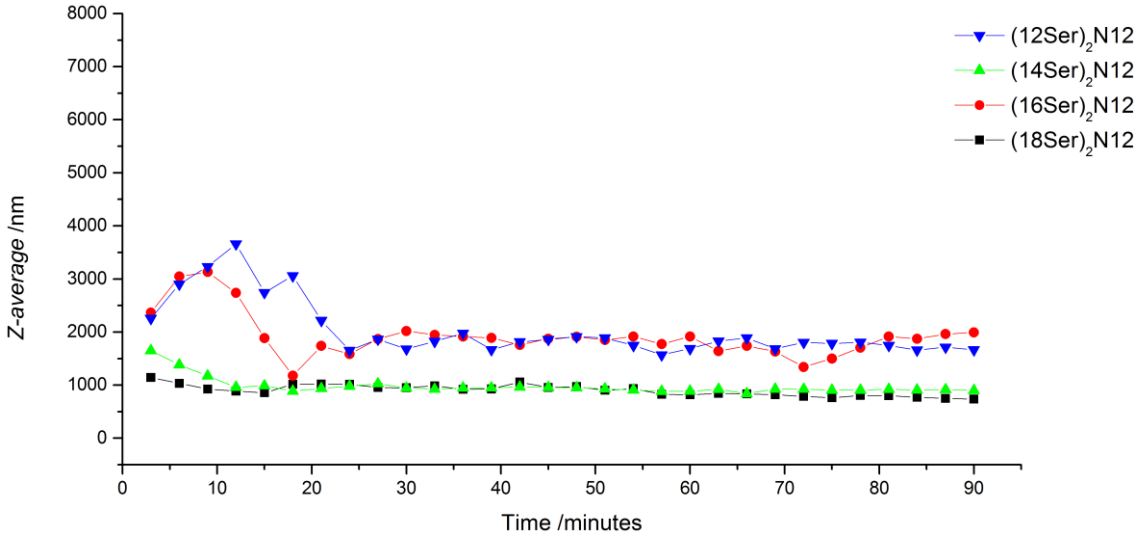

Figure 49 - Plot of the aggregate's size (Z-average) over time at 25°C with helper lipids present, for the entire $(nSer)_2N12$ gemini series at the Gemini/DNA charge ratio of 12/1.

In the presence of helper lipids at 25°C, the behaviour of the samples changes dramatically. During the first 20 minutes, the lipoplex size is unstable, with a sharp increase followed by a decrease for the $(12Ser)_2N12$ and $(16Ser)_2N12$. The other two systems, however, showed to be more stable, with only a slight decrease followed by an even smaller increase in size.

It is also noteworthy that the $(12Ser)_2N12$ and $(16Ser)_2N12$ ternary complexes show higher size fluctuations in the stable plateau than the other two. Curiously, the four ternary complexes seem to stabilize at two distinct sizes, hovering 1000 nm and 2000 nm, without a dependence on the hydrocarbon chains length.

3.4.2 Particle size and Zeta potential

All measurements were performed in accordance with the previously described method, with each sample being prepared immediately prior to the DLS and zeta potential analysis procedure.

Table 3 - Size measured by DLS and zeta potential of (nSer)2N12 gemini series, both with and without helper lipids.

Gemini	Gemini:DNA charge ratio	Without Helper Lipids 25°C		With Helper Lipids 25°C	
		Size *(nm)*	Zeta potential *(mV)*	Size *(nm)*	Zeta potential *(mV)*
$(12Ser)_2N12$	8/1	403 ± 49	30,5 ± 1,8	2753 ± 309	-35,1 ± 0,6
	10/1	536 ± 45	31,3 ± 1,2	1950 ± 107	-35,6 ± 1,1
	12/1	783 ± 72	30,9 ± 1,2	2959 ± 334	-43,1 ± 0,9
$(14Ser)_2N12$	8/1	1401 ± 310	24,4 ± 1,6	871 ± 66	-37,7 ± 1,4
	10/1	1317 ± 248	23,7 ± 2,1	1236 ± 125	-35,5 ± 1,6
	12/1	1394 ± 215	23,4 ± 1,5	1232 ± 195	-42,6 ± 1,3
$(16Ser)_2N12$	8/1	131 ± 1	32,5 ± 0,7	2857 ± 383	-33,6 ± 0,9
	10/1	137 ± 2	29,7 ± 0,6	2637 ± 360	-34,3 ± 2,7
	12/1	194 ± 1	33,4 ± 0,7	2633 ± 515	-47,6 ± 1,7
$(18Ser)_2N12$	8/1	1397 ± 365	22,3 ± 1,5	730 ± 71	-26,8 ± 0,5
	10/1	1380 ± 391	23 ± 1,4	1275 ± 149	-30,1 ± 0,7
	12/1	1216 ± 305	20,9 ± 1,9	969 ± 119	-39,8 ± 0,6

Starting by comparing the size of the complexes, it is noticeable that the ternary complexes (gemini/DNA/HL) containing $(12Ser)_2N12$ and $(16Ser)_2N12$ have a significantly larger size than their binary (gemini/DNA) counterparts. Among both the ternary and binary complexes, two charge ratio/size trends can be observed, both on the binary complexes of $(12Ser)_2N12$ and $(16Ser)_2N12$. Among all binary complexes, the most notorious for its size is the $(16Ser)_2N12$ binary complex since it is of a much smaller size at all charge ratios.

For binary complexes, we can observe that the zeta potential is always positive, while for ternary complexes the zeta potential values invert to a negative potential, with a higher modulus. (14Ser)*2*N12 and $(18Ser)_2N12$ binary complexes have a slightly smaller zeta potential than the rest of the gemini series, but the ternary complexes do not show that difference.

3.4.3 Morphology

Visual comparisons between the various gemini/DNA charge ratios were carried out, but no distinct differences were found. Therefore, all images shown below belong to complexes of gemini/DNA (binary) and gemini/DNA/HL (ternary) with a charge ratio of 12/1.

Overall, there does not seem to exist a correlation between the shape and size of the visible structures and the hydrocarbon chain length of the gemini. However, the ternary complexes seemed to aggregate less in dense structures, and formed instead more numerous but smaller clusters.

$(12Ser)_2N12$
gemini/DNA

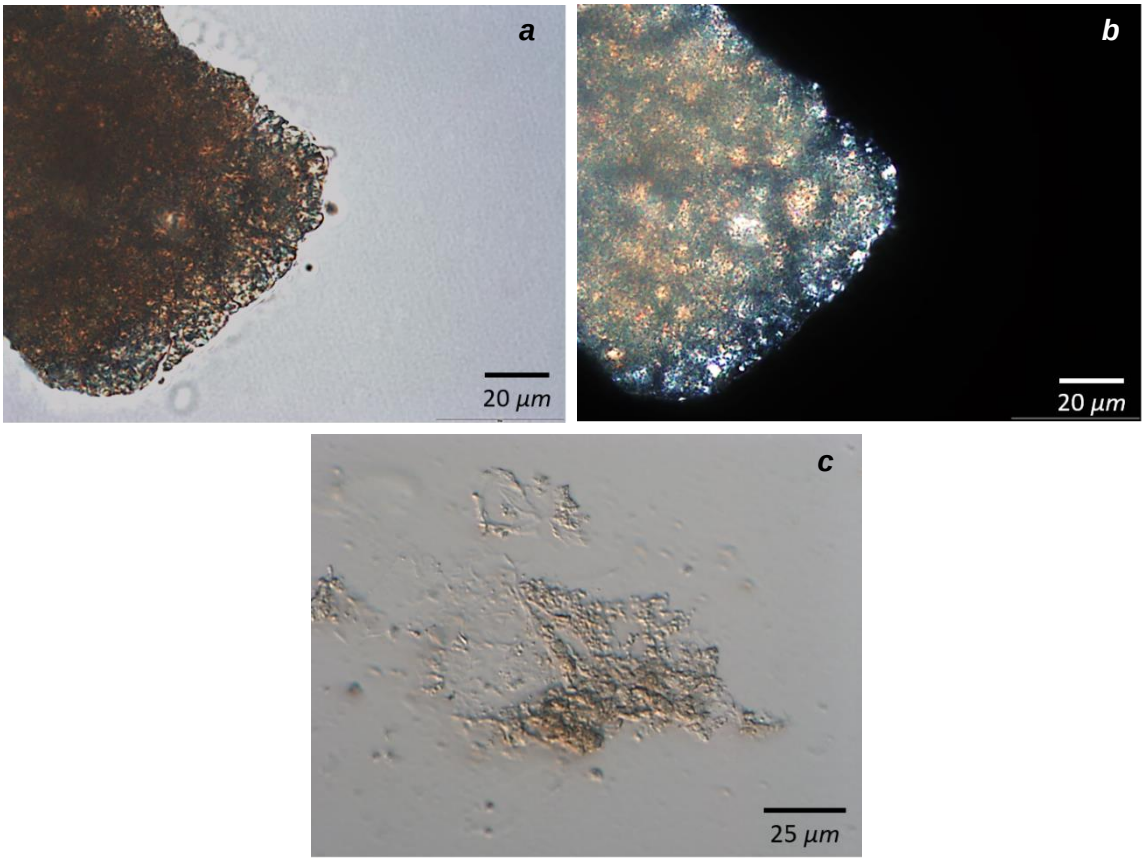

Figure 50 - $(12Ser)_2N12$ binary complexes images obtained under DIC (*a* and *c*) and polarized light (*b*).

gemini/DNA/HL

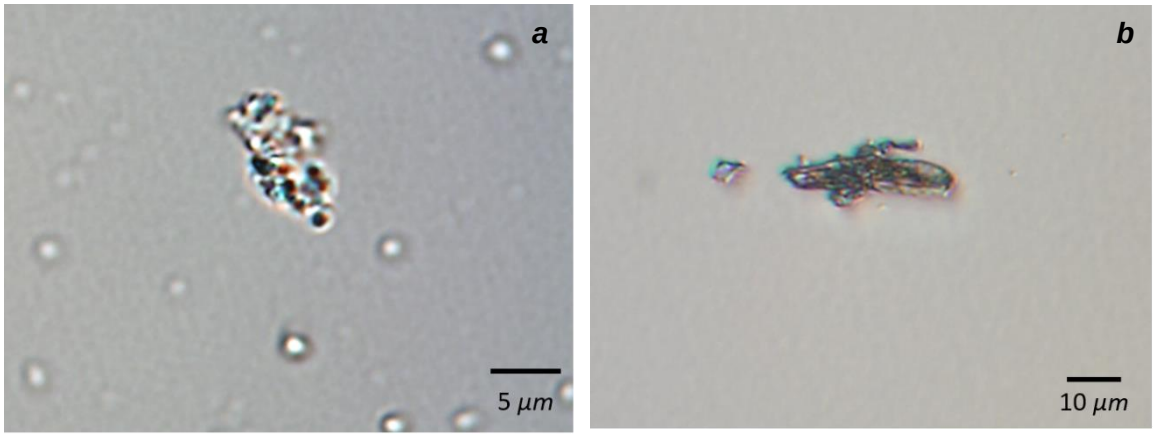

Figure 51 – $(12Ser)_2N12$ ternary complexes under DIC.

For the $(12Ser)_2N12$ binary complexes we could observe very large dense particles with some birefringence (Figure 50 **a** and **b**) and some less dense particles (Figure 50 **c**), seemingly formed by the same type of structures. These structures have a higher size than what was measured by DLS for the same complex. In the presence of helper lipids (ternary complexes), a bigger number of smaller aggregates is found, with size more similar to the values obtained by DLS (Figure 51). In both cases no neat organized structure such as bylayer structures could be identified.

$(14Ser)_2N12$

gemini/DNA

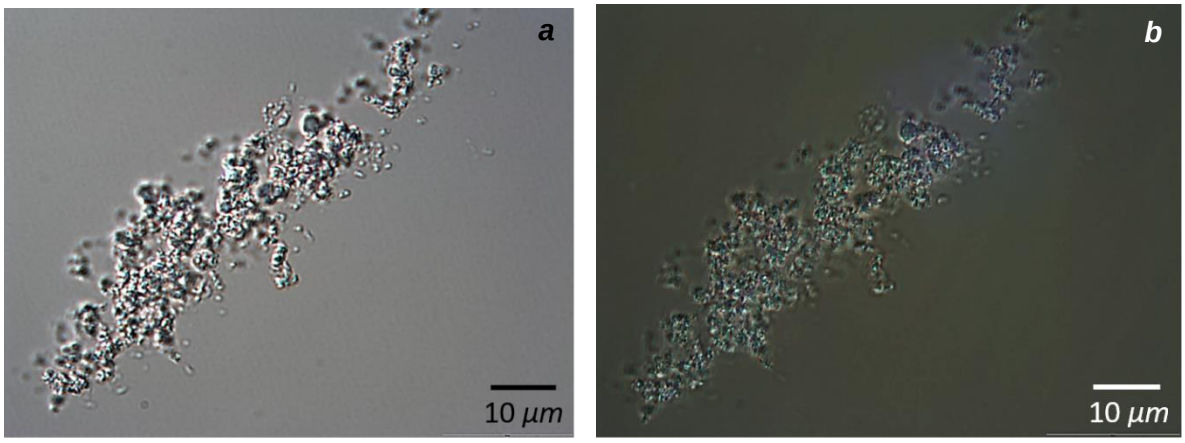

Figure 52 - $(14Ser)_2N12$ binary complexes under DIC (a) and polarized light (b).

gemini/DNA/HL

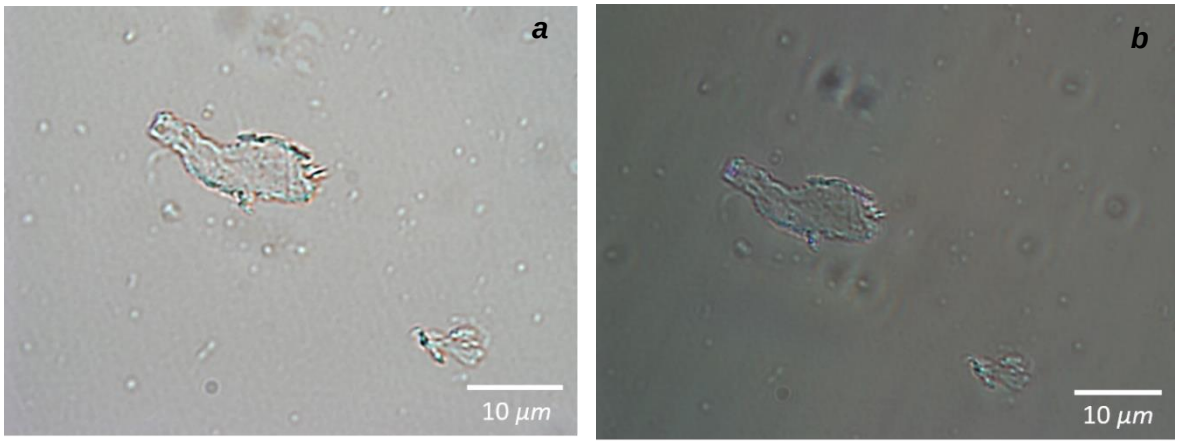

Figure 53 - $(14Ser)_2N12$ ternary complexes under DIC (a) and polarized light (b).

In the images for the $(14Ser)_2N12$ binary complexes, we can observe less dense clusters of the same granular texture as seen before in $(12Ser)_2N12$, with detectable birefringence. In ternary complexes, these granular textures disappeared, giving rise to smaller less packed structures, still maintaining a degree of birefringence (Figure 53). Like before, no neat organized structures could be identified.

$(16Ser)_2N12$

gemini/DNA

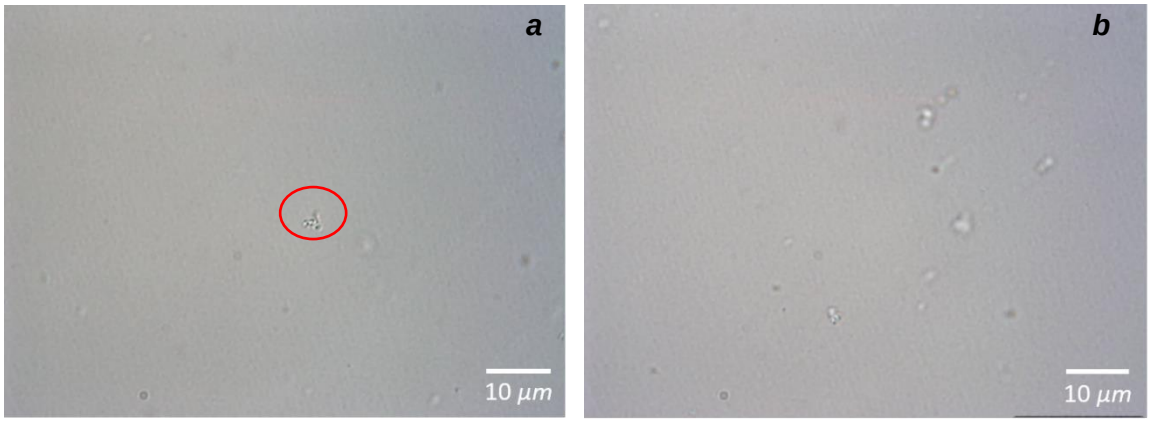

Figure 54 - $(16Ser)_2N12$ binary complexes under DIC. Aggregate circled in red (a).

gemini/DNA/HL

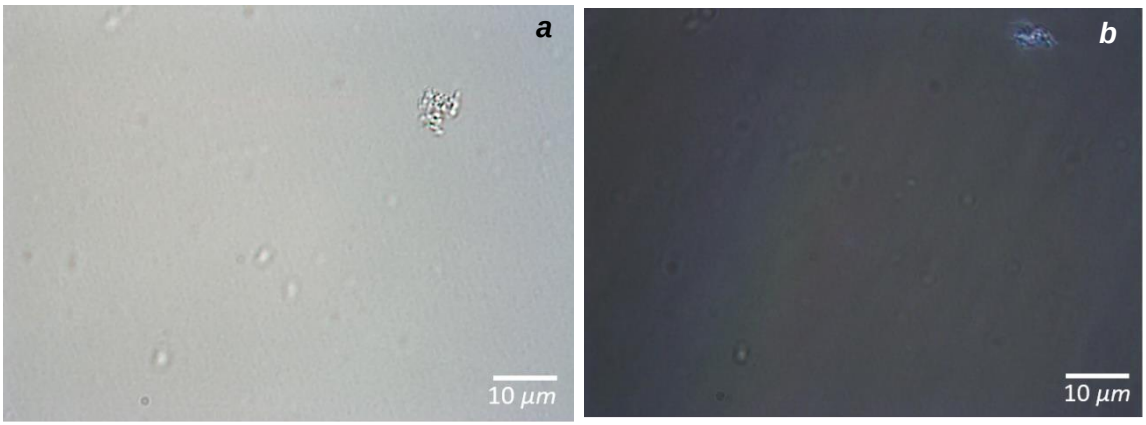

Figure 55 - $(16Ser)_2N12$ ternary complexes under DIC (a) and polarized light (b).

The binary complexes of $(16Ser)_2N12$ are different than the rest, with only one possible structure found in the entire slide preparation (Figure 54 **a**, circled in red). This is in accordance to DLS data obtained previously, since the particles measured have a sizer lower than the resolution limit of the microscope used. In the ternary complexes of this gemini only little more could be found, exhibiting birefringence (Figure 55).

$(18Ser)_2N12$

gemini/DNA

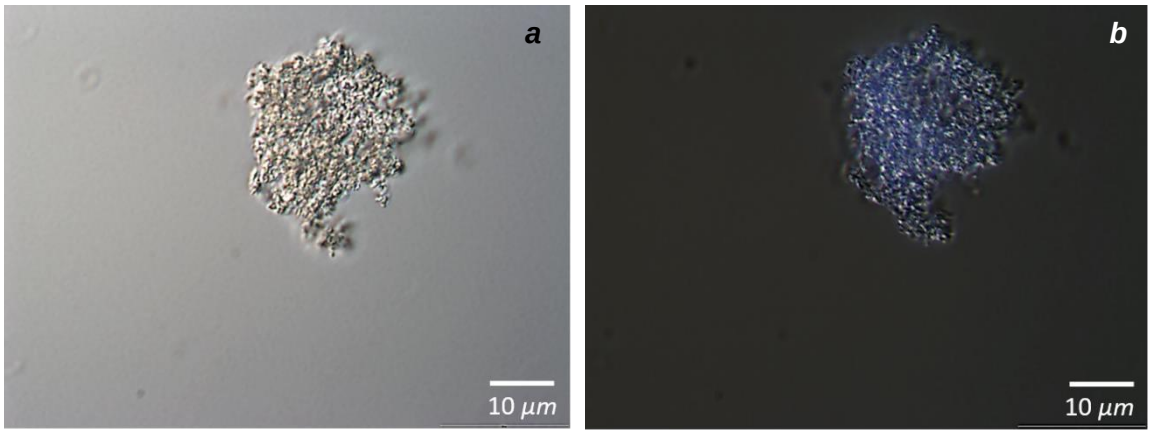

Figure 56 - $(18Ser)_2N12$ binary complexes under DIC (a) and polarized light (b).

gemini/DNA/HL

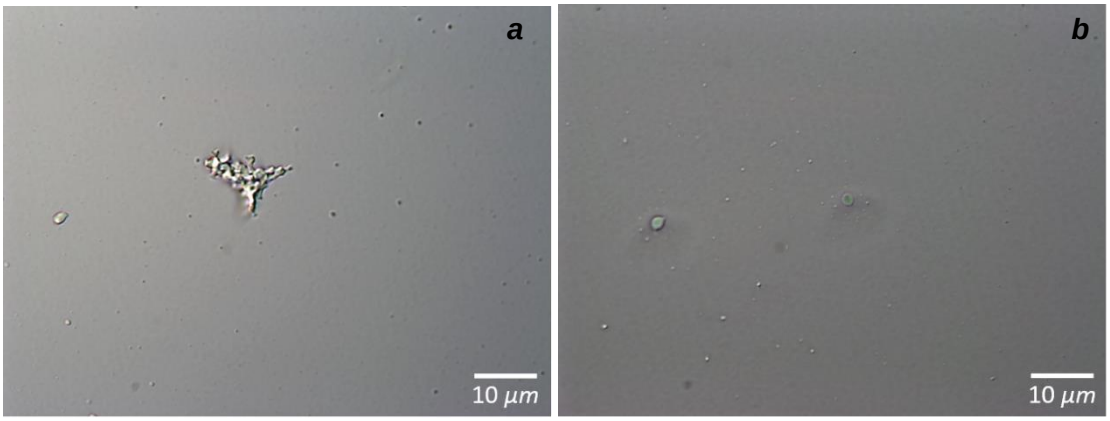

Figure 57 - $(18Ser)_2N12$ ternary complexes under DIC.

Lastly, the $(18Ser)_2N12$ binary complexes form large amorphous birefringent aggregates like the ones in $(12Ser)_2N12$ and $(14Ser)_2N12$ binary complexes (Figure 56). The ternary complexes of this gemini were difficult to detect, being of much smaller size (Figure 57 a). In the preparation slide, some evidences of phase separation were also found (Figure 57 b).

Helper Lipids

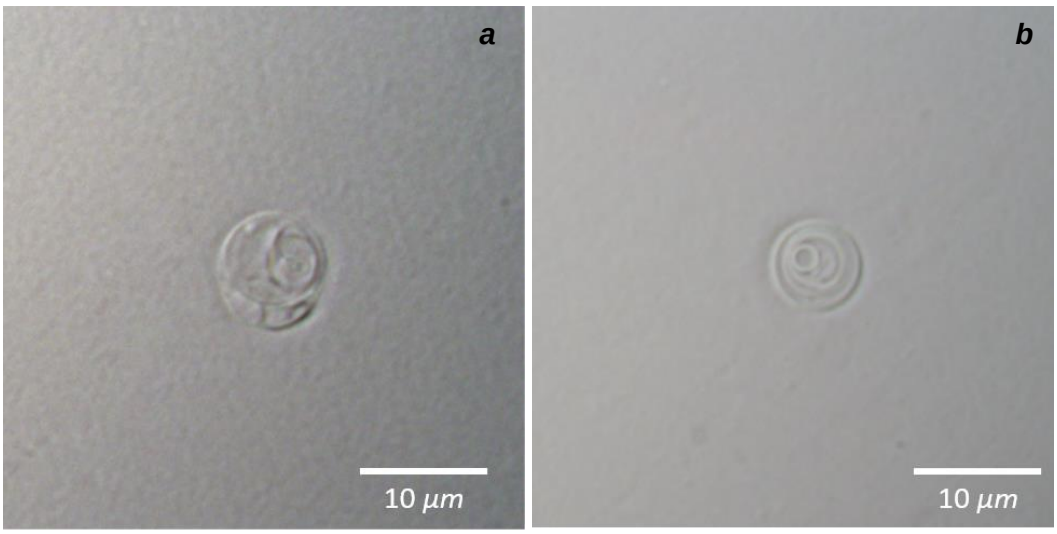

Figure 58 - DOPE:Chol helper lipid dispersion under DIC.

The helper lipid dispersion was also analysed under DIC microscopy, and multivesicular liposomes formed by them could be easily detected (Figure 58), as expected from this preparation.

3.4.4 Trends in lipoplex properties and comparison with previous studies

Previous studies on the $(nSer)_2N5$ series have also shown an inversion in zeta potential with the addition of DOPE:Chol helper lipid system, especially at high hydrocarbon chain lengths and increased gemini:DNA charge ratios[59].

This inversion did not happen in a similar study, in which the complex preparation was slightly different (for the $(12Ser)_2N12$ gemini)[72]. Within the same report, the $(12Ser)_2N12$ zeta potential agrees with the results in this work, at the measured charge ratios. However, there are some discrepancies with the DLS measured size of the aggregates with this gemini surfactants.

Similar to the *cmc* determination results, the stability of aggregates size over time, both with and without helper lipids, showed unusual and curious tendencies. Without HL, only $(16Ser)_2N12$ is stable over the entire timeframe studied, even though this complex has similar zeta potential values to the rest of the binary complexes (Table 3). Thus, this rapid growth of the other aggregates is most likely not due to the zeta potential parameter. Furthermore, the observed zeta potential values of the binary complexes should confer moderate stability in time, which is not observed. This difference between $(16Ser)_2N12$ and the rest is visible in the microscopy results, being nearly impossible to find a $(16Ser)_2N12$ aggregate (Figure 54) by the microscopy techniques used, due to resolution limits of the equipment.

It is interesting to note that the binary complexes that aggregate to a high size do not do so in a linear fashion for the entirety of the measurement. They tend to have a more haphazard aggregation from the 40-45 minutes onward, at both temperatures (Figure 47 and Figure 48).

With the presence of helper lipids (ternary complexes), the complexes' behaviour changes dramatically. Their size is only unstable at the beginning of the measurement, stabilizing at a certain size from the 20-25 minutes mark (Figure 49). The much lower size of the $(16Ser)_2N12$ binary complex is not noted here, with the behaviour of the ternary complex being much more similar to the rest.

The inversion in zeta potential with the addition of HL is not expected, but as referred before it may be a result of the complexes' preparation method. A possible explanation is that in the preformed gemini:DNA complexes both components are strongly bound, and cannot be rearranged as the HL lipid is added. Thus, the HL vesicles adsorb at the binary complexes surface, forming bigger structures with a negative zeta potential, coming from the contribution of DOPE.

The zeta potential of ternary complexes is also quite higher in modulus (Table 3) than those of binary complexes, granting them less tendency to aggregate. This is a visible effect in the microscopy pictures, as the ternary complexes form much smaller and fewer amorphous aggregates, the exception being $(16Ser)_2N12$.

3.5 Effects of lipoplex properties on biological activity

From the biological assays' data for the $(nSer)_2N12$ gemini surfactant series a trend arises for the complexes without helper lipids (binary). The higher the cellular viability, the lower the transfection efficiency. While the two parameters seem to be correlated, it is not possible to say with certainty that high viability is due to low transfection efficiencies.

When comparing the results from biological assays to the results from lipoplex characterization, no correlation between complex size and transfection efficiency/cellular viability is evident. However, there is some correlation between transfection efficiency and zeta potential – the binary complexes with highest transfection efficiencies are those containing the $(12Ser)_2N12$ and $(16Ser)_2N12$, which have a zeta potential rounding +31 mV for both complexes at all charge ratios, while those with lower transfection (among binary complexes), containing $(14Ser)_2N12$ and $(18Ser)_2N12$ have a zeta potential rounding +23 mV.

Ternary complexes have a high modulus negative zeta potential. Cellular membranes have a negative surface potential by themselves, thus, the more negative zeta potential a complex has, the more difficult it is for it to interact with the negatively charged cellular membrane (and consequently the mitochondria), due to electrostatic repulsions. Furthermore, the effect of the highly negative zeta potential in ternary complexes is also evident in microscopy results, as the macro-aggregates observed are smaller than their binary complexes counterparts.

Although it is not observed in the biological experiments data, it was expected, considering results obtained from DLS, for binary complexes of $(16Ser)_2N12$ to have better transfection efficiency due to their smaller size, which is ideal for cellular internalization via endocytosis.

Taking into account the above considerations, a probable hypothesis is that transfection with $(12Ser)_2N12$, $(14Ser)_2N12$ and $(18Ser)_2N12$ complexes occurs via fusion of these complexes with the cellular membranes, which could also explain the

relatively high cytotoxicity observed and the reasonable transfection even with very high complex sizes (such as were determined by DLS). Thus, gemini surfactants alone in the membrane would cause a disruptive effect on the membrane, untempered by the presence of helper lipids. The stable small size of $(16Ser)_2N12$ binary complexes would suggest its internalization via normal endocytic pathways.

Further studies with internalization pathway inhibitors are required to determine the method of DNA internalization into cells with the complexes studied in this project.

Chapter 4: Conclusions and future prospects

The physicochemical and biological studies carried out in this work are of great relevance for the development of ever more efficient gemini surfactant-based gene delivery systems, which rely greatly on the molecular properties of the DNA-complexing molecules.

It was found that the $(nSer)_2N12$ gemini compounds possess a much lower critical micelle concentration than similar compounds with shorter alky spacers and the conventional bis-quat 12-12-12 gemini surfactants. The change in *cmc* with the length of the hydrocarbon chains presents an unusual and interesting trend, which warrants further study of serine-derived gemini, with hydrocarbon chains longer than 18 carbons.

The prepared binary (gemini/DNA) and ternary (gemini/DNA/helper lipids) complexes show distinct biological properties, with binary complexes having moderate transfection and relatively high cytotoxicity, while ternary complexes having little to no transfection ability, but barely showing cytotoxicity. These biological activities seem to be correlated both with the length of the hydrocarbon chain in a non-linear fashion and the gemini:DNA (+/-) charge ratio of the complexes, with transfection and cytotoxicity increasing with the increase in charge ratio. The higher cytotoxicity seems to be correlated with the increase in transfection, but further studies are required to prove the causal link. The values obtained in biological studies, especially the difference between binary and ternary complexes can in part be explained by the size and zeta potential values measured.

As concerning future perspectives, further studies of internalization pathways and complex-membrane interactions (such as Fluorescence Resonance Energy Transfer (FRET) studies) will be required to further insight on the interactions of these gemini and their DNA complexes with living cells.

Bibliography

1. http://www.umich.edu/~chemh215/W11HTML/SSG2/ssg2.1/glossary1.html, 15/09/2016
2. Wang, Y. J.; Marques, E. F. Non-ideal behavior of mixed micelles of cationic gemini surfactants with varying spacer length and anionic surfactants: A conductimetric study. *J. Mol. Liq.* **2008,** *142*, 136-142.
3. Lin, M. T.; Beal, M. F. Mitochondrial dysfunction and oxidative stress in neurodegenerative diseases. *Nature* **2006,** *443*, 787-795.
4. Mitochondrial DNA, https://upload.wikimedia.org/wikipedia/commons/3/3e/Mitochondrial_DNA_en.svg, 10/09/2016
5. Adhya, S.; Mahato, B.; Jash, S.; Koley, S.; Dhar, G.; Chowdhury, T. Mitochondrial gene therapy: The tortuous path from bench to bedside. *Mitochondrion* **2011,** *11*, 839-844.
6. Wallace, D. C. The mitochondrial genome in human adaptive radiation and disease: on the road to therapeutics and performance enhancement. *Gene* **2005,** *354*, 169-180.
7. Wallace, D. C. A mitochondrial paradigm of metabolic and degenerative diseases, aging, and cancer: A dawn for evolutionary medicine. *Annu. Rev. Genet.* **2005,** *39*, 359-407.
8. Balaban, R. S.; Nemoto, S.; Finkel, T. Mitochondria, oxidants, and aging. *Cell* **2005,** *120* (4), 483-495.
9. Wallace, D. C. Mitochondrial diseases in man and mouse. *Science* **1999,** *283*, 1482-1488.
10. Moraes, C. T.; DiMauro, S.; Zeviani, M.; Lombes, A.; Shanske, S.; Miranda, A. F.; Nakase, H.; Bonilla, E.; Werneck, L. C.; Servidei, S.; Nonaka, I.; Koga, Y.; Spiro, A. J.; Brownell, K. W.; Schmidt, B.; Schotland, D. L.; Zupanc, M.; DeVivo, D. C.; Schon, E. A.; Rowland, L. P. Mitochondrial DNA deletions in progressive external ophthalmoplegia and Kearns-Sayre syndrome. *N. Engl. J. Med.* **1989,** *320*, 1293-1299.
11. Zeviani, M.; Moraes, C. T.; DiMauro, S.; Nakase, H.; Bonilla, E.; Schon, E. A.; Rowland, L. P. Deletions of mitochondrial DNA in Kearns-Sayre syndrome. *Neurology* **1988,** *38*, 1339-1346.
12. Jacobs, H. T. Disorders of mitochondrial protein synthesis. *Hum. Mol. Gen.* **2003,** *12*, 293-301.
13. Exner, N.; Lutz, A. K.; Haass, C.; Winklhofer, K. F. Mitochondrial dysfunction in Parkinson's disease: molecular mechanisms and pathophysiological consequences. *EMBO J.* **2012,** *31*, 3038-3062.
14. Valente, E. M.; Abou-Sleiman, P. M.; Caputo, V.; Muqit, M. M.; Harvey, K.; Gispert, S.; Ali, Z.; Del Turco, D.; Bentivoglio, A. R.; Healy, D. G.; Albanese, A.; Nussbaum, R.; Gonzalez-Maldonado, R.; Deller, T.; Salvi, S.; Cortelli, P.; Gilks, W. P.; Latchman, D. S.; Harvey, R. J.; Dallapiccola, B.; Auburger, G.; Wood, N. W. Hereditary early-onset Parkinson's disease caused by mutations in PINK1. *Science* **2004,** *304*, 1158-1160.
15. Petersen, K. F.; Dufour, S.; Befroy, D.; Garcia, R.; Shulman, G. I. Impaired mitochondrial activity in the insulin-resistant offspring of patients with type 2 diabetes. *N. Engl. J. Med.* **2004,** *350*, 664-671.
16. Lustbader, J. W.; Cirilli, M.; Lin, C.; Xu, H. W.; Takuma, K.; Wang, N.; Caspersen, C.; Chen, X.; Pollak, S.; Chaney, M.; Trinchese, F.; Liu, S.; Gunn-Moore, F.; Lue, L. F.; Walker, D. G.; Kuppusamy, P.; Zewier, Z. L.; Arancio, O.; Stern, D.; Yan, S. S.; Wu, H. ABAD directly links Abeta to mitochondrial toxicity in Alzheimer's disease. *Science* **2004,** *304*, 448-452.
17. Manczak, M.; Anekonda, T. S.; Henson, E.; Park, B. S.; Quinn, J.; Reddy, P. H. Mitochondria are a direct site of A beta accumulation in Alzheimer's disease neurons:

implications for free radical generation and oxidative damage in disease progression. *Hum. Mol. Genet.* **2006,** *15*, 1437-1449.
18. Hiona, A.; Leeuwenburgh, C. The role of mitochondrial DNA mutations in aging and sarcopenia: implications for the mitochondrial vicious cycle theory of aging. *Exp. Gerontol.* **2008,** *43*, 24-33.
19. Craven, L.; Tuppen, H. A.; Greggains, G. D.; Harbottle, S. J.; Murphy, J. L.; Cree, L. M.; Murdoch, A. P.; Chinnery, P. F.; Taylor, R. W.; Lightowlers, R. N.; Herbert, M.; Turnbull, D. M. Pronuclear transfer in human embryos to prevent transmission of mitochondrial DNA disease. *Nature* **2010,** *465*, 82-85.
20. Craven, L.; Herbert, M.; Murdoch, A.; Murphy, J.; Lawford Davies, J.; Turnbull, D. M. Research into Policy: A Brief History of Mitochondrial Donation. *Stem Cells* **2016,** *34*, 265-267.
21. Dolinsky, V. W.; Cole, L. K.; Sparagna, G. C.; Hatch, G. M. Cardiac mitochondrial energy metabolism in heart failure: Role of cardiolipin and sirtuins. *Biochim. Biophys. Acta* **2016,** *1860*, 1544-1554.
22. Yamada, Y.; Akita, H.; Kogure, K.; Kamiya, H.; Harashima, H. Mitochondrial drug delivery and mitochondrial disease therapy--an approach to liposome-based delivery targeted to mitochondria. *Mitochondrion* **2007,** *7*, 63-71.
23. Cardoso, A. M.; Morais, C. M.; Cruz, A. R.; Cardoso, A. L.; Silva, S. G.; do Vale, M. L.; Marques, E. F.; de Lima, M. C. P.; Jurado, A. S. Gemini Surfactants Mediate Efficient Mitochondrial Gene Delivery and Expression. *Mol. Pharm.* **2015,** *12*, 716-730.
24. Chinnery, P. F.; Thorburn, D. R.; Samuels, D. C.; White, S. L.; Dahl, H.-H. M.; Turnbull, D. M.; Lightowlers, R. N.; Howell, N. The inheritance of mitochondrial DNA heteroplasmy: random drift, selection or both? *Trends Genet.* **2000,** *16*, 500-505.
25. Stewart, J. B.; Chinnery, P. F. The dynamics of mitochondrial DNA heteroplasmy: implications for human health and disease. *Nat. Rev. Genet.* **2015,** *16*, 530-542.
26. Cao, Z.; Wanagat, J.; McKiernan, S. H.; Aiken, J. M. Mitochondrial DNA deletion mutations are concomitant with ragged red regions of individual, aged muscle fibers: analysis by laser-capture microdissection. *Nucleic Acids Res.* **2001,** *29*, 4502-4508.
27. Cardoso, A. M. S.; Silva, S. G.; Luísa do Vale, M.; Marques, E. F.; Pedroso de Lima, M. C.; Jurado, A. S. Gene delivery mediated by gemini surfactants. In *Engineering of Nanobiomaterials: Applications of Nanobiomaterials*, Grumezescu, A. M., Ed.; Elsivier: Oxford, 2016; Vol. 2, pp 227-256.
28. Hoekstra, D.; Rejman, J.; Wasungu, L.; Shi, F.; Zuhorn, I. Gene delivery by cationic lipids: in and out of an endosome. *Biochem. Soc. Trans.* **2007,** *35*, 68-71.
29. Luo, D.; Saltzman, W. M. Synthetic DNA delivery systems. *Nat. Biotechnol.* **2000,** *18*, 33-37.
30. Li, J.; Fan, C. H.; Pei, H.; Shi, J. Y.; Huang, Q. Smart Drug Delivery Nanocarriers with Self-Assembled DNA Nanostructures. *Adv. Mater.* **2013,** *25*, 4386-4396.
31. McNamara, K.; Tofail, S. A. M. Nanosystems: the use of nanoalloys, metallic, bimetallic, and magnetic nanoparticles in biomedical applications. *Phys. Chem. Chem. Phys.* **2015,** *17*, 27981-27995.
32. Ray, P. C. Diagnostics of single base-mismatch DNA hybridization on gold nanoparticles by using the hyper-Rayleigh scattering technique. *Angew. Chem. Int. Ed.* **2006,** *45*, 1151-1154.
33. Mitra, R. N.; Nichols, C. A.; Guo, J.; Makkia, R.; Cooper, M. J.; Naash, M. I.; Han, Z. Nanoparticle-mediated miR200-b delivery for the treatment of diabetic retinopathy. *J. Control. Release* **2016,** *236*, 31-37.
34. Nayerossadat, N.; Maedeh, T.; Ali, P. A. Viral and nonviral delivery systems for gene delivery. *Adv. Biomed. Res.* **2012,** *1*, 27-38.
35. Lentz, T. B.; Gray, S. J.; Samulski, R. J. Viral vectors for gene delivery to the central nervous system. *Neurobiol. Dis.* **2012,** *48*, 179-188.
36. Dalby, B.; Cates, S.; Harris, A.; Ohki, E. C.; Tilkins, M. L.; Price, P. J.; Ciccarone, V. C. Advanced transfection with Lipofectamine 2000 reagent: primary neurons, siRNA, and high-throughput applications. *Methods* **2004,** *33*, 95-103.

37. Oliveira, I. M.; Silva, J. P.; Feitosa, E.; Marques, E. F.; Castanheira, E. M.; Real Oliveira, M. E. Aggregation behavior of aqueous dioctadecyldimethylammonium bromide/monoolein mixtures: a multitechnique investigation on the influence of composition and temperature. *J. Colloid Interface. Sci.* **2012,** *374*, 206-217.
38. Farhood, H.; Serbina, N.; Huang, L. The role of dioleoyl phosphatidylethanolamine in cationic liposome mediated gene transfer. *Biochim. Biophys. Acta* **1995,** *1235*, 289-295.
39. Hui, S. W.; Langner, M.; Zhao, Y. L.; Ross, P.; Hurley, E.; Chan, K. The role of helper lipids in cationic liposome-mediated gene transfer. *Biophys. J.* **1996,** *71*, 590-599.
40. Holmberg, K.; Shah, D. O.; Schwuger, M. J. *Handbook of applied surface and colloid chemistry*; Wiley2002.
41. Tadros, T. F. Adsorption of Surfactants at the Air/Liquid and Liquid/Liquid Interfaces. In *Applied Surfactants*; Wiley, 2005, pp 73-84.
42. Simons, K.; Toomre, D. Lipid rafts and signal transduction. *Nat. Rev. Mol. Cell Biol.* **2000,** *1*, 31-39.
43. Goerke, J. Lung surfactant. *Biochim. Biophys. Acta* **1974,** *344*, 241-261.
44. Rooney, S. A.; Young, S. L.; Mendelson, C. R. Molecular and cellular processing of lung surfactant. *FASEB J.* **1994,** *8*, 957-967.
45. Shaw, D. J. 4 - Liquid–gas and liquid–liquid interfaces. In *Introduction to Colloid and Surface Chemistry (Fourth Edition)*, Shaw, D. J., Ed.; Butterworth-Heinemann: Oxford, 1992, pp 64-114.
46. http://www.ctgclean.com/tech-blog/2013/06/what-is-surface-tension/, 16/09/2015
47. Marques, E.; Silva, B. B. Surfactant Self-Assembly. In *Encyclopedia of Colloid and Interface Science*, Tadros, T., Ed.; Springer Berlin Heidelberg:Dordrecht, London: New York, 2013, pp 1202-1241.
48. http://cancurecancer.org/wp-content/uploads/2015/09/liposome.png, 10/09/2016
49. Marques, E. F.; Silva, B. F. B. Surfactant Self-Assembly. In *Encyclopedia of Colloid and Interface Science*, Tadros, T., Ed.; Springer Berlin Heidelberg, 2013, pp 1202-1241.
50. Wang, M.; Han, Y.; Qiao, F.; Wang, Y. Aggregation behavior of a gemini surfactant with a tripeptide spacer. *Soft Matter* **2015,** *11*, 1517-1524.
51. Bajaj, A.; Kondaiah, P.; Bhattacharya, S. Gene transfection efficacies of novel cationic gemini lipids possessing aromatic backbone and oxyethylene spacers. *Biomacromolecules* **2008,** *9*, 991-999.
52. Kumar, V.; Chatterjee, A.; Kumar, N.; Ganguly, A.; Chakraborty, I.; Banerjee, M. D-Glucose derived novel gemini surfactants: synthesis and study of their surface properties, interaction with DNA, and cytotoxicity. *Carbohydr. Res.* **2014,** *397*, 37-45.
53. Rosen, M. J.; Tracy, D. J. Gemini surfactants. *J. Surfactants Deterg.* **1998,** *1*, 547-554.
54. Perez, L.; Torres, J. L.; Manresa, A.; Solans, C.; Infante, M. R. Synthesis, aggregation, and biological properties of a new class of gemini cationic amphiphilic compounds from arginine, bis(Args). *Langmuir* **1996,** *12*, 5296-5301.
55. Zana, R. Dimeric and oligomeric surfactants. Behavior at interfaces and in aqueous solution: a review. *Adv. Colloid Interface Sci.* **2002,** *97*, 205-253.
56. Murguía, M. C.; Vaillard, V. A.; Sánchez, V. G.; Conza, J. D.; Grau, R. J. Synthesis, Surface-Active Properties, and Antimicrobial Activities of New Double-Chain Gemini Surfactants. *J. Oleo Sci.* **2008,** *57*, 301-308.
57. Tan, H.; Xiao, H. N. Synthesis and antimicrobial characterization of novel L-lysine gemini surfactants pended with reactive groups. *Tetrahedron Lett.* **2008,** *49*, 1759-1761.
58. Caillier, L.; de Givenchy, E. T.; Levy, R.; Vandenberghe, Y.; Geribaldi, S.; Guittard, F. Polymerizable semi-fluorinated gemini surfactants designed for antimicrobial materials. *J. Colloid Interface Sci.* **2009,** *332*, 201-207.

59. Cardoso, A. M.; Morais, C. M.; Cruz, A. R.; Silva, S. G.; do Vale, M. L.; Marques, E. F.; de Lima, M. C.; Jurado, A. S. New serine-derived gemini surfactants as gene delivery systems. *Eur. J. Pharm. Biopharm.* **2015,** *89*, 347-356.
60. Cardoso, A. M.; Morais, C. M.; Cruz, A. R.; Cardoso, A. L.; Silva, S. G.; do Vale, M. L.; Marques, E. F.; Pedroso de Lima, M. C.; Jurado, A. S. Gemini surfactants mediate efficient mitochondrial gene delivery and expression. *Mol. Pharm.* **2015,** *12*, 716-730.
61. Goreti Silva, S.; Fernandes, R. F.; Marques, E. F.; do Vale, M. L. C. Serine-Based Bis-quat Gemini Surfactants: Synthesis and Micellization Properties. *Eur. J. Org. Chem.* **2012,** *2012*, 345-352.
62. Damen, M.; Cristobal-Lecina, E.; Sanmarti, G. C.; van Dongen, S. F. M.; Rodriguez, C. L. G.; Dolbnya, I. P.; Nolte, R. J. M.; Feiters, M. C. Structure-delivery relationships of lysine-based gemini surfactants and their lipoplexes. *Soft Matter* **2014,** *10*, 5702-5714.
63. Perez, L.; Pinazo, A.; Pons, R.; Rosa Infante, M. Gemini surfactants from natural amino acids. *Adv. Colloid Interface Sci.* **2014,** *205*, 134-155.
64. Grueso, E.; Kuliszewska, E.; Roldan, E.; Perez-Tejeda, P.; Prado-Gotor, R.; Brecker, L. DNA conformational changes induced by cationic gemini surfactants: the key to switching DNA compact structures into elongated forms. *RSC Adv.* **2015,** *5*, 29433-29446.
65. Zhang, Y.-M.; Liu, Y.-H.; Zhang, J.; Liu, Q.; Huang, Z.; Yu, X.-Q. Cationic gemini lipids with cyclen headgroups: interaction with DNA and gene delivery abilities. *RSC Adv.* **2014,** *4*, 44261-44268.
66. Marchetti, S.; Onori, G.; Cametti, C. DNA condensation induced by cationic surfactant: a viscosimetry and dynamic light scattering study. *J. Phys. Chem. B* **2005,** *109*, 3676-3680.
67. Wang, C.; Li, X.; Wettig, S. D.; Badea, I.; Foldvari, M.; Verrall, R. E. Investigation of complexes formed by interaction of cationic gemini surfactants with deoxyribonucleic acid. *Phys. Chem. Chem. Phys.* **2007,** *9*, 1616-1628.
68. Marquez-Miranda, V.; Araya-Duran, I.; Camarada, M. B.; Comer, J.; Valencia-Gallegos, J. A.; Gonzalez-Nilo, F. D. Self-Assembly of Amphiphilic Dendrimers: The Role of Generation and Alkyl Chain Length in siRNA Interaction. *Sci. Rep.* **2016,** *6*, 29436-29451.
69. Kirby, A. J.; Camilleri, P.; Engberts, J. B.; Feiters, M. C.; Nolte, R. J.; Soderman, O.; Bergsma, M.; Bell, P. C.; Fielden, M. L.; Garcia Rodriguez, C. L.; Guedat, P.; Kremer, A.; McGregor, C.; Perrin, C.; Ronsin, G.; van Eijk, M. C. Gemini surfactants: new synthetic vectors for gene transfection. *Angew. Chem. Int. Ed.* **2003,** *42*, 1448-1457.
70. Karlsson, L.; van Eijk, M. C.; Soderman, O. Compaction of DNA by gemini surfactants: effects of surfactant architecture. *J. Colloid Interface Sci.* **2002,** *252*, 290-296.
71. Silva, S. G.; Alves, C.; Cardoso, A. M. S.; Jurado, A. S.; de Lima, M. C. P.; Vale, M. L. C.; Marques, E. F. Synthesis of Gemini Surfactants and Evaluation of Their Interfacial and Cytotoxic Properties: Exploring the Multifunctionality of Serine as Headgroup. *Eur. J. Org. Chem.* **2013,** *2013*, 1758-1769.
72. Silva, S. G.; Oliveira, I. S.; do Vale, M. L. C.; Marques, E. F. Serine-based gemini surfactants with different spacer linkages: from self-assembly to DNA compaction. *Soft Matter* **2014,** *10*, 9352-9361.
73. Silva, S. G.; Vale, M. L. C. d.; Marques, E. F. Size, Charge, and Stability of Fully Serine-Based Catanionic Vesicles: Towards Versatile Biocompatible Nanocarriers. *Chem. Eur. J.* **2015,** *21*, 4092-4101.
74. Almeida, J. A. S.; Faneca, H.; Carvalho, R. A.; Marques, E. F.; Pais, A. Dicationic Alkylammonium Bromide Gemini Surfactants. Membrane Perturbation and Skin Irritation. *PLoS ONE* **2011,** *6*.
75. Cardoso, A. M.; Morais, C. M.; Silva, S. G.; Marques, E. F.; de Lima, M. C. P.; Jurado, M. A. S. Bis-quaternary gemini surfactants as components of nonviral gene

delivery systems: A comprehensive study from physicochemical properties to membrane interactions. *Int. J. Pharm.* **2014,** *474*, 57-69.
76. Ley, S. V.; Norman, J.; Griffith, W. P.; Marsden, S. P. Tetrapropylammonium Perruthenate, Pr4N+RuO4-, TPAP: A Catalytic Oxidant for Organic Synthesis. *Synthesis* **1994,** *1994*, 639-666.
77. Kemp, W. *NMR in chemistry: a multinuclear introduction*; MACMILLAN EDUCATION LTD1986.
78. Pencer, J.; Hallett, F. R. Effects of Vesicle Size and Shape on Static and Dynamic Light Scattering Measurements. *Langmuir* **2003,** *19*, 7488-7497.
79. Aragón, S. R. Theory of dynamic light scattering from polydisperse systems. *J. Chem. Phys.* **1976,** *64*, 2395-2404.
80. Domingues, M. M.; Santiago, P. S.; Castanho, M. A.; Santos, N. C. What can light scattering spectroscopy do for membrane-active peptide studies? *J. Pept. Sci.* **2008,** *14*, 394-400.
81. Malvern Instruments Ltd; Zetasizer Nano Series User Manual, U., 2003.
82. Wiersema, P. H.; Loeb, A. L.; Overbeek, J. T. Calculation of Electrophoretic Mobility of a Spherical Colloid Particle. *J. Colloid Interface Sci.* **1966,** *22*, 78-99.
83. Kirby, B. J.; Hasselbrink, E. F., Jr. Zeta potential of microfluidic substrates: 1. Theory, experimental techniques, and effects on separations. *Electrophoresis* **2004,** *25*, 187-202.
84. Freire, J. M.; Domingues, M. M.; Matos, J.; Melo, M. N.; Veiga, A. S.; Santos, N. C.; Castanho, M. A. Using zeta-potential measurements to quantify peptide partition to lipid membranes. *Eur. Biophys. J.* **2011,** *40*, 481-487.
85. Inoué, S.; Oldenbourg, R. Microtubule Dynamics in Mitotic Spindle Displayed by Polarized Light Microscopy. *Mol. Biol. Cell* **1998,** *9*, 1603-1607.
86. Simoes, S.; Slepushkin, V.; Pires, P.; Gaspar, R.; de Lima, M. P.; Duzgunes, N. Mechanisms of gene transfer mediated by lipoplexes associated with targeting ligands or pH-sensitive peptides. *Gene Ther.* **1999,** *6*, 1798-1807.
87. Khan, I. A.; Mohammad, R.; Alam, M. S.; Kabir ud, D. Surface Properties and Mixed Micellization of Cationic Gemini Surfactants with Ethyleneamines. *J. Chem. Eng. Data* **2010,** *55*, 370-380.
88. Kabir ud, D.; Koya, P. A.; Khan, Z. A. Conductometric studies of micellization of gemini surfactant pentamethylene-1,5-bis(tetradecyldimethylammonium bromide) in water and water-organic solvent mixed media. *J. Colloid Interface. Sci.* **2010,** *342*, 340-347.
89. al, E. F. M. e. Unpublished results.
90. Eduardo, F. M. Surfactant Vesicles: Formation, Properties, and Stability. In *Encyclopedia of Surface and Colloid Science, Second Edition*; Taylor & Francis, 2007; Vol. null, pp 1-20.
91. Menger, F. M.; Littau, C. A. Gemini Surfactants - a New Class of Self-Assembling Molecules. *J Am Chem Soc* **1993,** *115*, 10083-10090.

Supplementary information

Dimethyl (2*S*,17*S*)-*Bis*(*tert*-butyloxymethyl)-3,16-ditetradecyl-3,16-di-azaoctadecane-1,18-dioate

1H NMR (CDCl3, 400 MHz): δ 3.70 (t, 2H, J = 7.4 Hz, 2 x –CH(H)-OtBu); 3.68 (s, 6H, 2 x -OCH3); 3.54-3.42 (m, 4H, 2 x –CH(H)OH + 2 x -CH); 2.58 and 2.50 (dt, 4H, J = 14.9, 7.4 Hz and m, 4H, N-CH2-(CH2)10-CH2-N and –N-CH2-C13H27), 1.48-1.34 (m, 8H, 2 x -CH2-CH2-N-CH2-CH2-C12H25); 1.30 (bs, 60H, -(CH2)11- + -N-(CH2)2-(CH2)8-(CH2)2-N-); 1.16 (18H, 2 x –C(CH3)3); 0.88 (t, 6H, J = 7.0 Hz, 2 x -CH3).

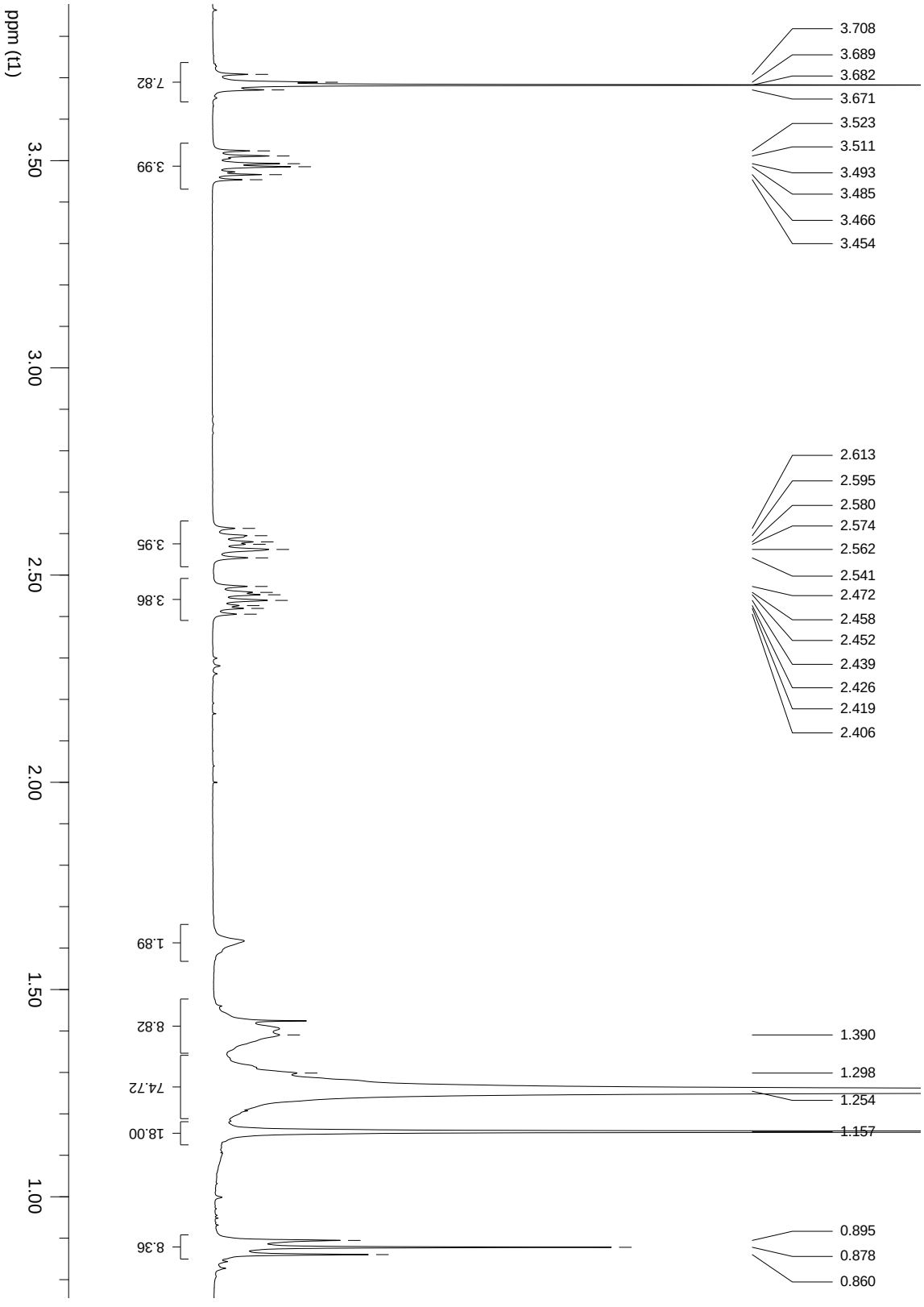

Suppl. Info. 1 - ^{1}H NMR spectra for dimethyl (2S,17S)-Bis(tert-butyloxymethyl)-3,16-ditetradecyl-3,16-di-azaoctadecane-1,18-dioate. Intermediate product.

Dodecamethylene*bis*{[(2-*tert*-butyloxy-1-methoxycarbonyl)ethyl]-(methyl) (tetradecyl) ammonium} diiodide

^{1}H NMR ($CDCl_3$, 400 MHz): δ 5.26-5.10 (m, 2 H, 2 x -C<u>H</u>); 4.24-4.02 (m, 4H, 2 x -C<u>H</u>$_2$O^{t}Bu); 3.90-3.50 (m, 8H, 2 x –C<u>H</u>$_2$-N$^+$(CH_3)-C<u>H</u>$_2$-$C_{13}H_{27}$); 3.82 and 3.81 (2 x s, 6H, 2 x –OC<u>H</u>$_3$); 3.45 (bs, 6H, -N$^+$(C<u>H</u>$_3$)-); 1.96-1.66 (m, 8H, -C<u>H</u>$_2$-CH_2-N$^+$(CH_3)-CH_2-C<u>H</u>$_2$-$C_{12}H_{25}$); 1.50-1.20 (m + bs, 60H, -(C<u>H</u>$_2$)$_{11}$- + -N$^+$-$(CH_2)_2$-(C<u>H</u>$_2$)$_8$-$(CH_2)_2$-N$^+$-); 0.85 (t, 6H, *J* = 6.8 Hz, 2 x -C<u>H</u>$_3$).

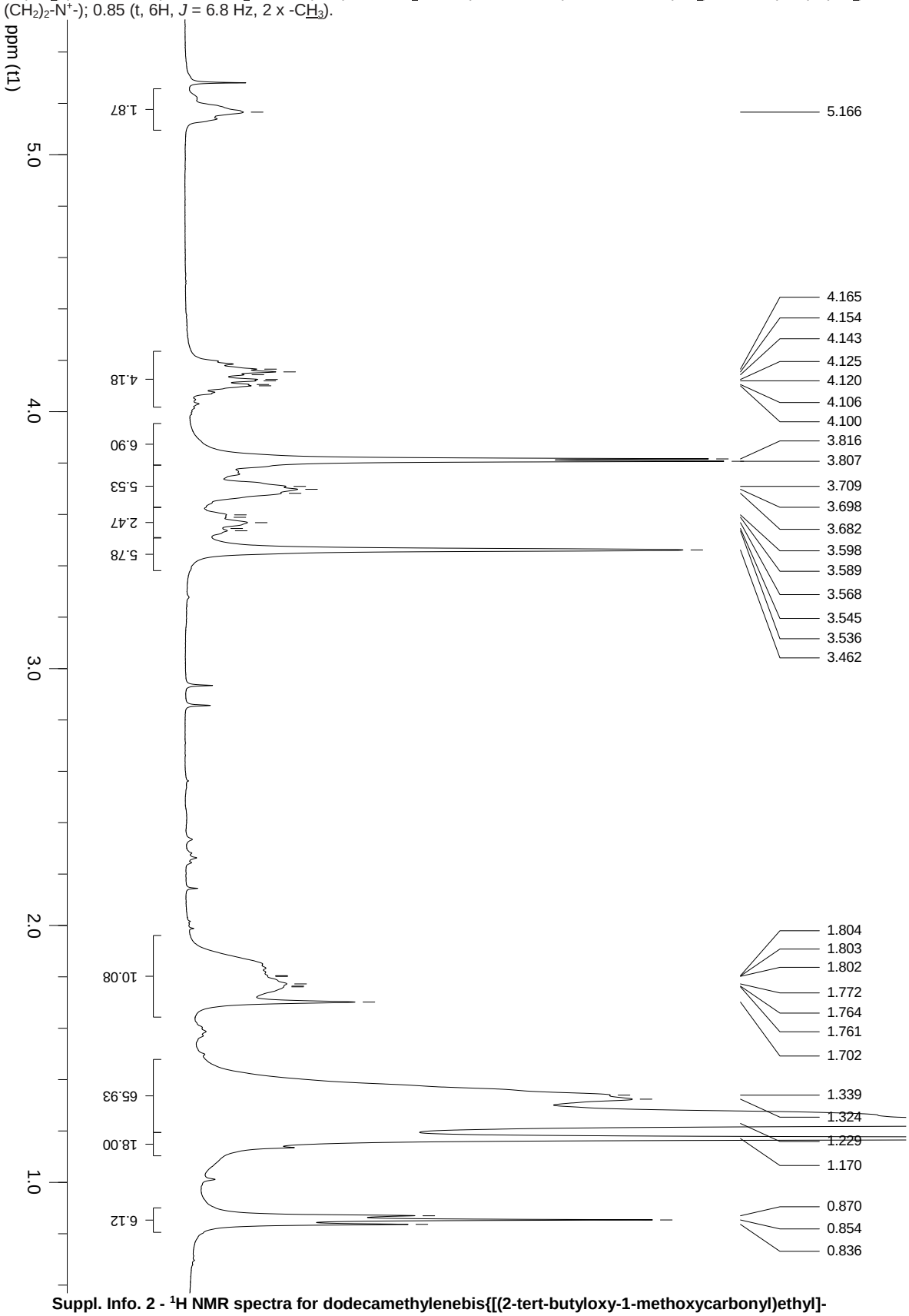

Suppl. Info. 2 - ^{1}H NMR spectra for dodecamethylenebis{[(2-tert-butyloxy-1-methoxycarbonyl)ethyl]-(methyl)(tetradecyl) ammonium} diiodide. Intermediate product.

Dodecamethylene-\ *bis*{[(2-hydroxy-1-methoxycarbonyl)ethyl](methyl)(tetradecyl)ammonium} *Bis*(trifluoroacetate)

^{1}H NMR (Acetone, 400 MHz): δ 4.78-4.72 (m, 2 H, 2 x -C<u>H</u>); 4.44-4.35 (m, 2H, -C<u>H</u>$_2$OH); 4.35-4.26 (m, 2H, -C<u>H</u>$_2$OH); 3.88 and 3.84 (2 x bs, 12H, 2 x –OC<u>H</u>$_3$); 3.83-3.64 (m, 8H, 2 x –C<u>H</u>$_2$-N$^+$(CH$_3$)-C<u>H</u>$_2$-C$_{13}$H$_{27}$) 3.49, 3.47, 3.46, 3.45 and 3.40 (5 x bs, 6H, -N+(C<u>H</u>$_3$)-); 2.00-1.73 (m, 8H, -C<u>H</u>$_2$-CH$_2$-N$^+$(CH$_3$)-CH$_2$-C<u>H</u>$_2$-C$_{12}$H$_{25}$); 1.38 and 1.28 (bs, 60H, -(C<u>H</u>$_2$)$_{11}$- + -N$^+$-(CH$_2$)$_2$-(C<u>H</u>$_2$)$_8$-(CH$_2$)$_2$-N$^+$-); 0.88 (t, 6H, *J* = 6.4 Hz, 2 x -C<u>H</u>$_3$).

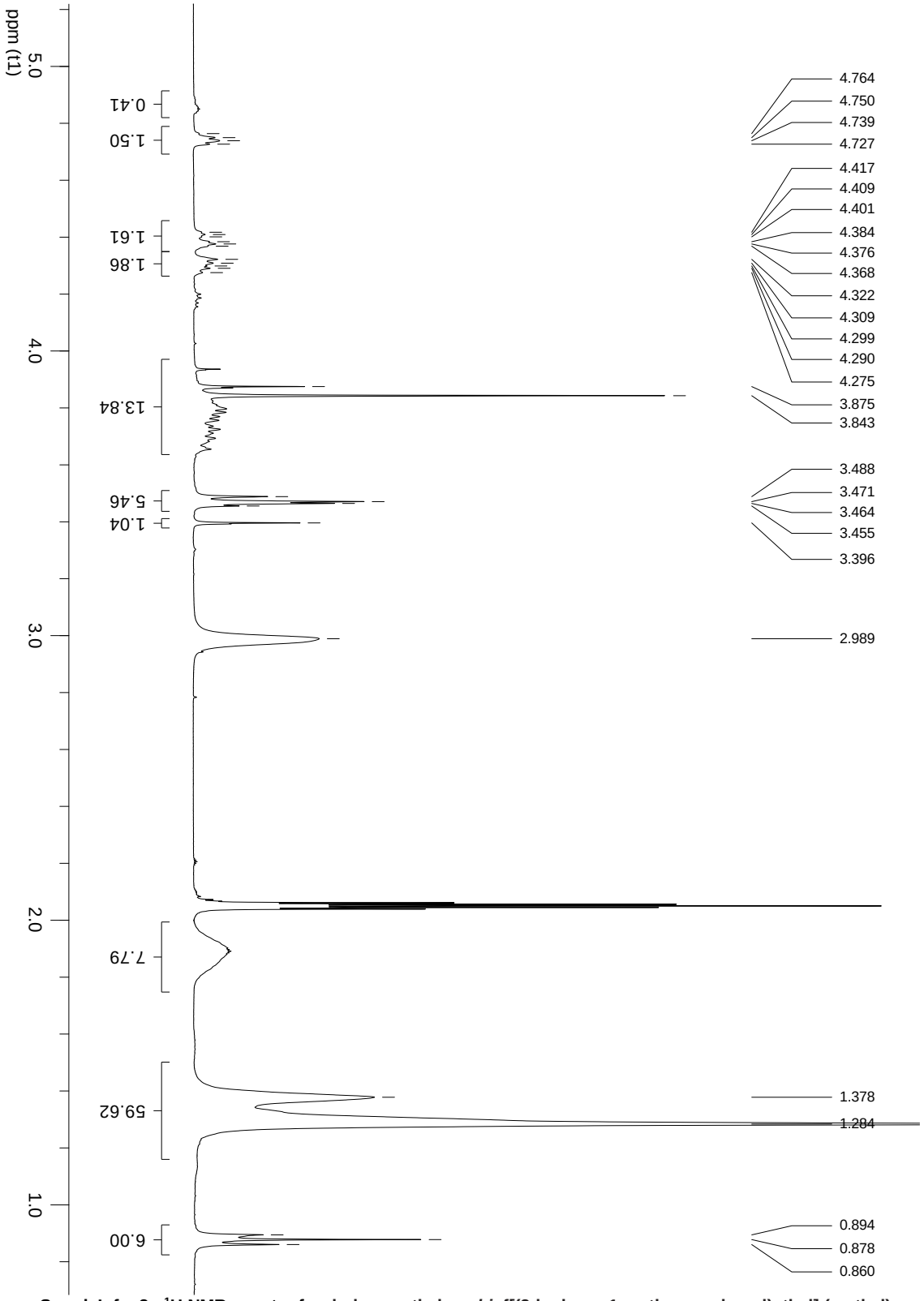

Suppl. Info. 3 - ^{1}H NMR spectra for dodecamethylene *bis*{[(2-hydroxy-1-methoxycarbonyl)ethyl] (methyl) (tetradecyl)ammonium} Bis(trifluoroacetate). Final product - (14Ser)$_2$N12.

^{13}C NMR (Acetone, 100 MHz): δ 168.7 (C=O); 74.3 and 74.2(5) (-CH); 63.9, 63.7, 63.6 (-$\underline{C}H_2$-N^+-$\underline{C}H_2$-$C_{13}H_{27}$); 60.5 and 59.7 (-CH_2OH); 54.6 (-OCH_3); 48.9 and 48.8 (-$N^+(CH_3)$), [33.6, 31.5-30.0 and 27.98 (N+(CH_3)-CH_2-($\underline{C}H_2$)$_{12}$-CH_3)], 24.3 and 23.9(-N^+-CH_2-($\underline{C}H_2$)$_8$-N^+),15.3 (-CH_3).

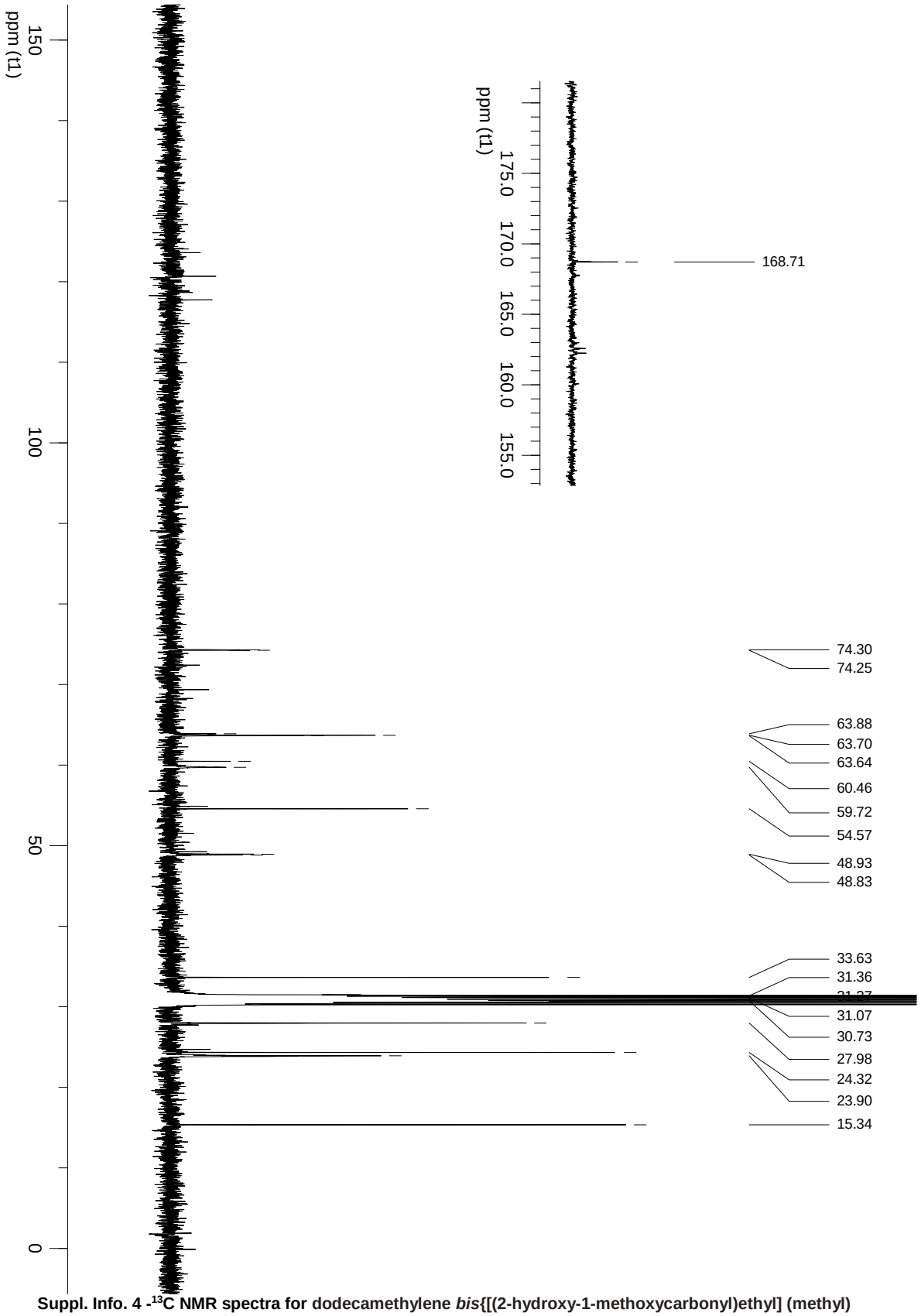

Suppl. Info. 4 -^{13}C NMR spectra for dodecamethylene *bis*{[(2-hydroxy-1-methoxycarbonyl)ethyl] (methyl) (tetradecyl)ammonium} Bis(trifluoroacetate). Final product - (14Ser)$_2$N12.

Dimethyl (2*S*,17*S*)-*Bis*(*tert*-butyloxymethyl)-3,16-dihexadecyl-3,16-di-azaoctadecane-1,18-dioate

^{1}H NMR ($CDCl_3$, 400 MHz): δ 3.71 (t, 2H, *J* = 7.6 Hz, 2 x –C<u>H</u>(H)-O^{t}Bu); 3.71 (s, 6H, 2 x -OC<u>H</u>$_3$); 3.57-3.45 (m, 4H, 2 x –CH(<u>H</u>)OH + 2 x -CH); 2.65-2.40 (2 m, 8H, N-C<u>H</u>$_2$-$(CH_2)_{10}$-C<u>H</u>$_2$-N and –N-C<u>H</u>$_2$-$C_{15}H_{31}$), 1.50-1.37 (m, 8H, 2 x -C<u>H</u>$_2$-CH_2-N-CH_2-C<u>H</u>$_2$-$C_{14}H_{29}$); 1.27 (bs, 68H, -$(C\underline{H}_2)_{13}$- + -N-$(CH_2)_2$-$(C\underline{H}_2)_8$-$(CH_2)_2$-N-); 1.18 (18H, 2 x –$C(CH_3)_3$); 0.90 (t, 6H, *J* = 6.8 Hz, 2 x -C<u>H</u>$_3$).

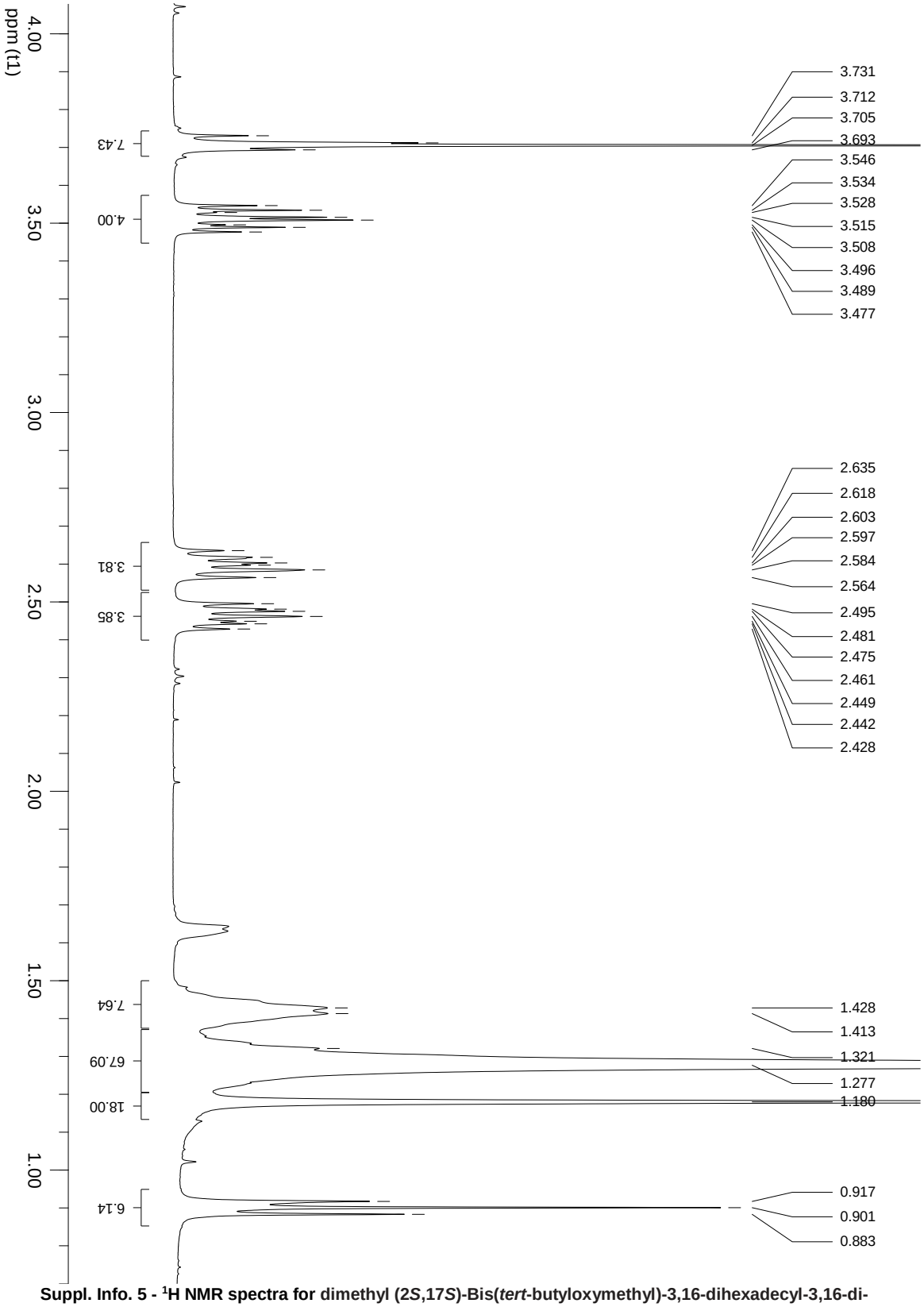

Suppl. Info. 5 - ^{1}H NMR spectra for dimethyl (2*S*,17*S*)-Bis(*tert*-butyloxymethyl)-3,16-dihexadecyl-3,16-di-azaoctadecane-1,18-dioate). Intermediate product.

Dodecamethylene*bis*{[(2-*tert*-butyloxy-1-methoxycarbonyl)ethyl]-(hexadecyl) (methyl) ammonium} diiodide

^{1}H NMR ($CDCl_3$, 400 MHz): δ 5.20-5.00 (m, 2 H, 2 x -C<u>H</u>); 4.68-4.54 (m, 2H, -C<u>H</u>$_2$O^{t}Bu); 4.43-4.29 (m, 2H, -C<u>H</u>$_2$O^{t}Bu); 3.90 and 3.84 (2 x s, 6H, 2 x –OC<u>H</u>$_3$); 3.74-3.40 (m, 8H, 2 x –C<u>H</u>$_2$-N$^+$(CH$_3$)-C<u>H</u>$_2$-C$_{15}$H$_{31}$); 3.36, 3.35, 3.32, 3.29 (4 x s, 6H, -N$^+$(C<u>H</u>$_3$)-); 1.80-1.50 (m, 8H, -C<u>H</u>$_2$-CH$_2$-N$^+$(CH$_3$)-CH$_2$-C<u>H</u>$_2$-C$_{14}$H$_{27}$); 1.27 (bs, 68H, -(C<u>H</u>$_2$)$_{13}$- + -N$^+$-(CH$_2$)$_2$-(C<u>H</u>$_2$)$_8$-(CH$_2$)$_2$-N$^+$-); 0.90 (t, 6H, *J* = 7.0 Hz, 2 x -C<u>H</u>$_3$).

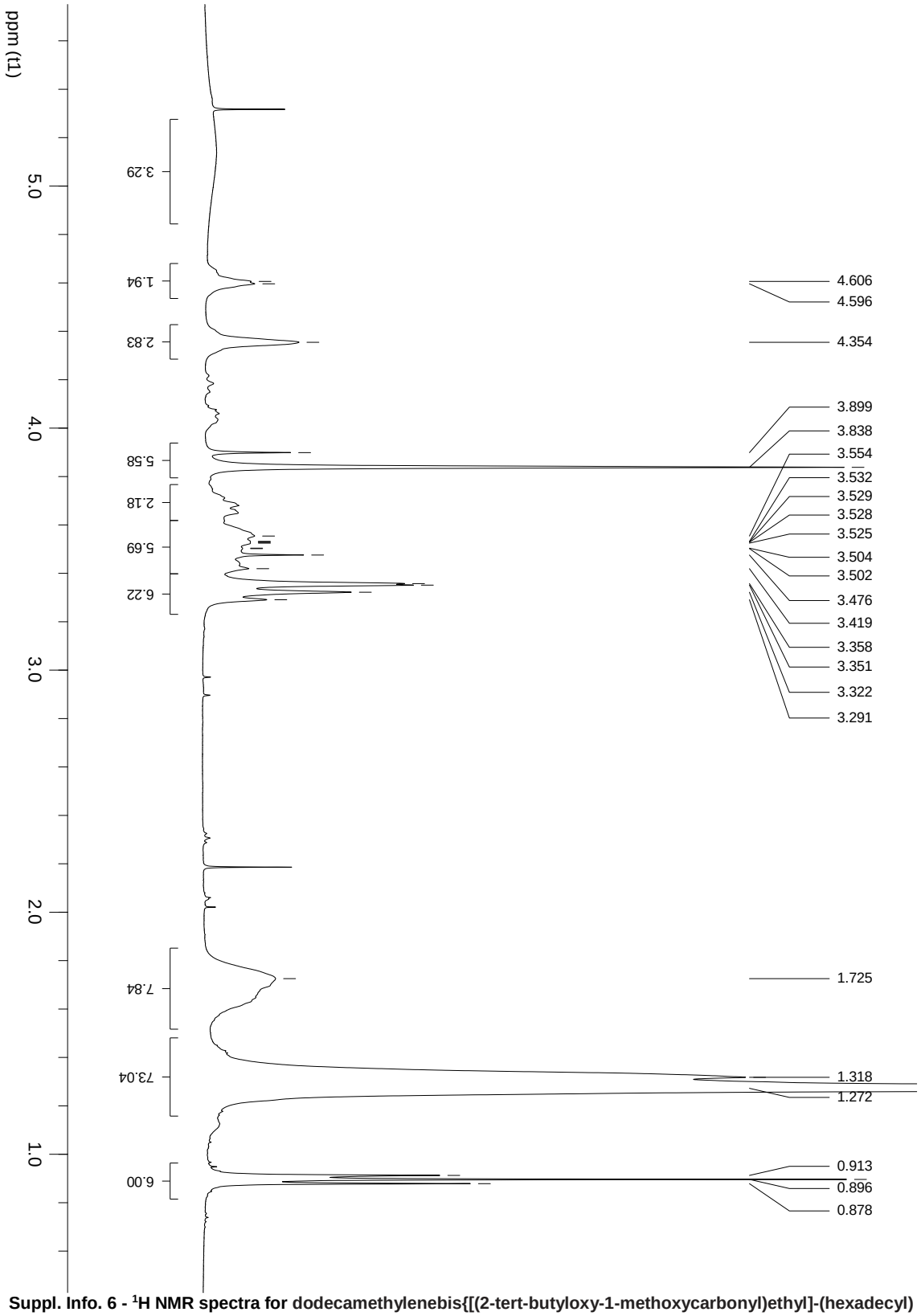

Suppl. Info. 6 - ^{1}H NMR spectra for dodecamethylenebis{[(2-tert-butyloxy-1-methoxycarbonyl)ethyl]-(hexadecyl) (methyl) ammonium} diiodide. Intermediate product.

Dodecamethylene *bis*{[(2-hydroxy-1-methoxycarbonyl)ethyl] (hexadecyl)(methyl)ammonium} *Bis*(trifluoroacetate)

^{1}H NMR ($CDCl_3$, 400 MHz):δ = 4.74 (bs, 2H, 2 x -C<u>H</u>); 4.45-4.26 (m, 4H, 2 x -C<u>H$_2$</u>OH); 4.14-3.44 (bs ,+ m, 14H –OC<u>H$_3$</u> + -C<u>H$_2$</u>-N$^+$(CH_3)-C<u>H$_2$</u>-$C_{15}H_{31}$), 3.41 and 3.37 (2 x bs 6H, -N+(C<u>H$_3$</u>)-); 1.90-1.56 (m, 8H, -C<u>H$_2$</u>-CH_2-N$^+$(CH_3)-CH_2-C<u>H$_2$</u>-$C_{14}H_{29}$); 1.38 and 1.27 (2 x bs, 68H, 2 x -(C<u>H$_2$</u>)$_{11}$- + -N$^+$-$(CH_2)_2$-(C<u>H$_2$</u>)$_8$-$(CH_2)_2$-N$^+$-); 0.88 (t, 6H, *J* = 6.4 Hz, 2 x -C<u>H$_3$</u>).

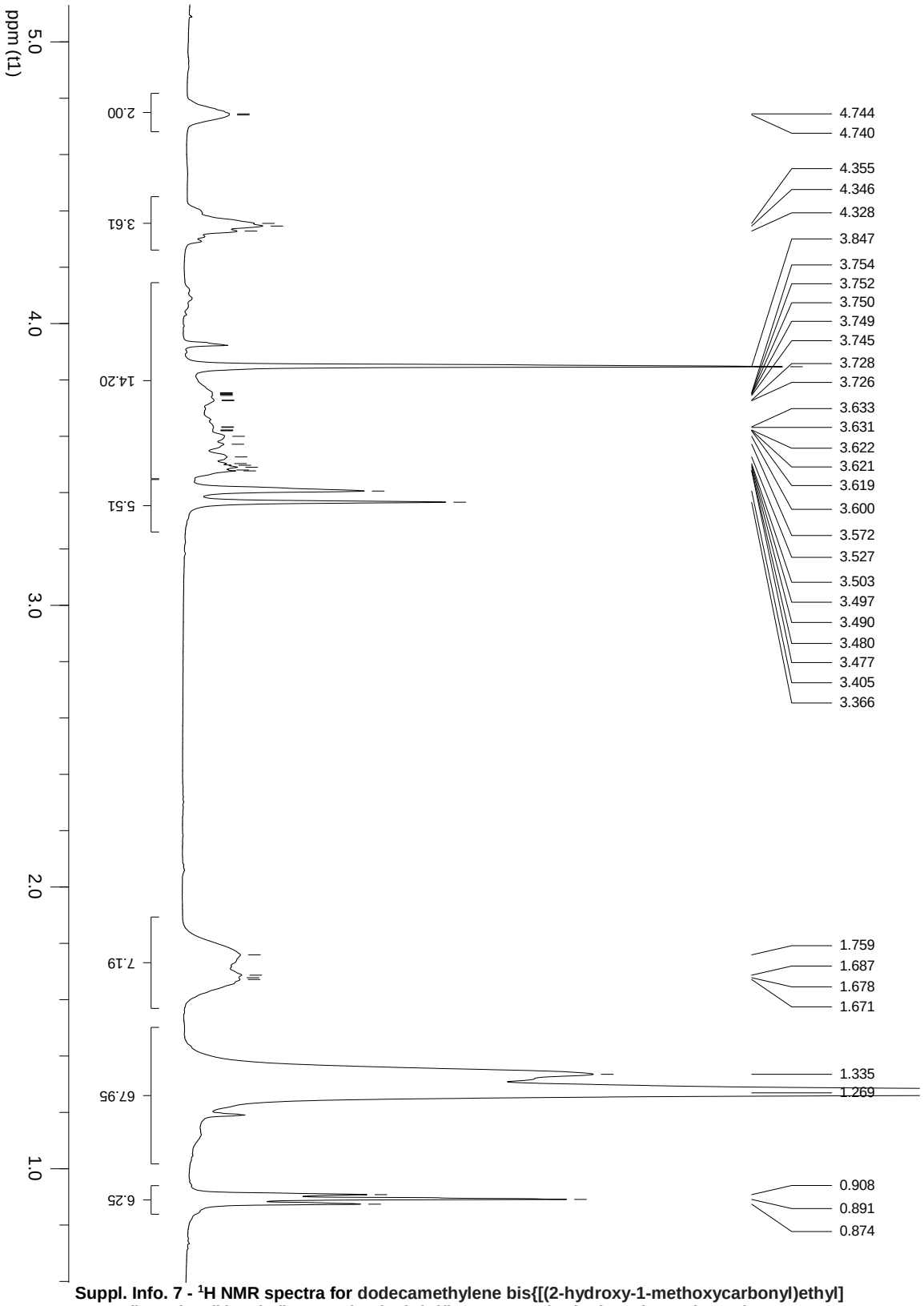

Suppl. Info. 7 - ^{1}H NMR spectra for dodecamethylene bis{[(2-hydroxy-1-methoxycarbonyl)ethyl] (hexadecyl)(methyl)ammonium} Bis(trifluoroacetate). Final product – $(16Ser)_2N12$.

Dimethyl (2*S*,17*S*)-Bis(*tert*-butyloxymethyl)-3,16-dioctadecyl-3,16-di-azaoctadecane-1,18-dioate

^{1}H NMR ($CDCl_3$, 400 MHz): δ 3.73 (t, 2H, *J* = 7.6 Hz, 2 x –C<u>H</u>(H)-O^{t}Bu); 3.71 (s, 6H, 2 x -OC<u>H</u>$_3$); 3.58-3.46 (m, 4H, 2 x –CH(<u>H</u>)OH + 2 x -CH); 2.66-2.54 and 2.52-2.40 (2 m, 8H, N-C<u>H</u>$_2$-$(CH_2)_{10}$-C<u>H</u>$_2$-N and –N-C<u>H</u>$_2$-$C_{15}H_{31}$), 1.50-1.37 (m, 8H, 2 x -C<u>H</u>$_2$-CH_2-N-CH_2-C<u>H</u>$_2$-$C_{16}H_{33}$); 1.18 (bs, 76H, -(C<u>H</u>$_2$)$_{15}$- + -N-$(CH_2)_2$-(C<u>H</u>$_2$)$_8$-$(CH_2)_2$-N-); 1.18 (18H, 2 x –C$(CH_3)_3$); 0.90 (t, 6H, *J* = 6.8 Hz, 2 x -C<u>H</u>$_3$).

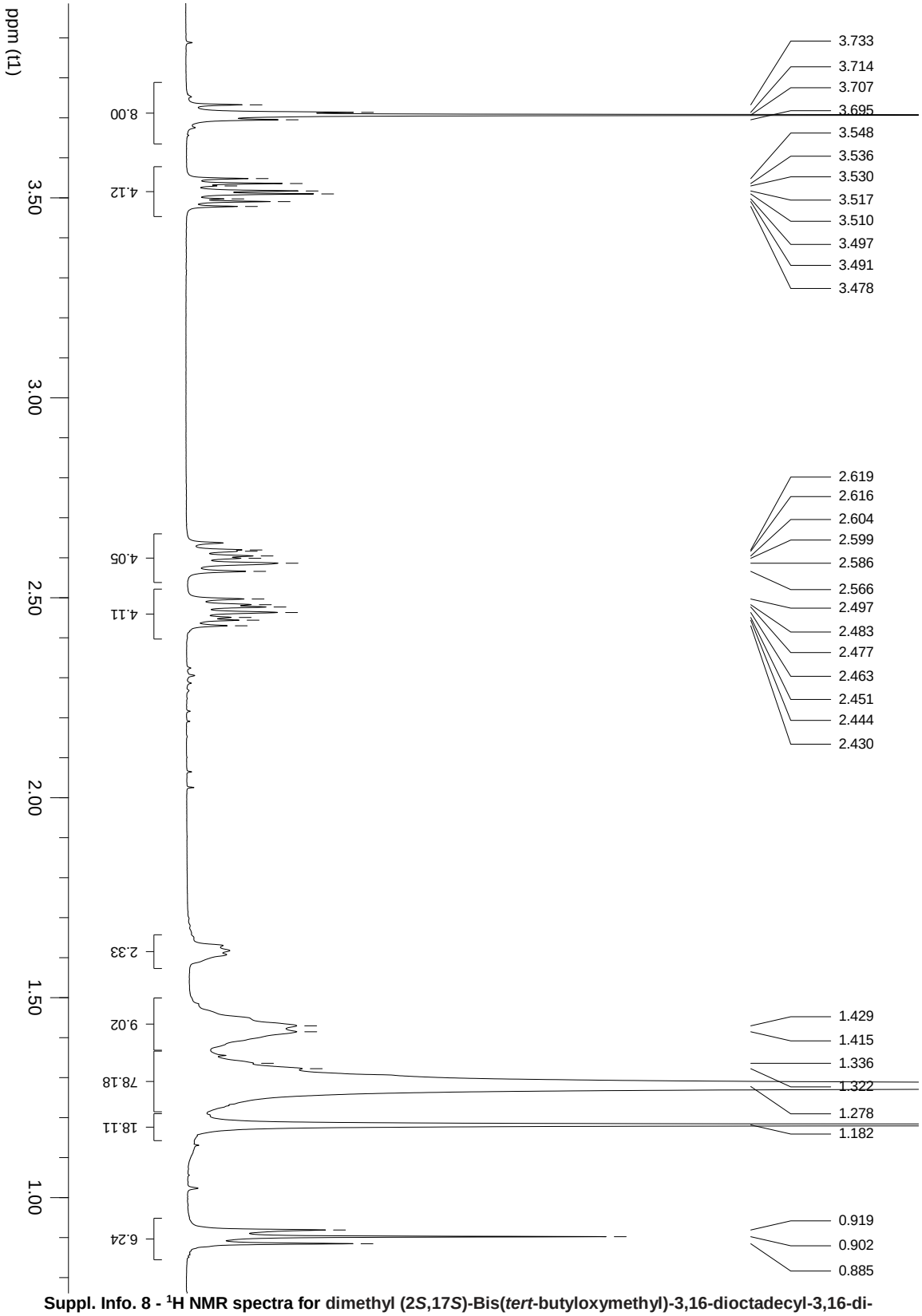

Suppl. Info. 8 - ^{1}H NMR spectra for dimethyl (2*S*,17*S*)-Bis(*tert*-butyloxymethyl)-3,16-dioctadecyl-3,16-di-azaoctadecane-1,18-dioate. Intermediate product.

Dodecamethylene*bis*{[(2-*tert*-butyloxy-1-methoxycarbonyl)ethyl]-(methyl) (octadecyl) ammonium} diiodide

^{1}H NMR ($CDCl_3$, 400 MHz): δ 5.26-5.15 (m, 2 H, 2 x -C<u>H</u>); 4.28-4.05 (m, 4H, 2 x -C<u>H</u>$_2$O^{t}Bu); 3.90-3.50 (m, 8H, 2 x –C<u>H</u>$_2$-N$^+$(CH$_3$)-C<u>H</u>$_2$-C$_{17}$H$_{35}$); 3.84 and 3.83 (2 x s, 6H, 2 x -OC<u>H</u>$_3$); 3.48, 3.47, 3.43, 3.44 (4 x s, 6H, -N$^+$(C<u>H</u>$_3$)-); 1.95-1.65 (m, 8H, -C<u>H</u>$_2$-CH$_2$-N$^+$(CH$_3$)-CH$_2$-C<u>H</u>$_2$-C$_{16}$H$_{33}$); 1.50-1.30 (m + bs, 76H, -(C<u>H</u>$_2$)$_{15}$- +-N$^+$-(CH$_2$)$_2$-(C<u>H</u>$_2$)$_8$-(CH$_2$)$_2$-N$^+$-); 0.88 (t, 6H, *J* = 6.8 Hz, 2 x -C<u>H</u>$_3$).

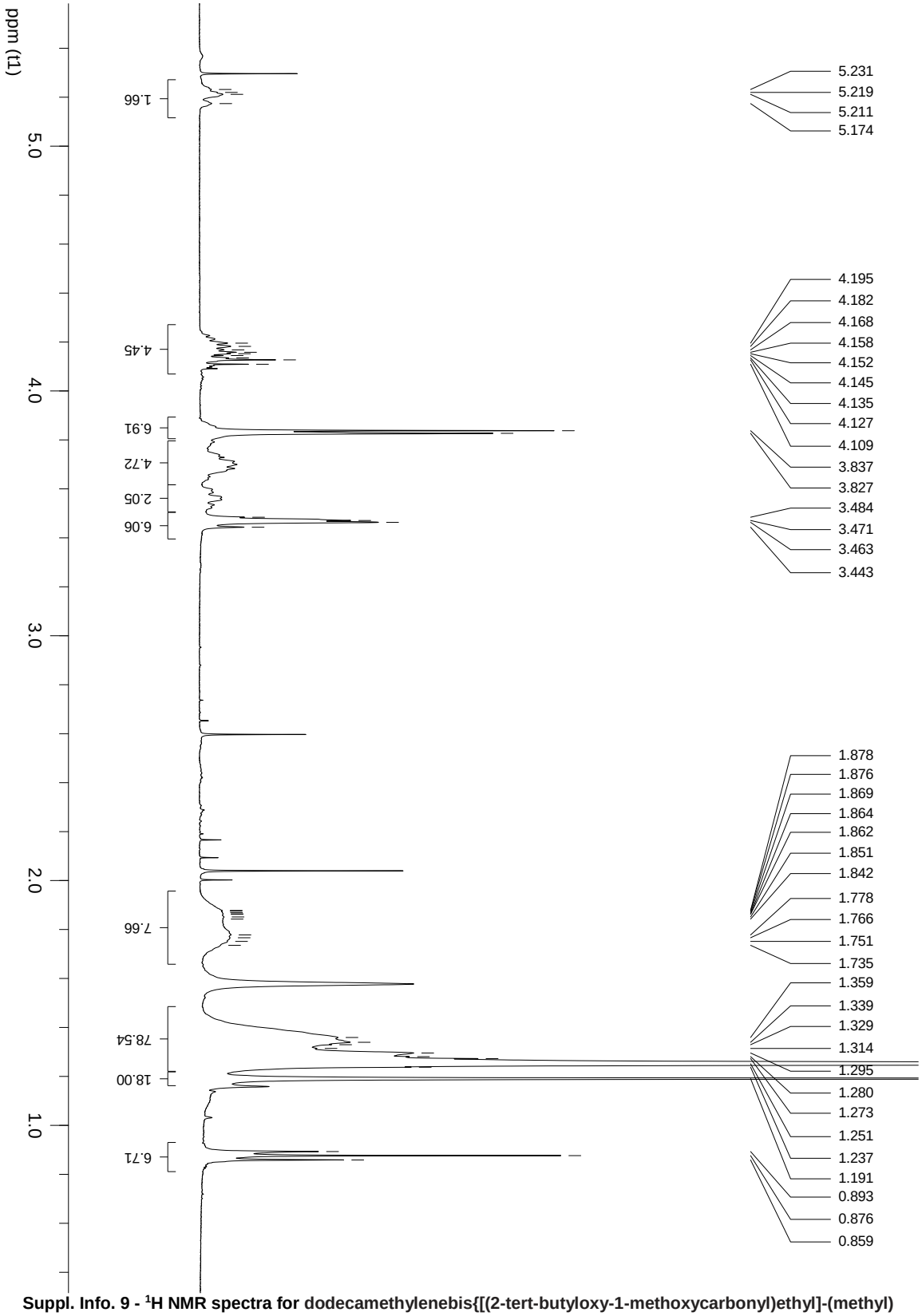

Suppl. Info. 9 - ^{1}H NMR spectra for dodecamethylenebis{[(2-tert-butyloxy-1-methoxycarbonyl)ethyl]-(methyl) (octadecyl) ammonium} diiodide. Intermediate product.

Dodecamethylene *bis*{[(2-hydroxy-1-methoxycarbonyl)ethyl] (methyl) (octadecyl)ammonium} *Bis*(trifluoroacetate)

^{1}H NMR (Acetone, 400 MHz):δ = 4.28, 4.72 (2 x bs, 2H, 2 x -C<u>H</u>); 4.46-4.14 (m, 4H, 2 x -C<u>H$_2$</u>OH); 3.96-3.60 (2 x bs + bs, 14H, 2 x –OC<u>H$_3$</u> + 2 x –C<u>H$_2$</u>-N$^+$(CH$_3$)-C<u>H$_2$</u>-C$_{17}$H$_{34}$) 3.50, 3.49, 3.41(4) and 3.41 (4 x s, 6H, -N+(C<u>H$_3$</u>)-); 2.10-1.80 (m, 8H, -C<u>H$_2$</u>-CH$_2$-N$^+$(CH$_3$)-CH$_2$-C<u>H$_2$</u>-C$_{16}$H$_{32}$); 1.39 and 1.32 (bs, 76H, -(C<u>H$_2$</u>)$_{15}$- + -N$^+$-(CH$_2$)$_2$-(C<u>H$_2$</u>)$_8$-(CH$_2$)$_2$-N$^+$-); 0.89 (t, 6H, *J* = 6.8 Hz, 2 x -C<u>H$_3$</u>).

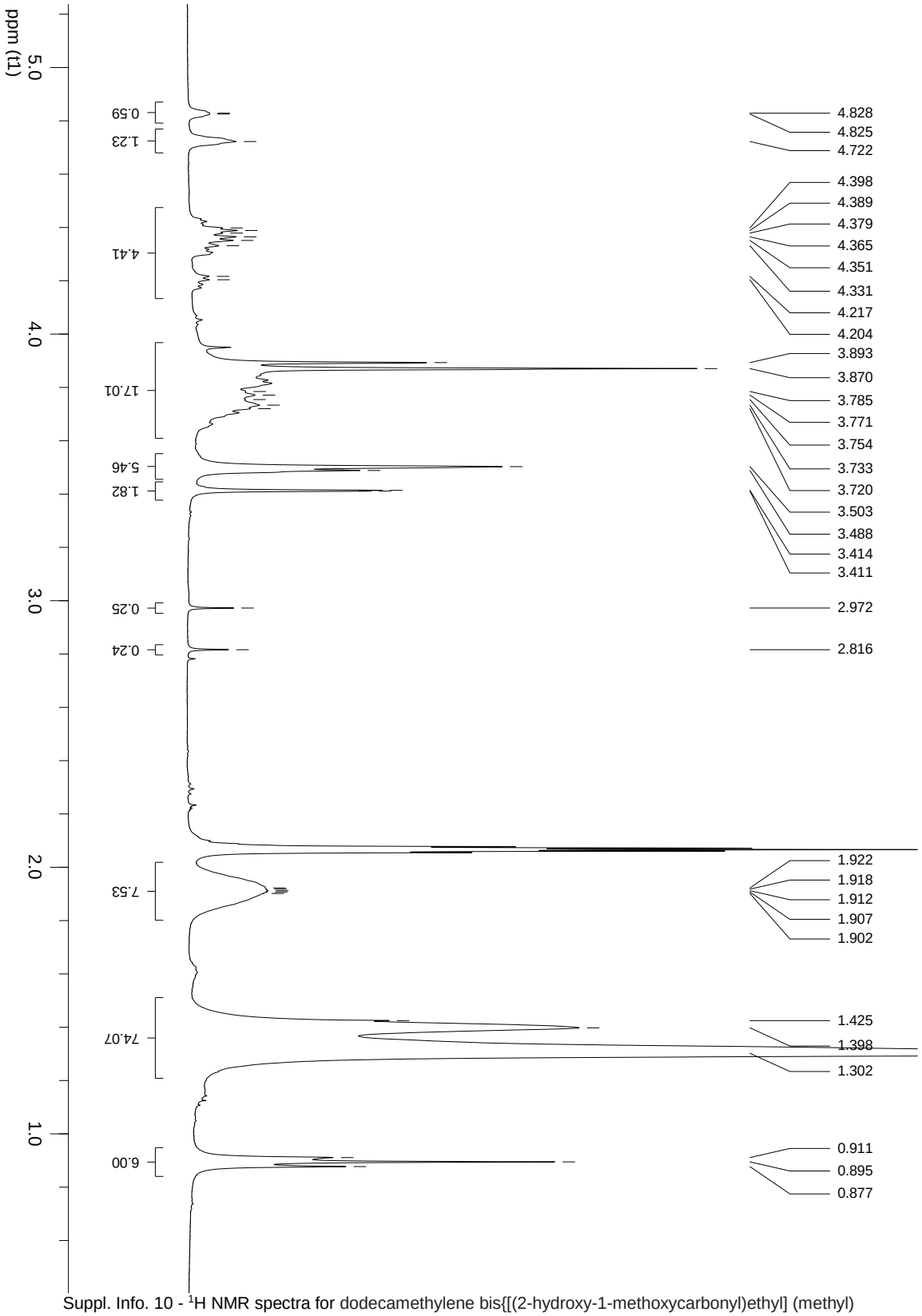

Suppl. Info. 10 - ^{1}H NMR spectra for dodecamethylene bis{[(2-hydroxy-1-methoxycarbonyl)ethyl] (methyl) (octadecyl)ammonium} Bis(trifluoroacetate). Final product – (18Ser)$_2$N12.

^{13}C NMR (Acetone, 100 MHz): δ 168.5 and 167.6 (C=O); 74.2, 74.1 and 72.4 (-CH); 63.9, 63.8, 63.7(6) (-$\underline{C}H_2$-N^+-$\underline{C}H_2$-$C_{17}H_{35}$); 59.8 and 59.7(8) (-CH_2OH); 54.9 and 54.7 (-OCH_3); 49.3 49.1 and 48.9 (-$N^+(CH_3)$), [33.6, 31.8-30.1 and 27.9 (N+(CH_3)-CH_2-($\underline{C}$H2)$_{16}$-CH_3)], 24.3 and 23.9 (-N^+-CH_2-($\underline{C}H_2$)$_8$-N^+), 15.3 (-CH_3).

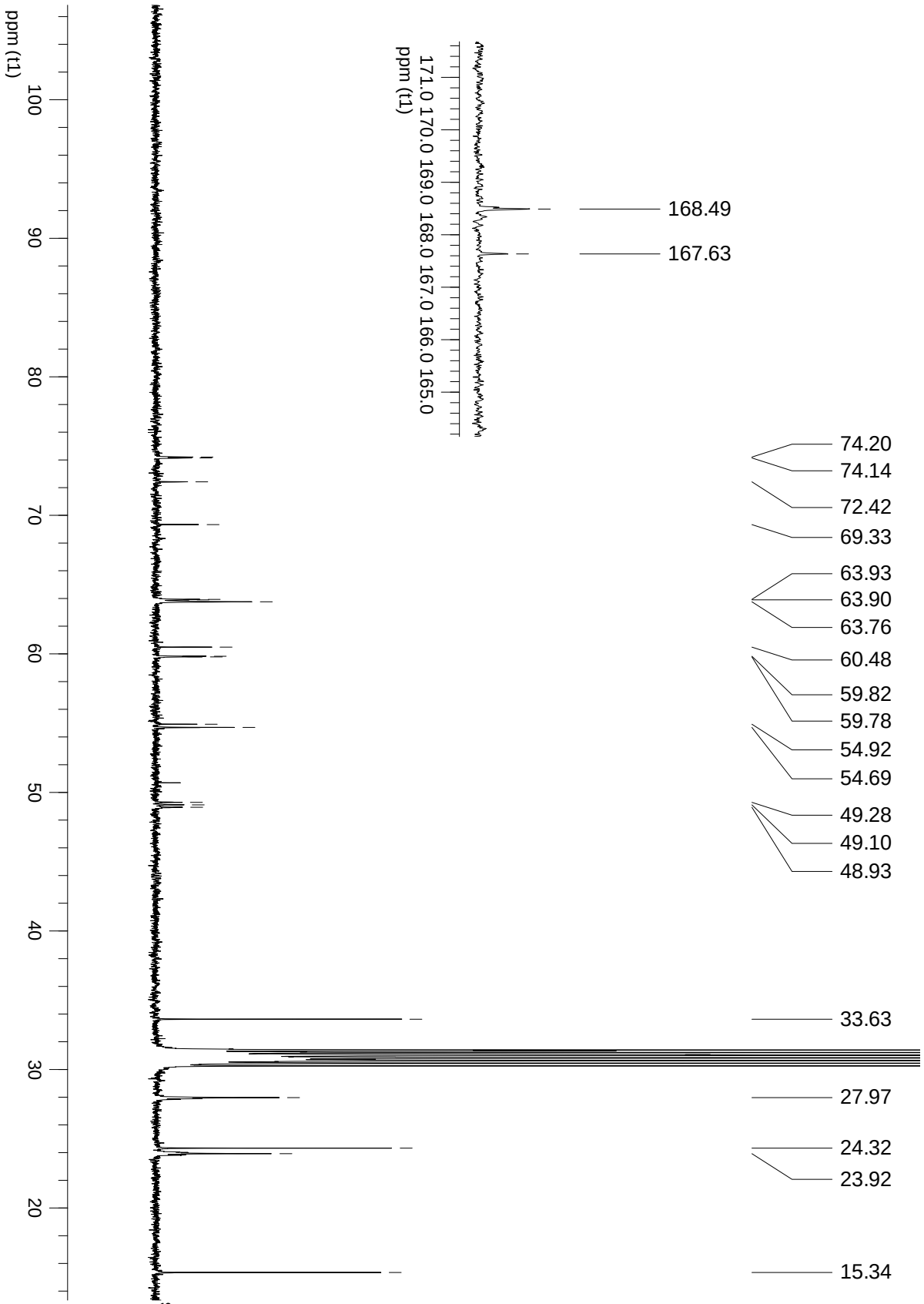

Suppl. Info. 11 – ^{13}C NMR spectra for dodecamethylene bis{[(2-hydroxy-1-methoxycarbonyl)ethyl] (methyl) (octadecyl)ammonium} Bis(trifluoroacetate). Final product – $(18Ser)_2N12$.